LOWER HYBRID HEATING
ASSOCIATED WITH MODE CONVERSION
ON THE WISCONSIN OCTUPOLE

by

THOMAS LLEWELLYN OWENS

A thesis submitted in partial fulfillment of the
requirements for the degree of

DOCTOR OF PHILOSOSPHY
(Electrical Engineering)

at the
UNIVERSITY OF WISCONSIN - MADISON
1979

LOWER HYBRID HEATING ASSOCIATED WITH MODE CONVERSION ON THE WISCONSIN OCTUPOLE

Thomas Llewellyn Owens

Under the supervision of Professor J.E. Scharer

This thesis addresses the following key issues in the lower hybrid frequency range: 1. What are the important physics aspects of wave propagation and heating in an experimental situation? 2. How effective is plasma heating in the complex magnetic field configuration of the octupole?

Experimental work is accomplished by launching 1-10ms pulses of up to 40kW of radio frequency power at 140MHz corresponding to the hot plasma lower hybrid resonance in the octupole. A dipole antenna which is moveable radially and is also rotatable couples wave power to the plasma. Coupling efficiencies greater than 95% are achieved by proper antenna placement near the edge of the plasma radial density profile.

Substantial ion body temperature increases of $\Delta T_i = 37\text{eV}$ ($\Delta T_i/T_{io} = 12$) in a helium plasma are measured from Doppler broadening of the helium 4686 Å line using a Fabry-Perot interferometer. From spatial scans of ion temperature using a miniature transverse ion energy analyzer in a hydrogen plasma, heating efficiencies in the range of 15-40% are found. The higher efficiencies in this range occur for denser plasmas.

The spatial scans of ion temperature also show that the heating zone follows a constant density surface defined by $\omega/\omega_{pi} \simeq 1.2$ as the

peak density is varied from $n = 3 \times 10^{11} cm^{-3}$ to $n = 8 \times 10^{11} cm^{-3}$ with $\omega/(\omega_{ci}\omega_{ce})^{\frac{1}{2}} \simeq 0.7$. As the peak density is raised above $n = 3 \times 10^{11} cm^{-3}$, edge heating results and the plasma is driven unstable as indicated by rapid plasma loss measured on a 35GHz microwave interferometer.

For $n = 3 \times 10^{11} cm^{-3}$ the heating zone is on the separatrix. The density is held constant during wave heating for periods of 10 ms indicative of a stable interaction at this density. Temperature decay times are 1-2ms at this density, also corresponding to a stable plasma situation.

Ion heating is eliminated and only electron heating remains at densities below $n = 3 \times 10^{11} cm^{-3}$. In addition, as the magnetic field is lowered, higher densities, above $n = 3 \times 10^{11} cm^{-3}$, are required to produce ion heating. No ion heating at any density occurs for $\omega/(\omega_{ci}\omega_{ce})^{\frac{1}{2}} \gtrsim 1.5$ where the magnetic field values are evaluated near the location of the lower hybrid resonance.

These observations are in close agreement with the theory of mode conversion from a cold to hot plasma lower hybrid mode if we impose the condition that $k_z v_e/\omega \simeq 0.3$. This represents a substantial upshift of the k_z wave power spectrum from that which is theoretically predicted to be formed at the antenna. Detailed wavelength measurements of k_x (from which k_z can be inferred) confirm this and indicate that the upshift in k_z occurs near the lower hybrid wave turning point. Substantial electron heating (ΔT_e=7eV) is also observed using Langmuir probes, consistent with electron Landau damping at these high values of k_z. It is proposed that the mechanism for transforming k_z from the edge to enhanced values near the turning point is associated with plasma inhomogeneities.

Wave probe measurements indicate that a high Q eigenmode associated with the fast lower hybrid branch exists in the octupole but does not couple substantial power due to the weak absorption.

The substantial ion heating with plasma stability obtained in the octupole, together with the excellent correlation of results with the linear theory of mode conversion provide optimism that lower hybrid waves can provide effective heating in an octupole.

ACKNOWLEGEMENTS

I gratefully acknowledge the helpful suggestions of Professor J.E. Scharer. I am thankful for his encouragement and enthusiastic interest in this research.

Paul Nonn's help was invaluable in constructing the lower hybrid oscillators, antenna, and associated RF equipment.

I thank David Brouchous for helpful discussions and for fabricating the first reliable perpendicular ion energy analyzer on the octupole, which was a key diagnostic in this research.

I am indebted to John Laufenberg and members of the octupole group for technical assistance and for their hard work in repairing and maintaining equipment used in the experiment.

I recognize that the personal God of the universe has tailored all of the science that we explore in this world. During the course of this work He has been a source of strength and help.

Finally, I greatly appreciate the excellent job of typing of this manuscript by my wife Lois. I cannot adequately express how much her patience and uplifting spirit have meant to me.

This research was supported by the United States Department of Energy.

TABLE OF CONTENTS

	Page
ABSTRACT	ii
ACKNOWLEDGEMENTS	v
TABLE OF CONTENTS	vi
1. INTRODUCTION	1
2. THEORY OF LOWER HYBRID WAVE PROPAGATION AND ABSORPTION	8
A. The Collisionless Model	8
A.1. Hot Plasma Effects	18
A.2. Unmagnetized Ion Approximation	24
A.3. First Order Approximation	29
B. Wave Fields	36
B.1. Cold Plasma Model	36
B.2. Three Dimensional Effects	43
B.3. Hot Plasma Model	45
C. Collisional Effects	48
3. EXPERIMENTAL APPARATUS	52
A. The Toroidal Octupole	52
B. Radio Frequency Sources	55
C. Wave Coupling	58
4. DIAGNOSTICS	66
A. Microwave Fringe-Shift Interferometer	66
B. Optical Fabry-Perot Interferometer	69
B.1 General Considerations	69
B.2 Experimental Procedures	74
C. Gridded Energy Analyzers	86
5. ION HEATING ASSOCIATED WITH MODE CONVERSION PROCESSES	97
A. Bulk Ion Heating	97
B. Ion Temperature Profiles	103
B.1 Ion Saturation Current Profiles	104
B.2. Energy Analyzer Measurements	106

C. Variation with Density and Magnetic Field 118
D. Power Dependence 123
E. Heating Efficiency 126

6. ELECTRON HEATING 129

7. EFFECTS OF HEATING ON PARTICLE CONTAINMENT 135

8. LOWER HYBRID WAVE FIELDS 140
A. Spacial Profiles 140
B. Parametric Instabilities 145
C. Slow Mode Wavelengths 147

9. CONCLUSIONS 157

APPENDIX A PRINCIPLES OF FABRY-PEROT INTERFEROMETRY 162

APPENDIX B COMPARISON OF FABRY-PEROT THROUGHPUT WITH PRISM AND GRATING MONOCHROMATORS 169

REFERENCES 175

CHAPTER 1

INTRODUCTION

The ultimate success of any radio frequency plasma heating scheme under fusion reactor conditions will depend not only upon maintaining a device with adequate plasma confinement and stability but also upon success in at least the following three areas. First of all, a substantial part of the wave power must penetrate to the plasma core and be efficiently absorbed by particles having well confined orbits. Deleterious effects along the wave path such as evanescent regions, surface wave coupling, and parasitic parametric modes should be minimized or eliminated altogether, if possible. Secondly, plasma stability must be maintained during and after wave heating. Naturally, favorable confinement and transport properties of a given device will greatly facilitate any heating technique. For RF (radio frequency) heating, this is a particularly crucial prerequisite since, frequently, high energy tails are produced on the distribution of particle energies. Bulk heating and velocity isotropization are then dependent upon confining these tails for times longer than slowing down and pitch angle scattering times. Finally, any RF heating scheme must be feasible from an engineering standpoint. Efficient high power RF sources must be available at the required frequencies. Launching structures must couple power effectively and at the same time be compatible with fusion plasma conditions. Problems such as high voltage, high frequency breakdown must be overcome.

This thesis will examine in detail RF heating in the lower hybrid frequency range, $\omega_{LH}^2 \approx \omega_{pi}^2/(1 + \omega_{pe}^2/\omega_{ce}^2)$. Stix first proposed that at least the first objective outlined above, namely core heating, could be achieved by a lower hybrid wave launched from the edge of a plasma.[1] His early hypothesis was based upon a relatively simple approach using linear theory and an idealized geometry.

Subsequent theories, built upon Stix's work, examined for the case of lower hybrid waves such things as non-linear and three dimensional effects[2-5], propagation in complex geometries[6], and scattering from density flucuations.[7,8]

A variety of absorption mechanisms were proposed, including ion cyclotron[1] harmonic absorption, and stochastic heating.[5] Absorption through parametric decay modes[4,9] or through turbulent processes[10] was also thought to play a role. Wave fields in the propagating region were predicted to be localized along conical trajectories referred to as "resonance cones".[11] But later theories showed that turbulence at the plasma edge could disperse the resonance cones.[7] At large amplitudes, self-focusing would occur also breaking up the resonance cone structure and leading to parametric instabilities near the plasma edge.[2] Ponderomotive force effects were thought to occur near the launching structures which added further complications to the coupling/propagation picture.

To date, there is no clear concensus on any single theory to explain results for high-power large scale experiments due to the complexity of the lower hybrid problem. The need for information on lower hybrid heating is, then, clearly acute if we are to have confidence in proceeding.

One-half megawatt continuous wave sources in the frequency range needed for fusion reactor conditions (1-5 GHz) can be constructed with present technology. It is envisioned that a waveguide "grill"[12] will couple power from many separate sources to the plasma. Total radio frequency power levels of about 80 megawatts are needed to achieve ignition for a conceptual tokamak reactor.[13]

Lower hybrid heating experiments, to date, have shown efficient wave coupling to ions (>40%)[14] even though there is disagreement on the wave mechanisms involved. Results from the Wega tokamak show that ion temperature increases are greatest when the lower hybrid resonance is at the center of their device indicative of a mode conversion process.[14] Similarly, the JFT-2 experiment shows maximum ion heating when the lower hybrid resonance is present at the plasma core.[15] In addition, they demonstrate, for their conditions, that there is no correlation between core ion heating and parametric instabilities, eliminating this as a possibility. Their observed parametric spectra originates at the edge, quickly saturates, and absorbs a negligible portion of the pump power. On the other hand, experiments on ATC do show a correlation between ion heating and the appearance of parametric decay spectra.[16] The disagreement with JFT-2 and Wega results has not been resolved.

Recent experiments on Alcator A indicate the entire pump lower hybrid wave may undergo a slight parametric downshift in frequency

(3 MHz downshift from 2.45 GHz pump frequency) at the plasma edge.[17] This downconverted wave is then mode-converted in the plasma center and collisionlessly absorbed. Finally, the Petula tokamak has observed parametric decay spectra with sideband amplitudes as large as the pump wave.[18] Non-linear mechanisms appear to be associated with heating in this case.

The type of lower hybrid experiments presented in this thesis are the first to be performed on a toroidal octupole. Work on the General Atomic octupole has concentrated on eletron heating at frequencies well above the maximum lower hybrid frequency.[19] This also is generally referred to as lower hybrid heating because the wave follows the lower hybrid dispersion relation between the launching structure and the absorption layer. However, because $\omega > \omega_{LH}$ and because they are launching waves having large values of $k_{\parallel} = \vec{k} \cdot \vec{B} / |\vec{B}|$, the wave is absorbed through electron Laundau damping. No ion heating directly by the wave is expected in their experiment.

The present experiment, on the other hand, is designed with $\omega \simeq \omega_{LH}$ and $k_{\parallel} v_e / \omega << 1$, where $v_e^2 = kT_e/m_e$, to avoid electron Laundau damping and allow direct ion heating by the lower hybrid wave.

The chief advantage of heating by this technique is that resonance should occur on a constant density surface defined by $\omega \simeq \omega_{pi}$. This surface can be chosen to lie along the density peak near the separatrix, which is an ideal location in which to deposit wave energy and heat the plasma. Plasma near the separatrix is well confined and remains stable to increases in particle energy below the β limit. In addition, particles in this region are heated well away from walls and hoops so that neutral reflux can be minimized. This simple picture is, of course, modified by such things as hot plasma effects on wave dispersion, plasma collisionality, inhomogeneities and non-ideal antenna effects, as described in the body of this thesis.

A unique feature of the octupole relative to most other devices in which lower hybrid heating has been attempted is its complicated magnetic field geometry and plasma configuration. It would be useful to know that this complication coupled with the large plasma density and magnetic field variations found in the octupole does not severely limit the efficiency of lower hybrid heating. Conditions in the FM-1 Spherator lower hybrid heating experiment at $\omega \simeq \omega_{pi}$ come closest to the complexity of the octupole.[20] However, there are significant differences in other aspects of the experiment such as wave launching conditions and power levels.

Further motivation for this experiment stems from the recent interest in advanced fuel multipole concepts.[21] This experiment and later ones will contribute to a preliminary data base for this concept, as it develops.

Physics issues that will be addressed in this work, which may be compared to other devices include: 1. Does the wave penetrate and heat the plasma core? 2. What are the heating mechanisms involved? 3. Is plasma stability maintained during wave heating?

Core heating, question one, has been demonstrated on other experiments during the course of this work.[14-16] Wega for example, inferred core heating partly through measurements of the Doppler broadening of various impuity lines, and calculations of the spatial location of brightest emission for each impurity.[14] In addition, charge exchange measurements showed a decay time of T_i after RF heating on the order of the energy confinement time, indicative of core heating.

In this experiment, we are able to use more direct means to measure core heating. This is because the relatively cold ($T_{i,e} < 30$ eV) tenuous plasma ($n < 2 \times 10^{12}$ cm^{-3}) in the octupole allows the use of probes that can be placed directly in the plasma environment facilitating spatial scans. A variety of probes can be used to gain not only information about ion and electron temperature profiles, but also spatial information about wave amplitude and wavelength.

Ion heating can be unambiguously attributed to wave absorption in the octupole since there are negligible ohmic currents. These currents could otherwise produce increases in temperature from RF induced changes in plasma resistivity. This has been a difficulty in tokamak experiments.[14]

As mentioned earlier, the physics of the ion heating mechanism, question two above, has not been conclusively resolved to date by any experiment. However, strong evidence presented in this thesis indicates that most of the ion heating occurs after a mode conversion of the wave. Complicating effects cause an effective upshift of a large part of the $k_{\parallel}$ wave power spectrum. This lowers the values of density and magnetic field at which absorption occurs and at the same time produces some electron heating. A possible explanation of this anomaly will be discussed in the last chapter.

CHAPTER 2

THEORY OF LOWER HYBRID WAVE PROPAGATION AND ABSORPTION

The theory that will be outlined in this chapter serves as a basis for designing the experiment and interpreting the results to be described in subsequent chapters. As such, specific examples and graphs of the general theory will be presented in terms of octupole parameters.

Many of the theoretical results which follow can be found in the literature and will be referenced where this is the case. An attempt has been made here to collate these results and expand upon key points.

To begin with, the cold plasma model will be developed. Finite temperature corrections to this model will then be presented. To make the temperate plasma theory more tractable, the dielectric tensor is expanded to first order in k_x^2. Some of the important features of the lower hybrid wave can still be described under this approximation. In particular, the first turning point of the wave is adequately modeled.

In the second section, the wave differential equation is solved to find the wave electric fields in both a cold and a temperate plasma. Finally, the effects of collisions will be considered.

A. The Collisionless Model

We use a coordinate system in which the magnetic field is in the $\hat{z}$ direction, and a density gradient exists in the $\hat{x}$ direction. The plasma is assumed to be uniform in the $\hat{y}$ direction. The wave is incident from the low density edge of the plasma and propagates toward the plasma center. The Fourier analyzed form of the wave equation is given by,

$$\vec{n}(\vec{n}\cdot\vec{E}) - n^2\vec{E} + \overline{K}\cdot\vec{E} = 0 \tag{2.1}$$

where $\vec{n}=\vec{k}c/\omega$ and $\vec{E}$ is the Fourier analyzed electric field. For a cold plasma this is expanded as,

$$\begin{bmatrix} (n_z^2 + K_{xx}) & (iK_{xy}) & (n_x n_z) \\ (-iK_{xy}) & (-n_x^2 - n_z^2 + K_{xx}) & (0) \\ n_x n_z & (0) & (n_x^2 + K_{zz}) \end{bmatrix} \begin{bmatrix} E_x \\ E_y \\ E_z \end{bmatrix} = 0 \tag{2.2}$$

The following quadratic equation in n_x^2 results by setting the determinant of the coefficient of $\vec{E}$ equal to zero and taking $\omega_{ce} \gg \omega \gg \omega_{ci}$,

$$an_x^4 + bn_x^2 + c = 0 \tag{2.3a}$$

where,

$$a = K_{xx}, \qquad b = (K_{zz} + K_{xx})(n_z^3 - K_{xx}) + K_{xx}^2$$

$$c = (n_z^2 - K_{xx})^2 - K_{xy}^2$$

$$K_{xx} = 1 - \frac{\omega_{pi}^2}{\omega^2}\left(1 - \frac{\omega^2}{\omega_h^2}\right) \tag{2.3b}$$

$$K_{zz} = 1 - \frac{\omega^2_{pe}}{\omega^2}$$

$$K_{xy} = \frac{\omega^2_{pe}}{\omega\,\omega_{ce}}, \qquad \omega^2_h = \omega_{ci}\omega_{ce} \tag{2.3b}$$

Two solutions to Eqn.(2.3a) result,

$$n^2_x = \frac{-b \pm (b^2 - 4ac)^{\frac{1}{2}}}{2a} \tag{2.3c}$$

The larger root has a slower phase velocity and a resonance for $a = K_{xx} = 1 - \frac{\omega_{pi}^2}{\omega^2}\left(1 - \frac{\omega^2}{\omega_h^2}\right) = 0$. This is the root of interest in most experiments and is referred to as the slow mode. For $n_z = 0$ the slow mode becomes the usual extraordinary wave.

The smaller root of Eqn.(2.3) is referred to as the fast mode. For $n_z = 0$ it assumes the common form of the ordinary wave. In a uniform magnetic field the fast wave has no resonance based upon cold plasma theory. However, in a strongly non-uniform magnetic field, the fast wave does have a resonance.[22]

To analyze this situation we assume the following linear relation between density and the square of the magnetic field: $\omega_{ce}^2 = \omega_{ceo}^2 + \beta\omega_{pe}^2$, where $\beta = d\omega_{ce}^2/d\omega_{pe}^2$. Substituting this value for ω_{ce}^2 into the equation for the lower hybrid resonance, $K_{xx} = 1 + \omega_{pe}^2/\omega_{ce}^2 - \omega_{pi}^2/\omega^2 = 0$, yields a quadratic equation in ω_{pi}^2 which has solutions of the form,

$$\frac{\omega_{pi}^2}{\omega^2} = \frac{1}{2\beta}\left[-\left((\alpha^2 - 1) - \beta\right) \pm \left\{\left((\alpha^2 - 1) - \beta\right)^2 + \beta\alpha^2\right\}^{\frac{1}{2}}\right] \tag{2.4a}$$

where, $\alpha^2 = \frac{\omega_{ceo}\omega_{cio}}{\omega^2} = \frac{\omega_{ho}^2}{\omega^2}$.

We see that there are now two densities where resonance will occur. The plus solution will correspond to the slow wave resonance and the minus solution to the new fast wave resonance. Taking lim $\beta \to 0$ in Eqn. (2.4a), the fast wave solution goes to infinity so there is, in effect, no resonance which was the case in Eqn. (2.3c). Using L'Hospital's rule to take the same limit for the plus solution in Eqn. (2.4a) yields for the slow mode,

$$\frac{\omega_{pi}^2}{\omega^2} = \frac{\alpha^2}{\alpha^2 - 1}. \tag{2.4b}$$

Eqn. (2.4b) is just the usual slow mode lower hybrid resonance condition. This exercise shows that Eqn. (2.4a) reduces in the proper way as $\beta \to 0$.

In order that solutions to Eqn. (2.4a) will be real we require,

$$\left[\beta + (1 - \alpha)^2\right] \left[\beta + (1 + \alpha)^2\right] \geq 0 .$$

This will be true only if the square bracketed terms have the same sign. It is sufficient to require,

$$\beta > - (1 - \alpha)^2$$

or,

$$\beta < - (1 + \alpha)^2 .$$

The second inequality above yields negative values for both plus and minus solutions in Eqn. (2.4a) if we require that $\alpha^2 > 1$. This inequality must be rejected on physical grounds. The first inequality, on the other hand, yields positive real solutions for plus and minus signs unless $\beta > 0$. For $\beta > 0$ one solution is positive, (slow mode) and the other solution is negative (fast mode). If we are to have a fast wave resonance we must then satisfy,

$$0 > \frac{d\omega_{ce}^2}{d\omega_{pe}^2} > -(1 - \frac{\omega_{ho}^2}{\omega^2})^2 \qquad (2.4c)$$

when,

$$\frac{\omega_{ho}^2}{\omega^2} > 1$$

For the case $\omega_{ho}^2/\omega^2 < 1$, the quantity ω_{pi}^2/ω^2 will have either one positive real solution and one negative solution or else complex solutions as β is varied. None of these correspond to fast wave resonances, so we must additionally require the second inequality in Eqn. (2.4c).

Equation (2.4c) then, demonstrates that the magnetic field gradient must be opposite to the density gradient to excite a fast wave resonance. In addition, from Eqn. (2.4a) the density at which the fast mode occurs is greater than or equal to the density at which the slow mode occurs. The minimum resonant density for the fast mode exists for the steepest allowable magnetic field gradients ($\beta = -(1 - \alpha)^2$). Under this condition, the slow and fast mode resonances coalesce at a densty given by, $\frac{\omega_{pi}^2}{\omega^2} = \frac{\alpha}{\alpha - 1}$.

Fast wave resonances do exist for octupole conditions. However, as the above analysis shows, these resonances require that the wave follow paths into the plasma center from high magnetic field regions to low field regions ($\beta < 0$).

For waves launched from the lid region of the octupole, as is the case in our experiment, the ray trajectories are not suitable for direct excitation of fast wave resonances. Only waves reflected from the octupole hoops or from the wall in the nose region are capable of executing the right trajectories. Hence, it seems unlikely that the fast wave plays a role in heating of the ocutpole plasma. The above considerations justify primarily studying the slow lower hybrid mode throughout the remainder of this text.

Figure 1 shows the values of ω_{pi}^2/ω^2 versus ω_h^2/ω^2 at which the slow lower hybrid resonance exists.[22] We find that for high magnetic fields or, alternatively, low densites $(\omega_{pi}^2/\omega_h^2 << 1)$ the resonance lies along a constant density surface defined by $\omega^2 = \omega_{pi}^2$. On the other hand, for low magnetic fields or high densities $(\omega_{pi}^2/\omega_h^2 >> 1)$ the resonance lies along a constant $|\vec{B}|$ surface defined by $\omega^2 = \omega_{ce}\omega_{ci} = \omega_h^2$. No resonance exists when the magnetic field magnitude is below the value at which $\omega^2 = \omega_h^2$ or the density is less than the value defined by $\omega^2 = \omega_{pi}^2$. For the octupole plasma, we are constrained to density values less than about $n = 1 \times 10^{12} cm^{-3}$. This provides an upper bound on the practical operating frequency for our experiment of about $f \leq 170$ MHz, for $|\vec{B}| = 3.5$kG. A lower bound is found from the requirement that $\omega >> \omega_{ci}$. For the octupole this implies $f >> 8$MHz. In addition, so as not to impinge upon the plasma or interfere with other experiments or machine operation the launching structure needs to be as compact as possible, which is generally an easier task at higher frequencies. The higher frequencies, also, will allow heating of denser plasmas in general. Taking into account all of these factors, a frequency of $f = 140$ MHz was chosen.

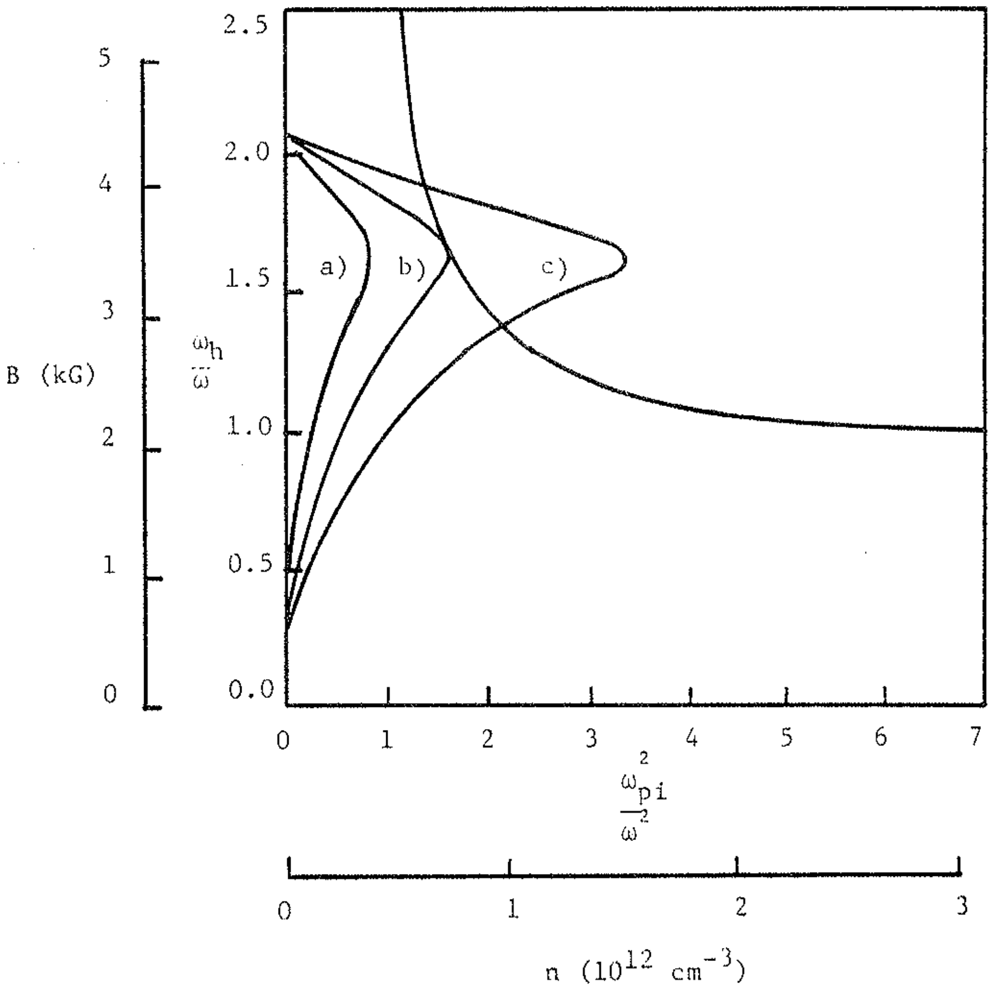

Figure 1. The line $K_{xx} = 0$ defining the lower hybrid resonance. Sample density profiles are superimposed (curves a,b,c)

The scales of density and magnetic field in Fig. 1 apply when the frequency equals this value. The parameters are within typical operating parameters.

Sample octupole density profiles are superimposed on Fig. 1 . Resonance occurs where the two curves intersect. This shows that resonance will result at the peak in the density profile when that peak is about $n = 7\times 10^{11}\text{cm}^{-3}$. The experiment will attempt to approach this favorable situation as close as possible. From Fig. 1 we also observe that resonance must occur in the higher magnetic field regions of the machine with $B > 2.0\,\text{kG}$. Finally, as the peak density is raised, the resonance can move out toward the edge of the density profile (profile c, Fig. 1). This later effect can produce edge heating and should be avoided.

With this qualitative picture of the lower hybrid resonance, we can construct the resonance surfaces on actual octupole flux plots as shown in Fig. 2 . At the optimum density of $n \simeq 7\times 10^{11}\text{cm}^{-3}$, resonance is entirely along the separatrix, while at higher densities the crescent shaped surfaces of Fig. 2b develop.

The minimum magnetic field values at the ends of the surfaces shown in Fig. 2 are given by $\omega_h^2 = \omega_{pi}^2/(\omega_{pi}^2/\omega^2 - 1)$ where ω_{pi}^2 is evaluated at this peak density. The width of the crescent at high densities ($n > 7\times 10^{11}\text{cm}^{-3}$) and in the high field region of the resonant surface (widest part of crescent) is given approximately by,

$$\frac{\Delta(\omega_{pi})^2}{\omega_{pi}^2} \simeq 2\left(1 - \frac{\omega_{pi}^2}{\omega^2}\right) \qquad (2.5)$$

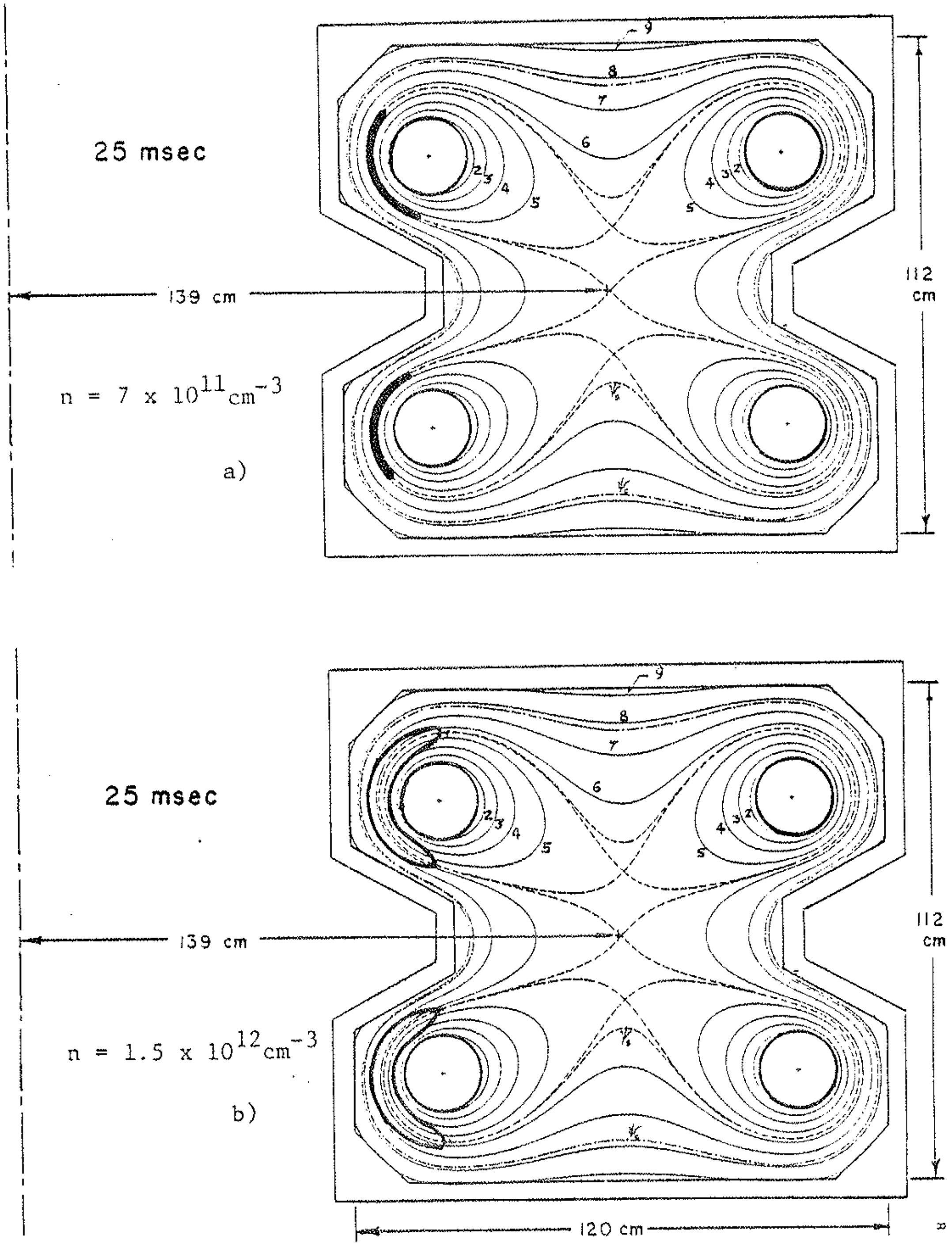
25 msec
139 cm
112 cm
n = 7 x 10^11 cm^-3
a)
1
2
3
4
5
6
7
8
9
25 msec
139 cm
112 cm
n = 1.5 x 10^12 cm^-3
b)
120 cm

Figure 2. Cold plasma lower hybrid resonant surfaces for maximum magnetic fields on the octupole.

Eqn. (2.5) applies when $\Delta\omega_{pi}^2/\omega_{pi}^2 > \omega^2/\omega_h^2$ where ω_h^2 is evaluated in the high field portion of the resonance surface and, as before, ω_{pi}^2 is evaluated at the peak density.

Thus far we have discussed wave behavior near the cold lower hybrid resonance and assumed the wave can propagate to this resonant layer. In actual fact only waves having a slow enough phase velocity along the magnetic field are able to propagate all the way to resonance. This condition can be written[22],

$$n_z^2 > 1 + \frac{\omega_{pe}^2}{\omega_{ce}^2} \tag{2.6}$$

where $\omega_{pe}^2/\omega_{ce}^2$ is evaluated at the lower hybrid resonance. Equation (2.6) can be derived from Egn. (2.3) by searching for values of n_z that make n_x^2 real inside the plasma. It is referred to as the "accessibility condition". Waves that do not satisfy this condition can propagate only in the low density surface regions of the plasma.

Waves that do satisfy Eqn. (2.6) still must pass through a thin evanescent region between zero density and the point along the density profile where $\omega = \omega_{pe}$. Since fields at the edge of this evanescent layer go like $\exp(-k_z x)$ field components with high k_z values will be affected more strongly by its presence.

For k_z values such that, $n_z > 3c/v_e$, where $v_e^2 = KT_e/m_e$ and c = velocity of light, appreciable electron Landau damping will absorb wave energy from the component of wave polarization along the magnetic field.[10, 23]. Thus, there is only a window in the n_z

spectrum of wave power that can propagate to the lower hybrid resonance.

For the octupole, a broad spectrum of n_z values is accessible to the resonance because of low electron temperatures. For rather typical experimental parameters, $T_e = 10\text{eV}$ and $n = 7 \times 10^{11}\ \text{cm}^{-3}$, the window of accessible n_z's is given by, $60 > n_z > 1.3$. In the experiment, our antenna is designed to have a peak in the n_z spectrum near $n_z \simeq 4$, which is well within the allowable bounds on n_z.

A.1. Hot Plasma Effects

The above cold plasma theory is useful for developing a simple preliminary picture of lower hybrid heating in the octupole. However it is really applicable only in the low density edge of the plasma where wavelengths are much longer than ion gyroradii. In the plasma interior, as wavelengths approach an ion gyroradius, hot plasma theory must be used.

Another shortcoming of cold plasma theory stems from the fact that the lower hybrid resonance is a wave resonance rather than a particle resonance. As such, energy accumulates in wave fields rather than particle motion, and so no heating can occur. This resonant field behavior may be analyzed from Eqn. (2.2) where,

$$\frac{E_x}{E_z} = \frac{n_x^2 - K_{zz}}{n_z n_x} \tag{2.7}$$

We find that $E_x \rightarrow \infty$ as $n_x \rightarrow \infty$ at the cold lower hybrid resonance, for a finite E_z. The wave field could not grow to this infinity if there were any dissipating of wave energy by the particles. This would introduce a wave damping term which would limit wave growth for finite input powers.

This phenomenom can also be seen by evaluating,

$$\vec{J}\cdot\vec{E} = \sigma_{xx}E_x^2 + \sigma_{zz}E_z^2$$

where,

$$\sigma_{xx} = i\omega\varepsilon_o\omega_{pi}^2\left(\frac{1}{\omega^2}-\frac{1}{\omega_h^2}\right) \tag{2.8}$$

$$\sigma_{zz} = i\varepsilon_o\frac{\omega_{ce}^2}{\omega}.$$

From this we recognize that $\vec{J}\cdot\vec{E}$ is a pure imaginary number and therefore no real power loss can occur. If collisions are included in the cold plasma theory, a loss mechanism for wave power will result. This will be discussed in section 2.3.

Finite gyroradius effects will provide us with a heating mechanism for a collisionless plasma. This situation is analyzed by making an electrostatic approximation, namely assuming $\vec{E} = -\vec{\nabla}\phi$. This will be a valid approximation in the interior of the plasma since the lower hybrid wave has $\vec{E}\,||\,\vec{k}$ there ($k_x >> k_z$ and $E_x >> E_z$). Under this approximation, the dispersion relation becomes,

$$n_x^2K_{xx} + 2n_xn_zK_{xz} + n_z^2K_{zz} = 0 \tag{2.9}$$

We use dielectric tensor elements from hot plasma theory given by,[24]

$$K_{xx} = 1 + \sum_{\alpha}\frac{\omega_{p\alpha}^2}{\omega k_z v_\alpha}e^{-\lambda_\alpha}\sum_{n=\infty}^{\infty}\frac{n^2}{\lambda^2}I_n(\lambda_\alpha)\,Z\,(\xi_n^\alpha)$$

$$K_{xz} = \sum_{\alpha} \frac{\omega_{p\alpha}^{2} k_x}{2\omega k_z^{2} \omega_{c\alpha}} e^{-\lambda_\alpha} \sum_{n=-\infty}^{\infty} \frac{n}{\lambda_\alpha} I_n(\lambda_\alpha) \; Z'(\xi_n^{\alpha})$$

$$K_{zz} = 1 - \sum_{\alpha} \frac{\omega_{p\alpha}^{2}}{\omega k_z^{2} v_\alpha^{2}} e^{-\lambda_\alpha} \sum_{n=-\infty}^{\infty} I_n(\lambda_\alpha) \; (\omega + n\omega_{c\alpha}) \; Z'(\xi_n^{\alpha})$$

where α refers to particle specie, $\lambda_\alpha = k_x^2 v_\alpha^2 / 2\omega_{c\alpha}^2$, $v_\alpha^2 = 2KT_\alpha / m_\alpha$, $\xi_n^{\alpha} = (\omega + n\omega_{c\alpha})/k_z v_\alpha$, I_n is the modified Bessel function, and Z is the plasma dispersion function. Substituting these dielectric tensor elements into Eqn. (2.9) yields an equation of the form,

$$1 + \sum_{\alpha} D^{\alpha} = 0 \tag{2.10a}$$

where,

$$D^{\alpha} = \frac{2\omega_{p\alpha}^{2}}{k^2 v_\alpha^2} e^{-\lambda_\alpha} \sum_{n=-\infty}^{\infty} I_n(\lambda_\alpha) \; (1 + \xi_o^{\alpha} Z(\xi_n^{\alpha})) = 0 \tag{2.10b}$$

This equation is really a modified form of the ion Bernstein dispersion relation, where a finite n_z is introduced into the equations. As such we might expect there to be some structure about the ion cyclotron harmonics.

In general, Eqn. (2.10a) must be solved numerically. A detailed study of this equation without approximation has been provided by Simonutti.[25] Brambilla makes an approximation to Eqn. (2.10), valid for $\lambda >> 1$ and $k_z v_\alpha / \omega_{c\alpha} >> 1$, that eliminates the need to calculate Bessel functions.[26]

In this thesis, a numerical solution of Eqn. (2.10) will not be attempted since it would produce little new information and is more appropriate to a theoretical thesis. Instead we will provide a rough idea of the salient features of the hot plasma theory.

We assume, first of all, that k_x and k_z are real and $\omega = \omega_r + i\omega_{im}$. We are interested in determining the temporal damping rate rather than the spacial damping rate because this will tell us if there is true absorption of wave energy as opposed to evanescence. We cannot distinguish an evanescent effect from a spacial damping effect having only a knowledge of the imaginary wave number.

We begin by assuming $\omega_i < \omega_r$. Total wave absorption can still occur in this "weak" damping approximation. We can write,

$$\omega_{im}^{\alpha} \simeq \frac{D_{im}^{\alpha}(\omega_r)}{\sum_{\alpha} \frac{\partial D_r^{\alpha}(\omega_r)}{\partial \omega r}} \qquad (2.11)$$

where D_{im}^{α} and D_r^{α} are the real and imaginary parts respectively of Eqn. (2.10b), which is evaluated for real requency, ω_r. Note that the total damping rate is given by the sum of electron and ion contributions, $\omega_{im} = \omega_{im}^{e} + \omega_{im}^{i}$. Using Eqn. (2.10), values for D_{im} and D_r will simplify as follows,[27]

$$D_{im}^{\alpha}(\omega_r) = \frac{2\sqrt{\pi}\,\omega_{p\alpha}^2}{k^2 v_\alpha^2}\,\xi_o^\alpha \sum_{n=-\infty}^{\infty} I_n(\lambda_\alpha)\, e^{-(\lambda_\alpha + (\xi_n^\alpha)^2)}$$

$$D_r^{\alpha}(\omega_r) = \frac{2\omega_{p\alpha}^2}{k^2 v_\alpha^2}\{1 + \xi_o^\alpha \sum_{n=-\infty}^{\infty} I_n(\lambda_\alpha)\, e^{-(\lambda_\alpha + (\xi_n^\alpha)^2}\} \qquad (2.13)$$

$$\times \; i\sqrt{\pi}\, \mathrm{erf}\, (i\xi_n^\alpha)$$

where $\xi_n^\alpha = (\omega_r - n\omega_{c\alpha})/k_z v_\alpha$, erf if the error function, and we have used the value of Z for real arguments. Using the fact that $\partial \mathrm{erf}(z)/\partial z = 2\pi^{-\frac{1}{2}}\exp(-z)^2$ we can write,

$$\frac{\partial D_r^{\alpha}(\omega_r)}{\partial \omega_r} = \frac{2\omega_{p\alpha}^{2}}{k_z v_\alpha} \frac{i\sqrt{\pi}}{k^2 v_\alpha^2} \sum_{n=-\infty}^{\infty} I_n(\lambda_\alpha)\, e^{-\lambda\alpha}$$

$$x \left\{ e^{-(\xi_n^{\alpha})^2} \mathrm{erf}\, (i\xi_n^{\alpha})\ (1 - 2\xi_o^{\alpha}(\xi_n^{\alpha}) + \frac{2i\xi_o^{\alpha}}{\pi^{1/2}} \right\} \qquad (2.14)$$

We first consider the contribution to wave damping by the ions. In this case, the dominant term in Eqn. (2.12) (for a fixed value of λ_i) will occur for the minimum value of ξ_n^i. This occurs when ω is sufficiently close to an ion cyclotron harmonic. Through this behavior we conclude that the damping mechanism is ion cyclotron damping at a high harmonic of the ion cyclotron frequency (since $\omega >> \omega_{ci}$ has been assumed).

Another important feature is that in the limit as $k_z \to 0$ (or $\xi_n^{\alpha} \to \infty$) all the terms in Eqn. (2.12) vanish, and Eqn (2.14) diverges ($\xi_o^{\alpha} \to \infty$). Thus, no damping occurs if the wave phase velocity is exactly perpendicular to the magnetic field. This is an important characteristic which will distinguish this theory from the straight line ion orbit treatment, to be described later.

The requirement that ω be close to an ion cyclotron harmonic is easily satisfied in the octupole. In fact, near the lower hybrid resonant layer, confining magnetic field amplitude variations are such that the wave frequency will be close to twenty different ion cyclotron harmonics between $\omega = 25\omega_{ci}$ and $\omega = 45\omega_{ci}$. Strong ion damping is thus expected. Of course, some variations in the exact magnitude of the damping will occur, depending upon the value of λ_i

at the point in the plasma where an ion cyclotron harmonic is encountered.[28]

Since $\lambda_e/\lambda_i = m_e/m_i$ we can take $\lambda_e << 1$ and obtain an accurate representation of electron dynamics over the region between the plasma edge and the point along the density profile where λ_i is on the order ten, which covers most of the wave interaction region. Under their approximation, the Bessel function in the electron term of Eqn. (2.12) can be approximated as $I_n(\lambda_e) \simeq (\lambda_e/2)^n/n!$. From this we see that I_o will be the largest Bessel function in the summation. Also, $(\xi_n^e)^2 >> (\xi_o^e)^2$ for $n \neq 0$. Because of this, an examination of Eqn. (2.12) reveals that the $n = 0$ term will be the most important term in the summation. D_{im}^e can then be simplified as,

$$D_{im}^e \simeq \frac{2\sqrt{\pi}\,\omega_{pe}^2}{k^2 v_e^2}\, I_o(\lambda_e)\, e^{-\lambda_e}\, \xi_o^e\, e^{-(\xi_o^e)^2} \qquad (2.15)$$

The quantity $\partial D_r^e/\partial\omega_r$, in turn, can be written,

$$\frac{\partial D_r^e}{\partial\omega_r} \simeq \frac{2\omega_{pe}^2}{k^2 v_e^2}\,\frac{i\pi^{\frac{1}{2}}}{k_z v_e}\, I_o(\lambda_e)\, e^{-\lambda_e}\, \{\mathrm{erf}\,(i\xi_o^e)\, e^{-(\xi_o^e)^2}(1 - 2\,(\xi_o^e)^2) + \frac{2i\xi_o^e}{\pi^{\frac{1}{2}}}\} \qquad (2.16)$$

Further simplifications result by assuming that $\xi_o^e >> 1$. In this limit, $\mathrm{erf}\,(i\xi_o^e) \to (-1)/(\pi^{\frac{1}{2}} i\xi_o^e)\, \exp\,(\xi_o^e)^2$ and Eqn. (2.16) can be written,

$$\frac{\partial D_r^e}{\partial\omega_r} \simeq -\,\frac{2\omega_{pe}^2}{k^2 v_e^2\,\omega}\, I_o(\lambda_e)\, e^{-\lambda_e} \qquad (2.17)$$

The final expression for the electron damping rate then becomes,

$$\omega_{im} \simeq \frac{\dfrac{2\pi^{\frac{1}{2}}\omega_{pe}^{2}}{k^{2}v_{e}^{2}}\ \xi_{o}^{e}\ I_{o}(\lambda_{e})\ e^{-\lambda_{e}-(\xi_{o}^{e})^{2}}}{\dfrac{\partial D_{r}^{i}}{\partial\omega_{r}} + \dfrac{2\omega_{pe}^{2}}{k^{2}v_{e}^{2}\omega}\ I_{o}\ (\lambda_{e})\ e^{-\lambda_{e}}} \qquad (2.18)$$

Unfortunately, the ion term does not simplify in the present case. However, it can be held fixed while ξ_{o}^{e} is varied since the electron thermal velocity is independent of any variable in $\partial D_{r}^{i}/\partial\omega_{r}$. Because of the exponential function of $-(\xi_{o}^{e})^{2}$ in the numerator of Eqn. (2.18) and the fact that the denominator is insensitive to changes in $\xi_{o}^{e} = \omega/k_{z}v_{e}$ for fixed v_{e}, we see the relation of the electron damping process in this case to ordinary Laundau damping. Namely, as the wave phase velocity approaches the electron thermal velocity, the damping rate becomes appreciable.

A.2. Unmagnetized Ion Approximation

It is apparent from the above analysis that both the ion and electron contributions to wave damping are, in general, very complicated functions. In attempts to simplify the situation, what is often done is to assume that the ions are unmagnetized and so execute straight line orbits.[23] Electrons, on the other hand, remain magnetized and are treated much as they were before.

Since wavelengths can be much less than an ion gyroradius and the frequency is much greater than the ion cyclotron frequency, this may seem, at first glance, to be a reasonable approximation, particularly if the wave damps away on a time scale less than an ion gyroperiod ($\omega_{im} >> \omega_{ci}$). We can obtain the desired approximate result by taking $\omega_{ci} = 0$ for the ion term in the general dispersion relation, Eqn. (2.10). This yields,

$$D^i = \frac{2\omega_{pi}}{k^2 v_i^2} \left(1 + \xi_o^i \, Z\,(\xi_o^i)\right). \qquad (2.19)$$

We have used the fact that $\sum I_n(\lambda_i) = \exp(\lambda_i)$ in obtaining Eqn. (2.19). Using once again the expansion of the plasma dispersion function for real arguments, we can obtain from Eqn. (2.19),

$$D^i_{im}(\omega_r) = \frac{2\sqrt{\pi}\,\omega_{pi}^2}{k^2 v_i^2} \, \xi_o^i \, e^{-(\xi_o^i)} \qquad (2.20)$$

$$D^i_r(\omega_r) = \frac{2\omega_{pi}^2}{k^2 v_i^2} \left(1 + \xi_o^i \, i\pi^{\frac{1}{2}} \, e^{-(\xi_o^i)} \, \mathrm{erf}\,(i\xi_0^i)\right) \qquad (2.21)$$

Taking $\omega_{ci} = 0$ for the ion term in Eqn. (2.14), in turn, yields,

$$\frac{\partial D_r(\omega_r)}{\partial \omega_r} = \frac{2\omega_{pi}^2}{k^2 v_i^2} \, \frac{i\pi^{\frac{1}{2}}}{k_z v_i} \left\{ e^{-(\xi_o^i)^2} \mathrm{erf}\,(i\xi_o^i) \, (1 - 2(\xi_o^i)^2 + \frac{2i\xi_o^i}{\pi^{\frac{1}{2}}} \right\} \qquad (2.22)$$

Now if we assume $\xi_o^i = \omega/k_z v_i >> 1$ then we can simplify Eqn. (2.22) as follows,

$$\frac{\partial D_r}{\partial \omega_r} \simeq \frac{2\omega_{pi}^2}{k^2 v_i^2 \omega} \qquad (2.23)$$

Retaining the former assumption that $\xi_o^e = \omega/k_z v_e >> 1$ we can use Eqns. (2.15) and (2.17) that have already been derived. The damping rate for ions can now be written explicitly by combining Eqns. (2.11), (2.17) and (2.23) to give,

$$\frac{\omega_{im}^{i}}{\omega} \quad \frac{\pi^{\frac{1}{2}}\xi_o^i \; e^{-(\xi_o^i)^2}}{1 + \frac{T_i}{T_e} I_o(\lambda_e) \; e^{-\lambda_e}} \tag{2.24}$$

The electron damping term can be obtained under the assumption that $\xi_o^e >> 1$ from Eqn. (2.18) and using the new simplified form for $\partial D_r^i/\partial\omega_r$ in Eqn. (2.23). This will give,

$$\frac{\omega_{im}^{e}}{\omega} \simeq \frac{\pi^{\frac{1}{2}}\xi_o^e \; I_o \; (\lambda_e) \; e^{-\lambda \; -(\xi_o^e)^2}}{\{ \frac{T_e}{T_i} \; + I_o(\lambda_e) \; e^{-\lambda_e} \}} \tag{2.25}$$

We now have simple analytic forms for the damping rates. A new phenomenon becomes apparent for the ion damping term, indicated in Eqn (2.24). Wave absorption will now become large as the quantity $\xi_o^i = \omega/kv_i$ decreases. This process is thus ion Landau damping with the difference that it occurs across the magnetic field lines rather than along the field lines. (We can speak of a magnetic field for wave damping by ions because a magnetic field was retained for electrons, which have a contribution to the ion damping term, Eqn. (2.24), and define the direction of $\vec{k}$.).

It should also be pointed out that for the ion term in the dispersion relation, Eqn. (2.19), k_z and k_x become identical when the magnetic field vanishes. This is because our dispersion relation is a local approximation for a uniform plasma. Therefore, when $B = 0$ there is no distinguishing feature defining a $\hat{z}$ and an $\hat{x}$ direction.

Equations (2.24) and (2.25) differ slightly from the results of Glagolev.[23] This is primarily because of the order in which the derivative $\partial D_r^\alpha/\partial\omega_r$ was taken. In this paper, the derivative of the general dispersion relation, Eqn. (2.10), was first taken, and then the limit $\omega_{ci} \rightarrow 0$ was used to simplify the resulting expression. Glagolev essentially takes the limit $\omega_{ci} \rightarrow 0$ first and then takes the derivative of the resulting expression for D_r^α. In any event, Glagolev must retain two terms in the asymptotic expansion of the real part of the plasma dispersion function to obtain finite results. In the present case, however, only a single term in the expansion is necessary to obtain a reasonable approximation.

An interesting feature that is apparent from Eqns. (2.24) and (2.25) is that the ion damping will be largest where k is largest (ξ_o^i is smallest). On the other hand because of the factor $\exp(-\lambda_e)$ in the electron damping term, Eqn. (2.25), electron damping will be largest for the smallest value of $k \simeq k_x$ for a fixed value of $\xi_o^e = \omega/k_z v_e$, and assuming $k_z \ll k_x$. Since $|\vec{k}|$ generally increases as the wave propagates from the plasma edge into an increasing density, this implies that electrons will be heated near the edge of the plasma, while ions will be heated closer to the center of the plasma.

A sharply peaked electron temperature profile could allow greater penetration of the wave before any elctron absorption would occur. This would be the case, for example, if the electron temperature increased at such a rate that the value of the quantity

$(\lambda_e + \xi_o^e)$ decreased from the edge toward the center of the plasma. In any event, from this fact we see that the electron and ion energy deposition profiles will be important features, useful in identifying the absorption mechanism in the experiment.

Before going on, some of the limitations of the straight ion orbit approximation should be mentioned. First of all, it is really a fair approximation only in its description of the real part of the dispersion relation and only to first order in k_x^2. As will be shown later, this is because in the actual first order expansion of the dispersion relation, the magnetic field disappears from the ion terms without directly assuming that $\omega_{ci} = 0$ (typically, ω_{ci} appears added to ω, but since $\omega >> \omega_{ci}$ the ω_{ci} quantity is neglected). It can be shown that for higher order expansions of the dielectric tensor elements in powers of k_x^2, the magnetic field cannot be neglected. Therefore, the straight line ion orbit treatment becomes invalid for very large values of k_x^2.

The neglect of the magnetic field in the ion term is a poor approximation in analyzing the imaginary part of the dispersion relation for all k_x^2 values. As we have seen from Eqn. (2.10). which is a more exact treatment that retains both the magnetic field and the higher order terms in k_x^2, strong ion damping is critically dependent upon being in the vicinity of an ion cyclotron harmonic. There can be no such dependence for unmagnetized ions in the present approximation. In addition, we found from the exact treatment that in the limit $k_z \to 0$, the ion damping vanishes.

However, in the straight ion orbit case, there is no such dependence upon k_z. In fact, damping is still appreciable for $k_z = 0$ (see Eqn. (2.24). Thus, there is no straightforward connection between the theory for magnetized ions and the theory for unmagnetized ions.

Nonetheless, as pointed out by Simonetti[25], there may be situations in a real experiment where the zero order ion orbits deviate significantly from precise helices. In this case, neither Eqn.(2.10), which is derived under the assumption of exact, helical zero order ion motion, nor Eqn. (2.19) for straight line orbits will provide a precise description. Rather they may model the extremes of the situation In this light, the ion damping description from an unmagnetized ion treatment may be useful.

A.3. First Order Approximation

We turn now to one final approximation to the dispersion relation, which bears similarities to the straight line ion orbit case just considered in its description of the real part of the dispersion relation. Still using the electrostatic approximation, the relevant equation is given by Eqn. (2.9). We expand the dielectric tensor elements to first order in k_x^2 which yields,

$$\begin{aligned} K_{xx} &\simeq K_{xx}^{0} + K'_{xx}k_x^2 \\ K_{xz} &\simeq K_{xz}^{o} + K'_{xz}k_x^2 \qquad 2.26) \\ K_{zz} &\simeq K_{zz}^{o} + K'_{zz}k_x^2 \end{aligned}$$

where,

$$K_{xx}^{o} = 1 + \frac{\omega_{pe}^{2}}{\omega_{ce}^{2}} - \frac{\omega_{pi}^{2}}{\omega^{2}}$$

$$K_{xz}^{o} = -\left(\frac{\omega_{pe}^{2}}{\omega_{ce}^{2}}\frac{v_e^2}{\omega_{ce}^{2}} + \frac{\omega_{pi}^{2}}{\omega^2}\frac{v_i^2}{\omega^2}\right)k_x k_z$$

$$K_{zz}^{o} = 1 - \frac{\omega_{pi}^{2}}{\omega^{2}} - \frac{\omega_{pe}^{2}}{\omega^{2}}$$

$$K'_{xx} = \frac{\partial K_{xx}}{\partial k_x^2}\bigg|_{k_x=0} = -3\frac{\omega_{pi}^{2}}{\omega^2}\frac{v_i^2}{\omega^2} - \frac{3}{4}\frac{\omega_{pe}^{2}}{\omega_{ce}^{2}}\frac{v_e^2}{\omega_{ce}^{2}} \tag{2.27}$$

$$K'_{xz} = \frac{\partial K'_{xz}}{\partial k_x^2}\bigg|_{k_x=0} = -\left(12\frac{\omega_{pi}^{2}}{\omega^2}\frac{v_i^4}{\omega^4} - \frac{45}{8}\frac{\omega_{pe}^{2}}{\omega_{ce}^{2}}\frac{v_e^4}{\omega_{ce}^{4}}\right)k_x k_z$$

$$K'_{zz} = \frac{\partial K_{zz}}{\partial k_x^2}\bigg|_{k_x=0} = -\frac{\omega_{pi}^{2}}{\omega^2}\frac{v_i^2}{\omega^2} + \frac{\omega_{pe}^{2}}{\omega^2}\frac{v_e^2}{\omega_{ce}^{2}}$$

Substituting these values for the dielectric tensor elements into Eqn. (2.9) and assuming $\omega/k_z v_i >> 1$ and $\omega/k_z v_e >> 1$ yields the approximate dispersion relation[30],

$$K'_{xx}k_x^4 + K_{xx}^{o}k_x^2 + K_{zz}^{o}k_z^2 = 0 \tag{2.28}$$

Note that taking $T_e = T_i = 0$ in this equation yields the fluid plasma electrostatic dispersion relation with $\nabla p=0$,

$$k_x^2 = -\frac{K_{zz}^{o}}{K_{xx}^{o}}k_z^2 \tag{2.29}$$

Eqn. (2.28) will be valid up to some maximum value of k_x^2. This maximum will be determined by the degree of linearity of the tensor elements with respect to k_x^2. From the numerical results of

Simonutti[25], Eqn. (2.28) appears to be a fair approximation at least up to the first turning point of the wave. For $k_z v_e/\omega < 0.1$ it is a good approximation nearly to the point where $k_x^2 v_i^2/\omega^2 \simeq 1$. Above this value, Eqn. (2.28) is no longer valid.

Having obtained a rough idea of the range of validity of Eqn. (2.28), we plot k_x versus density in Fig. 3 as determined from Eqn. (2.28). Representative curves are shown for $k_z v_e/\omega = 0.29$ and $k_z v_e/\omega = 0.16$ with $\omega/\omega_{ci} = 41.9$. The dashed curves show results that are predicted from the fluid theory, Eqn. (2.29). As shown in Fig.3, the wave propagates along the fluid plasma branch as a backward wave until it reaches a critical density where a significant deviation from the fluid theory occurs. It then turns around and propagates back out of the plasma as a forward wave along the thermal branch of the dispersion relation. The point where this conversion from a backward wave to a forward wave occurs is referred to as the turning point. The whole process is referred to as "mode conversion" in the literature.[1,23] The plasma parameters that occur at the turning point have been calculated by Simonutti.[31] They may be obtained from Eqn. (2.28) by solving for k_x^2 and then taking $\partial k_x^2/\partial \omega_p^2 \rightarrow \infty$. The condition that must be satisfied at the turning point is then,

$$(K_{xx}^{o})^2 = -4K'_{xx} k_z^2 \qquad (2.31)$$

In terms of plasma parameters this becomes,

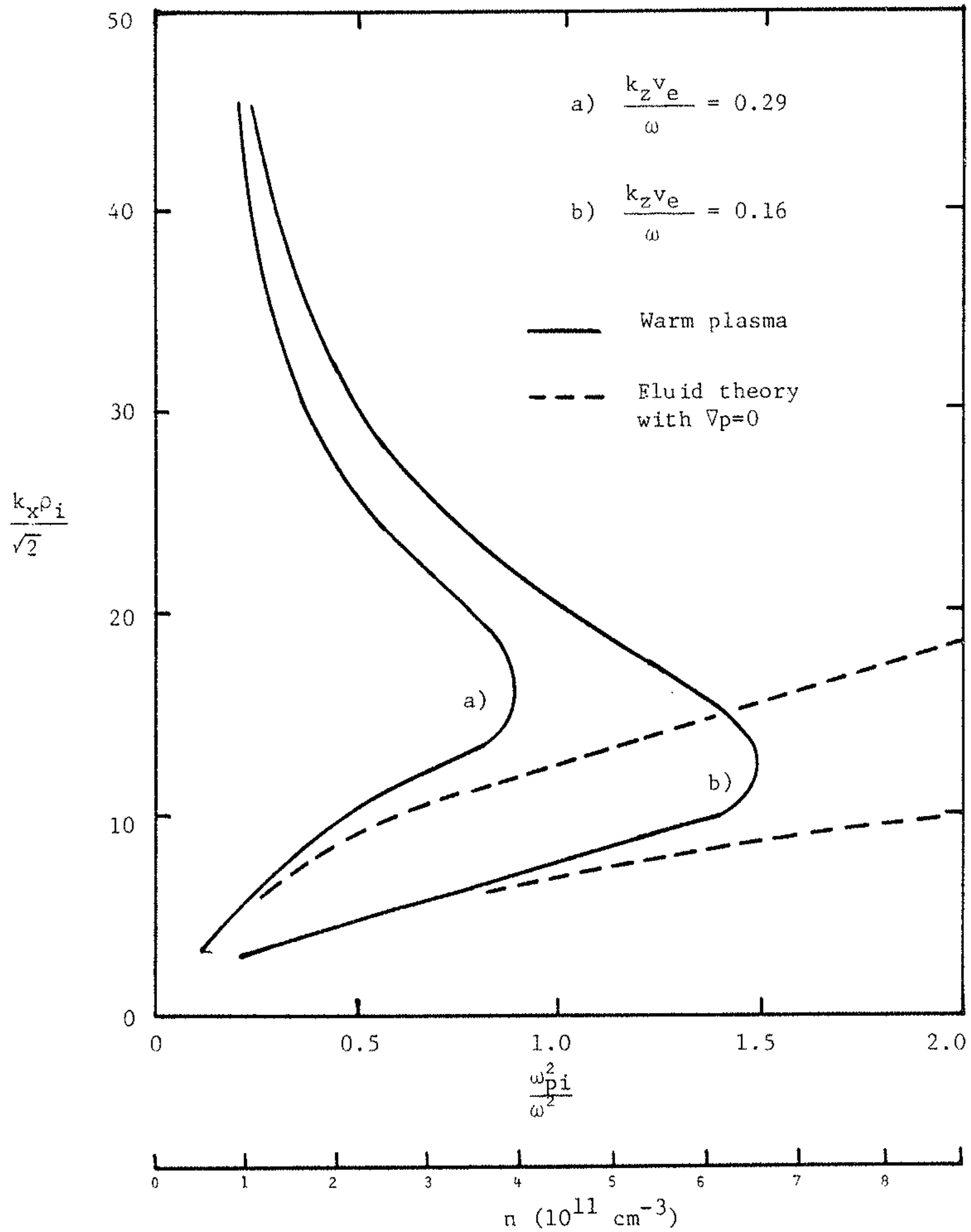

Figure 3. Warm plasma dispersion relation (B=2.2kG, f_o=140MHz).

$$\frac{\omega_{pi}^2}{\omega^2} \quad \left(1 + \frac{\omega_{pi}^2}{\omega_h^2}\right)\left[1 + 2\sqrt{3}\,\frac{k_z v_e}{\omega}\left(\frac{T_i}{T_e}\right)^{\frac{1}{2}}\left(1 + \frac{1}{4}\,\frac{T_e}{T_i}\,\frac{\omega^4}{\omega_h^4}\right)^{\frac{1}{2}}\right]^{-1} . \qquad (2.32)$$

Sample parameters at which the turning point occurs are plotted in Fig. 4. We have chosen the same values of $k_z v_e/\omega$ as in Fig.3. Also shown for comparison is the cold plasma resonance. It is seen that the maximum density to which the wave can penetrate decreases with increasing k_z and can be well below the cold plasma value for large k_z. This will be an important consideration in interpreting experimental results.

The value of k_x^2 at the turning point can be calculated by solving, once again, Eqn. (2.28) for k_x^2 and then using Eqn. (2.31). This yields,

$$k_x^2 = k_z\left(-\frac{K_{zz}^o}{K_{xx}'}\right)^{\frac{1}{2}} \qquad (2.33)$$

In terms of plasma parameters Eqn. (2.33) can be written,

$$\frac{k_x^2 v_i^2}{\omega_{ci}^2} = \frac{1}{\sqrt{3}}\;\frac{k_z v_e}{\omega}\,\frac{\omega^2}{\omega_{ci}^2}\left(1 + \frac{1}{4}\,\frac{T_e}{T_i}\,\frac{\omega^4}{\omega_h^4}\right)^{-\frac{1}{2}} \qquad (2.34)$$

where ω_{ci} and ω_h are evaluated at the wave turning point. From this result, we plot $k_x v_i/\omega_{ci}$ versus ω_{ci}/ω in Fig. 5. We observe that k_x increases with decreasing magnetic field and with decreasing k_z.

All of the above information on the turning point is useful in obtaining an idea of how the dispersion relation changes under

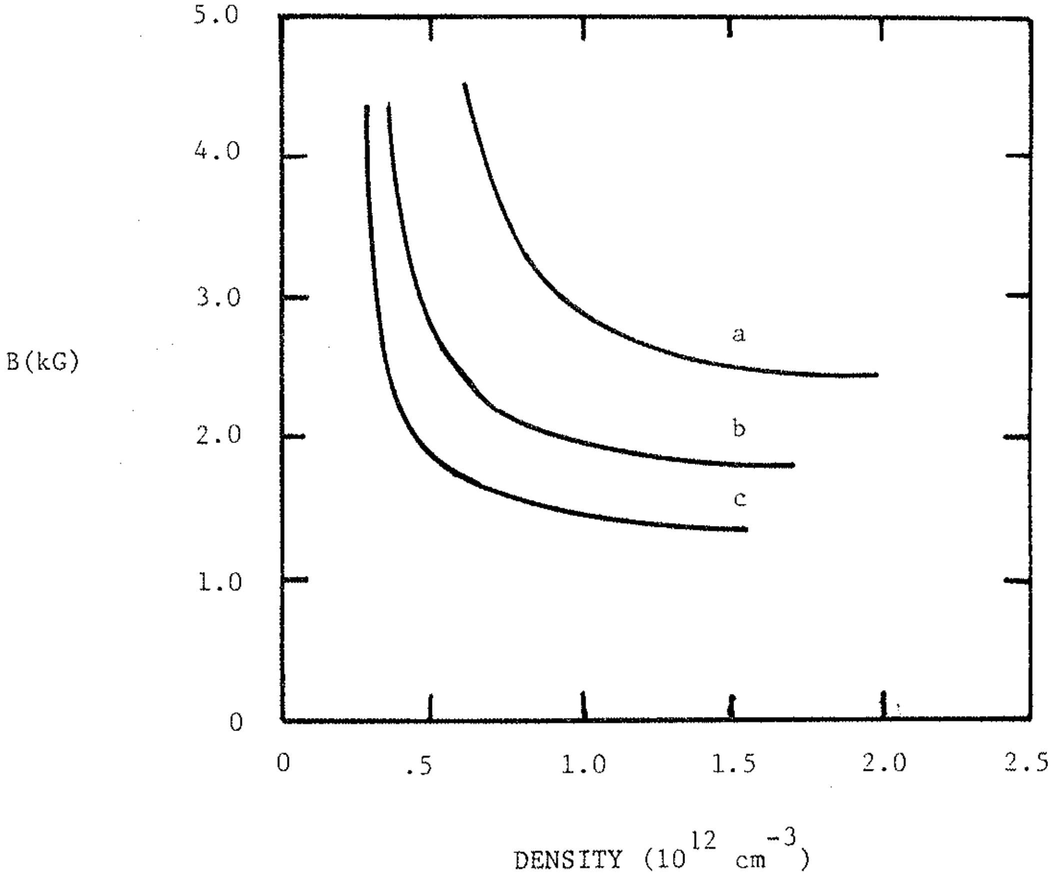

a. $k_z v_e/\omega = 0$

b. $k_z v_e/\omega = 0.16$

c. $k_z v_e/\omega = 0.3$

Figure 4. Density versus magnetic field at which mode conversion occurs for a wave frequency of 140 MHz. Curve (a) defines the cold plasma resonance.

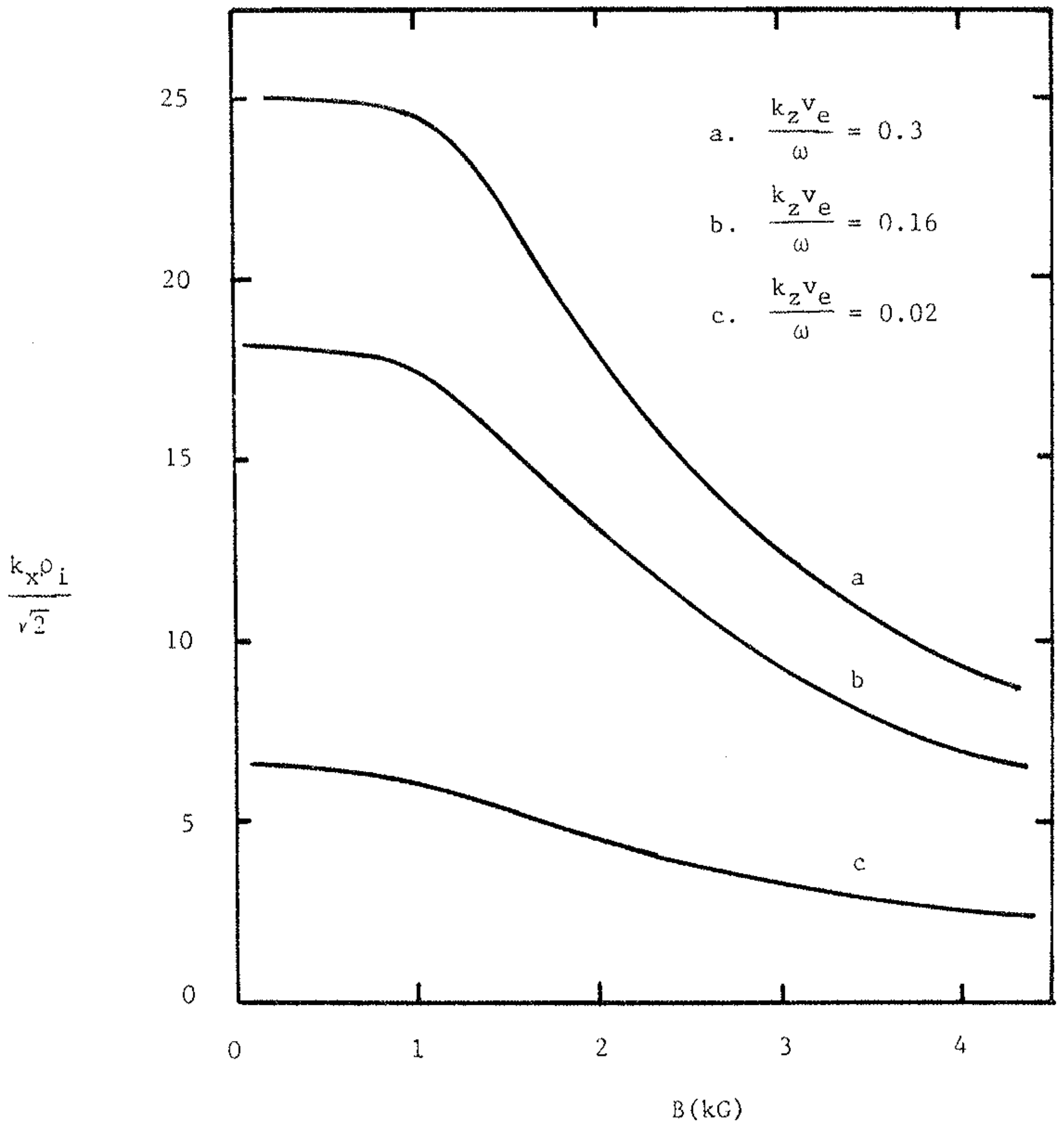

Figure 5. $k_x \rho_i/\sqrt{2}$ at the lower hybrid turning point versus magnetic field at the turning point for three values of $k_z v_e/\omega$.

a variety of conditions. The turning point in turn is important because it marks the point along the dispersion curve where ion damping can start as the wave continues up the thermal branch of the dispersion curve. Thus, it will be useful to compare energy deposition profiles in the experiment with the turning point of the wave. This procedure has the benefit that it provides a simple and convenient means of obtaining a rough comparison between our theoretical expectations and the actual experimental results.

B. Wave Fields

B.1. Cold Plasma Model

Briggs and Parker have demonstrated from cold plasma theory that the lower hybrid wave energy tends to follow narrow channels referred to as the resonance cones.[11] If fields at the plasma edge have any singularities, the field in the resonance cones will also have singularities. The less singular the excitation at the edge, the less singular will be the fields in the resonance cones, in general.

Of course, under more realistic assumptions there will be a limit to how sharply peaked this electric field can become. The k_z spectrum for the electric field broadens as the field becomes more peaked. Eventually, k_z values will be large enough to allow Landau damping and further field peaking is thereby inhibited. This effect would become apparent from a hot plasma treatment. The procedure for analyzing hot plasma fields will be outlined later in this section.

One of the simplest forms that a resonance cone takes is found for a uniform cold plasma.[10] In the electrostatic limit the differential equation governing wave behavior is given by,

$$\frac{\partial^2\phi}{\partial x^2} = -\frac{K_{zz}}{K_{xx}}\frac{\partial^2\phi}{\partial x^2} \qquad (2.37)$$

It is easy to see that solutions of this equation have the general functional dependence, $\phi = \phi(z \pm (-K_{zz}/K_{xx})^{\frac{1}{2}} x)$. Therefore values of constant potential lie along a conical surface defined by $(z \pm (-K_{zz}/k_{xx})^{\frac{1}{2}} x)$. This surface is the resonace cone.

The next step up in complexity is to allow the plasma to be non-uniform. The following analysis of this problem is an amplification of the results of Briggs and Parker.[11] The differential equation that must now be solved is,

$$\frac{\partial}{\partial x}\left(K_{xx}\frac{\partial}{\partial x}\phi\right) + \frac{\partial}{\partial z}\left(K_{zz}\frac{\partial}{\partial z}\phi\right) = 0 \qquad (2.38)$$

Taking the plasma to be uniform in the $\hat{z}$ direction allows us to easily take the Fourier transform of Eqn. (2.38) in the $\hat{z}$ direction yielding,

$$\frac{\partial^2\phi}{\partial x^2} + \frac{1}{K_{xx}}\frac{\partial K_{xx}}{\partial x}\frac{\partial\hat{\phi}}{\partial x} - k_z^2\frac{Kzz}{K_{xx}}\hat{\phi} = 0 \qquad (2.39)$$

where,

$$\hat{\phi}(x,k_z) = \int_{-\infty}^{\infty} \phi(x,z)\; e^{-ik_z z} dz$$

We now take solutions of Eqn. (2.39) to be of the form,

$$\hat{\phi} = u(x)p(x) \tag{2.40}$$

where,

$$\begin{aligned} p(x) &= \exp(-\tfrac{1}{2} \int_{o}^{x} \frac{1}{K_{xx}}\, dx + \sigma) \\ &= e^{\sigma}(K_{xx}(x))^{-\frac{1}{2}}. \end{aligned} \tag{2.41}$$

The quantity σ is a constant of integration that will be determined from the boundary conditions. Equation (2.39) becomes an equation for u(x) given by,

$$\frac{\partial^2 u}{\partial x^2} + f(x)u = 0 \tag{2.42}$$

where,

$$f(x) = -\frac{1}{2K_{xx}} \frac{\partial^2 K_{xx}}{\partial x^2} \quad \frac{1}{4} \frac{1}{K_{xx}^2} (\frac{\partial K_{xx}}{\partial x})^2 - k_z^2 \frac{K_{zz}}{K_{xx}} \tag{2.43}$$

This equation may be solved approximately using the WKB method.[32] Accordingly, solutions will be of the form,

$$u(x) = \frac{1}{(f(x))^{\frac{1}{4}}} \left[c_+ \exp(i\int (f(x)^{\frac{1}{2}}\, dx) + c_- \exp(-i\int (f(x)^{\frac{1}{2}}\, dx) \right] \tag{2.44}$$

Looking for waves that travel only in one direction, the constant c_- can be taken to be zero. The indefinite integral can be changed to a definite integral over the region from zero to x. The constant of integration left over from this change, together with the constant in Eqn. (2.41) can be absorbed into the constant c_+. This constant, in turn, is determined by the boundary conditions, $\hat{\Phi}(o,k_z) = p(o)\ u(o) = c_+((f(o))^{\frac{1}{2}} K_{xx}(o)\ )^{-\frac{1}{2}}$. Using Eqns. (2.40) and (2.42) the final expression for the wave potential results[11],

$$\hat{\Phi}\ (x,k_z) = \hat{\Phi}(o,k_z) \left(\frac{K_{xx}(o)(f(o))^{\frac{1}{2}}}{K_{xx}(x)(f(x))^{\frac{1}{2}}}\right)^{\frac{1}{2}} e^{\int_o^x (f(x))^{\frac{1}{2}}\, dx} \qquad (2.45)$$

Now in order to satisfy the WKB criterion, the quantity f(x) must be a slowly varying function, over one "wavelength". In order to satisfy this requirement, we first impose the constraint that the scale length for variation in K_{xx} be large enough that,

$$\frac{1}{K_{xx}^2}\left(\frac{\partial K_{xx}}{\partial x}\right)^2 << k_z^2 \left|\frac{K_{zz}}{K_{xx}}\right|. \qquad (2.46)$$

Also, the curvature in the density profile is taken to be slight so that,

$$\frac{1}{K_{xx}} \frac{\partial^2 K_{xx}}{\partial x^2} << k_z^2 \left|\frac{K_{zz}}{K_{xx}}\right|. \qquad (2.47)$$

With these conditions imposed the quantity $(f(x))^{\frac{1}{2}}$ becomes,

$$(f(x))^{\frac{1}{2}} = |k_z| (- \frac{K_{zz}}{K_{xx}})^{\frac{1}{2}}. \qquad (2.48)$$

Identifying f(x) with the wave number k_x^2, the WKB approximation will be valid for,

$$\left|\frac{\partial k_x}{\partial x}\right| << \left|k_x^2\right| \qquad (2.49)$$

and,

$$\left|\frac{\partial^2 k_x}{\partial x^2}\right| << \left|k_x\right| \left|\frac{\partial k_x}{\partial x}\right| \qquad (2.50)$$

It is found that the WKB theory will break down near the lower hybrid resonance since the dielectric tensor elements change very rapidly there, and Eqns. (2.46), (2.47), (2.49) and (2.50) are violated. WKB can also break down near the edge of the plasma where k_x can become very small relative to its derivative.

Cold plasma theory will break down near the mode conversion point of the wave, rendering the above results invalid near this point in the plasma. Finally, near the edge of the plasma, where wavelengths can approach free space values, the electrostatic approximation can breakdown. In this case the theory will be valid only over a portion of the wave trajectory in the plasma interior. We could not make a connection with the boundary electric field and the interior electric field without including electromagnetic corrections.

In any event,it is easy to show from Eqn. (2.45) that a singular electric field near the plasma edge will produce singularities along the resonance cone channels. Modeling the boundary field as a delta function, $\phi(o,z) = \delta(z)$, we can write the Fourier transform of the potential as,

$$\mathcal{F}\phi(x,z) = B(x)\left(H(k_z)\, e^{ik_z g(x)} + (1 - H(k_z))\, e^{-ik_z g(x)}\right) \qquad (2.50a)$$

where $H(k_z)$ is the heaviside function, $\mathcal{F}$ is the Fourier transform operator and

$$B(x) = \left(\frac{K_{xx}(o)\ K_{zz}(o)}{K_{xx}(x)\ K_{zz}(x)}\right)^{\frac{1}{4}} .$$

Mutiplying both sides of Eqn. (2.50a) by $\exp(-c|k_z|)$ and taking the inverse Fourier transform yields,

$$\frac{1}{2\pi}\left(\int_o^\infty \mathcal{F}\phi(x,z-ic)\ e^{ik_z z}\ dk_z + \int_{-\infty}^{o} \mathcal{F}\phi(x,z+ic)\ e^{ik_z z}\ dk_z\right)$$

$$= B(x)\frac{1}{2\pi}\left(\int_o^\infty e^{ik_z(g(x)\ +\ ic\ +\ z)}\ dk_z + \int_{-\infty}^{o} e^{-ik_z(g(x)+ic-z)}\ dk_z\right) \tag{2.50b}$$

The right hand side of Eqn. (2.50b) becomes,

$$\text{RHS} = i\ \frac{B(x)}{2\pi}\left(\frac{1}{(g(x)\ +\ z)\ -\ c} + \frac{1}{i(g(x)\ -\ z)\ +\ c}\right) \tag{2.50c}$$

Now taking the limit $c \to 0$ of Eqn. (2.50c) and the left hand side of Eqn. (2.50b) yields the final wave potential,[11]

$$\phi(x,z) = \frac{i}{2\pi}\ B(x)\ \left(\frac{1}{g(x)\ -\ z} + \frac{1}{g(x)\ +\ z}\right) \tag{2.51}$$

where,

$$g(x) = \int_o^x \left(\frac{K_{zz}}{K_{xx}}\right)^{\frac{1}{2}} dx.$$

It is observed that singularities form along surfaces defined by $g(x) = \pm z$, which are the resonance cones in this development.

Taking the opposite extreme for comparison we impose a boundary potential to be a standing wave composed of two sinusiodal waves traveling in opposite directions,

$$\phi(o,z) = e^{ik_{zo}z} + e^{-ik_{zo}z}.$$

For this case, $\phi(o,k_z) = \delta(k_{zo}) + \delta(-k_{zo})$ and the wave potential becomes,

$$\phi(x,z) = \frac{i}{\pi} B(x) \cos(k_{zo}z) \, e^{ig(x)k_{zo}}. \qquad (2.52)$$

A unique phase can be assigned to each point along the standing wave pattern at the plasma boundary. By writing $2 \cos k_{zo} z = \exp (ik_{zo}z) + \exp -(ik_{zo}z)$ in Eqn. (2.52), it is easy to see that surfaces of constant phase are defined by $g(x) = \pm z$. The peaks and valleys of the standing wave pattern originating at the plasma edge thus follow the same surface that was followed by the singular potential imposed at the plasma edge (Eqn.2.51).

Thus, we find that for the two extremes (i.e. a very broad k_z spectrum and a very narrow one) features at the plasma edge are transmitted along the resonance cones. Thus, the energy flow will be along the resonance cones. Also, interior fields are amplified by a factor B(x). We can expect similar behavior for more intermediate forms of the boundary k_z wave spectrum.

The axial (z direction) distance that the resonance cone travels before it reaches the lower hybrid layer can be calculated from $z_h = g(x_h)$, where x_h is the distance to the hybrid layer. For a linear density profile this can be found from an elementary integral of the form,

$$z_h = \int_o^{x_h} \left(\frac{\alpha}{1 + \beta x} \right)^{\frac{1}{2}} dx = - \frac{\pi}{z} \left(\frac{\alpha}{\beta}\right)^{\frac{1}{2}} \frac{1}{\beta} \qquad (2.53)$$

where,

$$\alpha = - \frac{4\pi e^2}{\omega^2 m_e} \frac{\partial n_e}{\partial x}, \quad \beta = - \frac{4\pi e^2}{\omega^2 m_i} \frac{\partial n_i}{\partial x}.$$

Noting that at $x = x_h$, $1 + \beta x_h = 0$, we find that $|z_h| \simeq (m_i/m_e)^{\frac{1}{2}} x_h$.[11]

For the octupole configuration, we can qualitatively describe the wave trajectory based upon the above simplified analysis. The scale length of density variation is as large as about 40 cm across the midplane of of the device and is small as 6 cm across the bridge regions. For an average scale length of about 23 cm, the wave will travel two and one half times poloidally around the machine before being absorbed near the lower hybrid layer. In addition the wave should exist only in the common flux regions of the machine when the density is high enough that $\omega < \omega_{pi}$. This is because the wave trajectories proceed from the launching structure up to the point where $\omega < \omega_{pi}$, near which total wave absorption occurs.

B.2. Three Dimensional Effects

In the treatment thus far, we have ignored the effect of the third dimension and taken $k_z = 0$. The dispersion relation, discussed in the last section, depends upon k_x, k_y and k_z, through the parameters $(k_x^2 + k_y^2)$ and k_z.[25] Because of this, for a finite imposed k_y we may obtain a new value for k_x^2 simply by subtracting k_y^2 from the old k_x value. This fact implies that the mode conversion density does not depend upon k_y, nor is the accessibility condition affected (since it depends upon k only through the parameter k_z). Thus some of the important features of the dispersion relation are unchanged by a finite k_y.

The effect of a finite k_y on the resonance cone trajectories, on the other hand, can be significant. To see this, we first find the vector trajectory of the group velocity at an arbirary point along a ray which will be found from, $\vec{v}_g \times d\vec{s} = 0$, where $\vec{v}_g = \partial\omega/\partial\vec{k}$. The slope of the trajectory is then given by,

$$\frac{\partial x}{\partial z} = \frac{v_{gx}}{v_{gz}} \quad \text{and} \quad \frac{\partial y}{\partial z} = \frac{v_{gy}}{v_{gz}} \tag{2.56}$$

Including a finite k_y in Poisson's equation, the cold plasma dispersion relation can be written,

$$D = (k_x^2 + k_y^2)\ K_{xx} + k_z^2 K_{zz} = 0. \tag{2.57}$$

Note that D is a function of ω, which, in turn, is a function of k through Eqn. (2.57). Thus it must be that,

$$\frac{\partial D}{\partial \vec{k}} = \frac{\partial D}{\partial \omega}\frac{\partial \omega}{\partial \vec{k}} . \tag{2.58}$$

Using Eqns. (2.58) and (2.56) we can then write for the group velocity trajectory,

$$\frac{\partial x}{\partial z} = \frac{\partial D}{\partial k_x}\left(\frac{\partial D}{\partial k_z}\right)^{-1} \qquad \frac{\partial y}{\partial z} = \frac{\partial D}{\partial k_y}\left(\frac{\partial D}{\partial k_z}\right)^{-1} \tag{2.59}$$

Substituting the values of the derivatives of D using Eqn. (2.57) yields,

$$\frac{\partial y}{\partial z} = \frac{k_y}{k_z}\frac{K_{xx}}{K_{zz}} \quad \text{and} \quad \frac{\partial x}{\partial z} = -\frac{K_{xx}}{K_{zz}}\left(-\frac{K_{zz}}{K_{xx}} - \frac{k_y}{k_z}\right)^{\frac{1}{2}} \qquad (2.60)$$

From this result we see that a finite k_y allows the wave group velocity to have a component in the $\hat{y}$ direction since $\partial y/\partial z$ is finite. This was not the case in the previous analysis. Also the group velocity ray will move into the density profile ($\hat{x}$ direction) more slowly as a function of z than the previous analysis showed because $\partial x/\partial z$ decreases with increasing k_y.

Applying this result to the octupole, we find that the wave energy velocity will now have an additional component in the toroidal direction because of an unavoidable k_y wave spectrum resulting from an antenna structure having a finite length in the $\hat{y}$ direction. The wave energy will follow a roughly helical path for a pure poloidal octupole magnetic field. The pitch angle of this helical path will vary with individual k_y components of the wave. We thus can expect to find the wave distributed over a large sector of the torus rather than only in the single azumuthal plane of the machine where the antenna is located. In addition, the fields should still be found primarily in the common flux regions of the device between the walls and the separatrix because of the nature of the wave energy trajectories.

B.3. Hot Plasma Model

Up to this point we have used cold plasma theory to describe the wave fields. This will give a fair picture over only a portion of the wave trajectories. Near and beyond the warm plasma wave turning point another description must be used, as already mentioned.

The differential equation describing the wave fields in this case, may be found by inverse Fourier transforming(in the k_x sense) the general electrostatic dispersion relation $\vec{k} \cdot \overline{K} \cdot \vec{k}\hat{\phi} = 0$. We write this explicitly here as,

$$ik_x(K_{xx})ik_x\hat{\phi} + k_x(K_{xz})ik_z\hat{\phi} + ik_z(K_{xz})ik_x\hat{\phi} + ik_z(K_{zz})ik_z\hat{\phi} = 0 \ . \tag{2.61}$$

For the purpose of inverse Fourier transforming, the order in which the multiplications appear in Eqn. (2.61) will be important.

The dielectric tensor elements can be expanded in powers of k_x^2 as,

$$K_{xx} = \sum_{n=0}^{\infty} \alpha_n k_x^{2n}, \qquad K_{xz} = \sum_{n=0}^{\infty} \beta_n k_x^{2n+1},$$
$$K_{zz} = \sum_{n=0}^{\infty} \alpha_n k_x^{2n} \tag{2.62}$$

where the coefficients are given by,

$$\alpha_n = \frac{\partial^n K_{xx}}{\partial(k_x)^n}\bigg|_{k_x^2 = 0}, \quad \beta_n = \frac{\partial^n}{\partial(k_x^2)^n}\left(\frac{K_{xz}}{k_x}\right)\bigg|_{k_x^2 = 0}$$
$$\gamma_n = \frac{\partial^n K_{zz}}{\partial(k_x^2)^n}\bigg|_{k_x^2 = 0}$$

Taking the inverse Fourier transform of these elements gives,

$$\begin{aligned} \mathcal{F}^{-1}(K_{xx}) &= \sum_{n=0}^{\infty} \alpha_n \frac{\partial^{2n}}{\partial x^{2n}} \delta(x) \\ \mathcal{F}^{-1}(K_{xz}) &= \sum_{n=0}^{\infty} \beta_n \frac{\partial^{2n+1}}{\partial x^{2n+1}} \delta(x) \\ \mathcal{F}^{-1}(K_{zz}) &= \sum_{n=0}^{\infty} \gamma_n \frac{\partial^{2n}}{\partial x^{2n}} \delta(x) \end{aligned} \tag{2.63}$$

where $\delta(x)$ is the delta function.

Now using the property of Fourier transforms,

$$\mathcal{F}^{-1}(\mathcal{F}(g)\ \mathcal{F}(h)) = g * h, \tag{2.64}$$

where the asterisk denotes the convolution integral is to be taken, the inverse transform of Eqn. (2.61) can be obtained. The result is,

$$\begin{aligned} &\frac{\partial}{\partial_x}\left(\sum_{n=0}^{\infty} \alpha_n \frac{\partial^{2n}}{\partial x^{2n}}\right)\frac{\partial \phi}{\partial x} + ik_z\left(\sum_{n=0}^{\infty} \beta_n \frac{\partial^{2n+1}}{\partial x^{2(n+1)}}\right)\frac{\partial \phi}{\partial x} \\ &+ ik_z \frac{\partial}{\partial x}\left(\sum_{n=0}^{\infty} \beta_n \frac{\partial^{2n+1}}{\partial x^{2n+1}}\right)\phi - k_z^2\left(\sum_{n=0}^{\infty} \gamma_n \frac{\partial^{2n}}{\partial x^{2n}}\right)\phi = 0 \end{aligned} \tag{2.65}$$

where it should be remembered that α_n, β_n, γ_n, are functions of x and k_z in general.

Eqn. (2.65) represents the general equation describing the wave fields in cartesian coordinates. We see that the cold plasma equation, Eqn. (2.39), results from the n=0 term in Eqn. (2.65) (β_o=0 for $T_{i,e}$=0). The next higher order equation will be a fourth order differential equation derived from the n=0,1 terms in Eqn. (2.65),

$$\frac{\partial}{\partial x}\left(\alpha_o + \alpha_1 \frac{\partial^2}{\partial x^2}\right)\frac{\partial\phi}{\partial x} + ik_z\left(\beta_o \frac{\partial}{\partial x} + \beta_1 \frac{\partial^3}{\partial x^3}\right)\frac{\partial\phi}{\partial x}$$

$$= ik_z \frac{\partial}{\partial x}\left(\beta_o \frac{\partial}{\partial x} + \beta_1 \frac{\partial^3}{\partial x^3}\right)\phi - k_z^2\left(\gamma_o + \gamma_1 \frac{\partial^2}{\partial x^2}\right)\phi = 0 \ . \qquad (2.66)$$

Recognize that $\alpha_o = K^o_{xx}$, $\alpha_1 = K'_{xx}$, $\beta_o = (1/k_x)\, K^o_{xz}$, $\beta_1 = (1/k_x)\, K'_{xz}$, $\gamma_o = K^o_{zz}$, and $\gamma_1 = K'_{zz}$ as defined in Eqn. (2.27). For $k_z v_i/\omega << 1$ and $k_z v_e/\omega_{ce} << 1$ it can be shown that $\alpha_1 >> k_z\beta_1$ and $\alpha_o >> (k_z\beta_o - k_z^2\gamma_1)$. This essentially means that the K_{xz} term and the first term in the expansion for K_{zz} can be neglected in the equation for wave potential. After regrouping terms, Eqn. (2.66) can be approximated as[33],

$$\frac{\partial^4\phi}{\partial x^4} + \frac{1}{\alpha_1}\frac{\partial\alpha_1}{\partial x}\frac{\partial^3\phi}{\partial x^3} + \frac{\alpha_o}{\alpha_1}\frac{\partial^2\phi}{\partial x^2} + \frac{1}{\alpha_1}\frac{\partial\alpha_o}{\partial x}\frac{\partial\phi}{\partial x} - k_z^2\frac{\gamma_o}{\gamma_1}\phi = 0 \qquad (2.67)$$

An analytic procedure for solving Eqn. (2.67) is given in reference 33. Based upon this equation Colestock[34] shows, for a point source at the plasma boundary, that wave energy flows from the plasma edge along the cold plasma resonance cone channel found from Eqn. (2.51). Near the warm plasma turning point the energy flow turns around and propagates back out of the plasma, as expected from the dispersion relation.

C. Collisional Effects

All of the analysis to this point has ignored the effects of collisions. Plasma collisions can randomize the otherwise ordered and coherent charged particle motion that results from the electromagnetic and electrostatic wave fields. This randomization is an irreversible process and can lead to appreciable wave energy absorption before the wave is able to mode convert.

The maximum plasma collisionality that will still allow mode conversion can be estimated from the constraint,

$$\int_o^{x_m} k_{xi}(x)\, dx < 1, \tag{2.69}$$

where k_{xi} is the spatial damping rate resulting from collisions and the integral is evalutated between the plasma edge and the mode conversion region $(x=x_m)$.

The following expression for k_i can be easily derived from fluid equations[10],

$$\frac{k_{xi}}{k_{xr}} = \frac{k^2}{k_z^2}\,\frac{1}{2K_{zz}}\,\frac{\omega_{pi}^2}{\omega^2}\left(\frac{\nu_i}{\omega} + \frac{\nu_e}{\omega}\left(\frac{\omega^2}{\omega_h^2} + \frac{m_i}{m_e}\frac{k_z^2}{k^2}\right)\right) \tag{2.70}$$

where $k^2 = k_x{}^2 + k_z{}^2$ and $\omega_h{}^2 = \omega_{ce}\omega_{ci}$, as before. The quantity k_{xr} can be approximated from the cold plasma dispersion relation (we are examining wave behavior only up to the turning point so cold plasma theory is a fair approximation),

$$k_{xr} \simeq (-\frac{K_{zz}}{K_{xx}})^{\frac{1}{2}}\,|k|_z \quad . \tag{2.71}$$

Substituting cold plasma values for the dielectric tensor elements given by Eqn. (2.3b) we obtain for condition (2.69),

$$\kappa \left[\lambda_1 \int_0^{\psi_o} \left(\frac{\psi}{(1-\psi)} \right)^{\frac{3}{2}} d\psi + \lambda_2 \int_0^{\psi_o} \frac{\psi^{\frac{1}{2}}}{(1-\psi)^{\frac{3}{2}}} d\psi \right] < 1 \qquad (2.72)$$

where,

$$\kappa = - \frac{\pi}{\psi_o} \left(\frac{\ell}{\gamma_z}\right) \left(\frac{m_i}{m_e}\right)^{\frac{1}{2}}$$

$$\lambda_1 = \left(\frac{\nu_i}{\omega} - \frac{\nu_e}{\omega}\right)$$

$$\lambda_2 = \left(\frac{e}{\omega}\right), \quad \ell^{-1} = \frac{1}{n} \frac{dn}{dx} \Big|_{x=x_m}$$

$$\psi_o = \frac{\omega_{pi}^2}{\omega^2} \Big|_{x=x_m} = \left(1 + 2\sqrt{3} \frac{k_z v_e}{\omega} \left(\frac{T_i}{T_e}\right)^{\frac{1}{2}} \right)^{-1}$$

In Eqn. (2.72), we have assumed for simplicity that $\omega/\omega_h < 1$. This is a fair assumption for typical magnetic field values near the turning point in the experiment. We have also assumed a linear density variation.

Evaluating the integrals in Eqn. (2.72) yields the final expression for the maximum collisionality that will permit mode conversion,

$$\kappa \left[\frac{\nu_i}{\omega} \left(\left(\frac{\psi_o}{1-\psi_o}\right)^{\frac{1}{2}} (3-\psi_o) + 3 \tan^{-1} \left(\frac{1-\psi_o}{\psi_o}\right)^{\frac{1}{2}} - \frac{3\pi}{2} \right) - \frac{\nu_e}{\omega} \left(\psi_o^{\frac{1}{2}} (1-\psi_o)^{\frac{1}{2}} + 5 \tan^{-1} \left(\frac{1-\psi_o}{\psi_o}\right)^{\frac{1}{2}} - \frac{5\pi}{2} \right) \right] < 1 . \qquad (2.73)$$

For sample experimental parameters, $T_i = T_e = 15\text{eV}, n=5\text{x}10^{11}\text{cm}^{-3}$, $\nu_e/\omega = 3.7 \text{ x } 10^{-4}$, $\nu_i/\omega = 6.2 \text{ x } 10^{-6}$, and $\ell/\lambda_z \simeq 0.3$, the left-hand side of Eqn. (2.73) is about 0.1. The inequality for this case is well satisfied, and over eighty percent of the wave power will propagate to the turning point.

The choice of experimental parameters used above is close to the actual experimental values after RF heating and so it will be meaningful to compare the experiment with the collisionless model at least up to the wave turning point.

A more exact treatment that is valid closer to the turning point than the above analysis reveals that exactly at the turning point there is no special enhancement of wave damping due to collisional absorption.[35,36] In this case the constraint that allows us to neglect collisions is given by,

$$\kappa \frac{\nu}{\omega} \frac{\omega^2}{\omega_h^2} \left(\frac{8\psi_o}{1-\psi_o}\right) < 1 \tag{2,74}$$

This is adapted from Eqn. (9) of reference 36 where the notation of Eqn. (2.72) is used for comparison. The form of Eqn. (2.74) is much like the more approximate case, Eqn. (2.73).

For the same sample plasma parameters that were substituted into Eqn. (2.73) we find that the left hand side of Eqn. (2.74) is about 0.08. Thus, the more exact result, Eqn. (2.74), is slightly less restrictive than Eqn. (2.73). We conclude, then, that for typical experimental parameters, wave behavior follows a collisionless theory up to and including the turning point. Thus mode conversion should be present in the following experiment.

CHAPTER 3

EXPERIMENTAL APPARATUS

A. The Toroidal Octupole

The toroidal octupole has been described in detail in the literature.[37-39] Only a brief description of parameters pertinent to the lower hybrid heating experiment will be provided here.

Figure 6 shows a diagram of the octupole. A purely poloidal magnetic field is produced by currents in the four internal hoops together with image currents in the aluminum walls. A flux plot is shown in Fig. 7. A 48,000 μF capacitor bank charged to 2.5 kV excites a maximum poloidal field strength in the experiment of about 2.0 kG near the surface of the outer hoops, 4.5 kG near the surface of the inner hoops and zero where the separatrix field lines cross. A small toroidal field of about 200 G is applied near the center of the machine by imposing a voltage on the toroidal gap. This field eliminates the electron cyclotron resonance that would otherwise occur at about B=50 G for an applied frequency of 140 MHz. Finally, the magnetic field is crowbarred at peak field values and resistively decays in from ~90 ms to ~160 ms .

The machine has a major radius of 1.4 m and a minor cross section 1.2 m x 1.2 m with a total vacuum volume of 8.6 m^3 . Both hydrogen and helium plasmas are produced by gun injection with $T_i \simeq T_e = 40$eV and $n = 2 - 0.5 \times 10^{12} cm^{-3}$ early in time. Temperature decay times are typically 1-4 ms initially due to dominant charge exchange losses

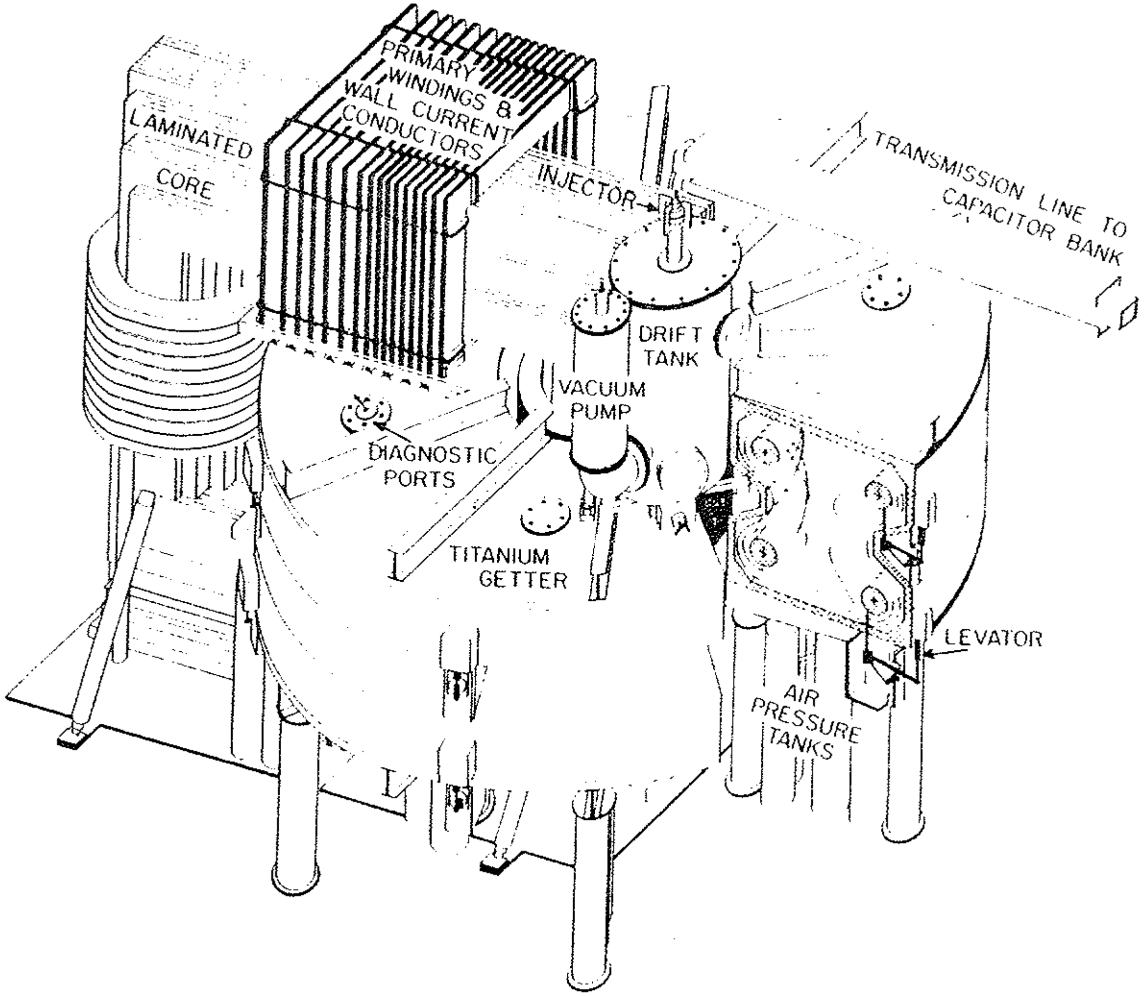
PRIMARY WINDINGS & WALL CURRENT CONDUCTORS
LAMINATED CORE
INJECTOR
TRANSMISSION LINE TO CAPACITOR BANK
DRIFT TANK
VACUUM PUMP
DIAGNOSTIC PORTS
TITANIUM GETTER
LEVATOR
AIR PRESSURE TANKS

Figure 6 WISCONSIN LEVITATED OCTUPOLE

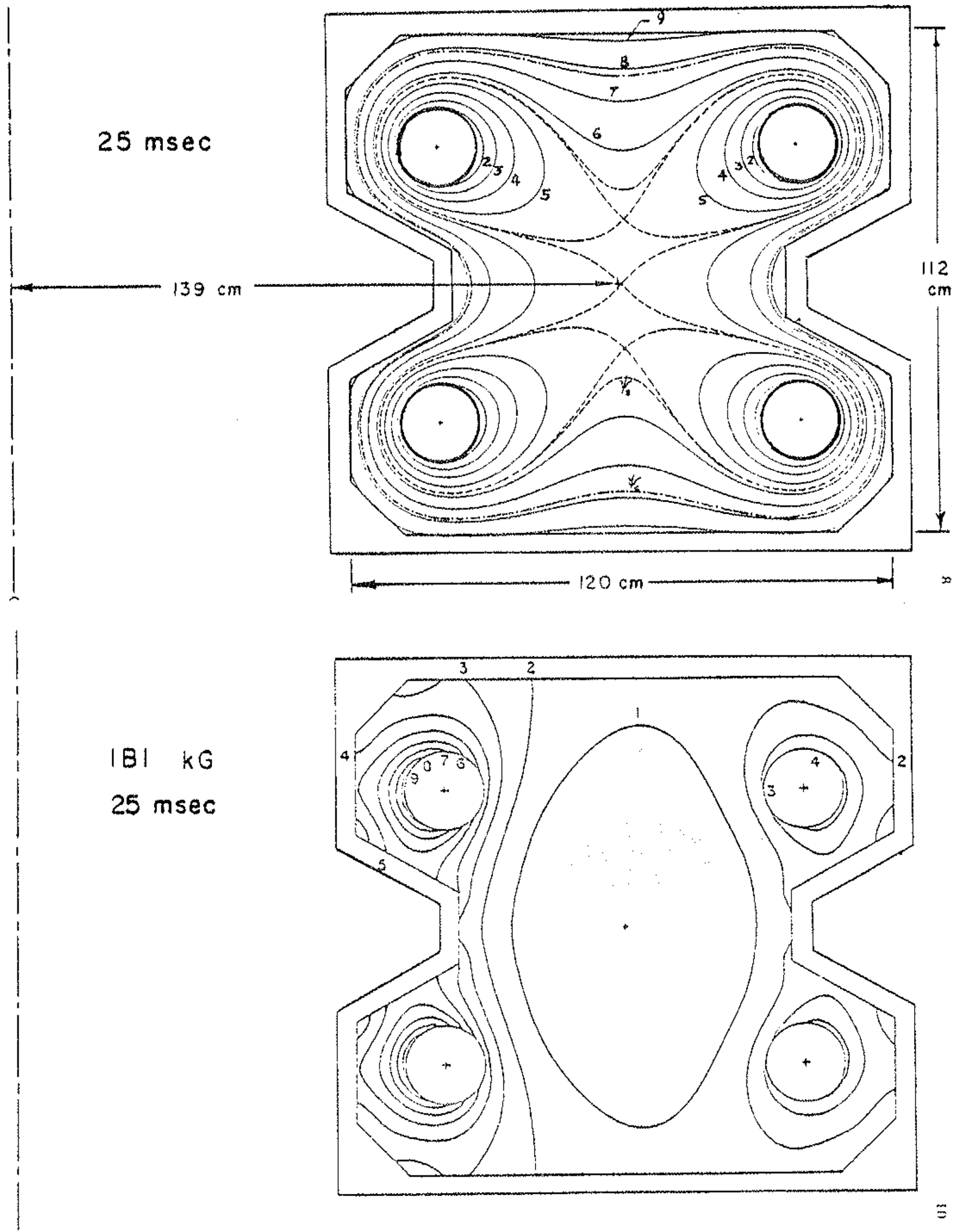
25 msec
9
8
7
6
2
3
4
5
139 cm
112 cm
ψs
120 cm
|B| kG
25 msec
1
2
3
4
5
6
7
8
9
℄

Figure 7. Octupòle flux plot for maximum field excitation.

and ion neutral elastic collisions. Density decay times are between 10-20 ms initially.

B. Radio Frequency Sources

Radio frequency power up to 40 kW at 140 MHz is produced by class C, push-pull oscillators. Forward and reverse power is monitored using a directional coupler and diode detector circuitry.

Schematics of the oscillators are shown in Figs. 8 and 9. The 140 MHz oscillator uses two 3CX1500A7 triodes. An operating frequency of 140 MHz is a practical upper limit of efficient operation of the oscillator in its present design. The limit occurs because the required tank capacitance and inductance eventually fall below stray tube and circuit values.

Care has to be taken to keep the inductance between the cathode connections of the two tubes to a minimum. Any small inductance there acts as an RF choke and also alters the phase of the feedback signal unfavorably. This reduces the amplitude of oscillation. Optimum phase of the feedback signal can also be destroyed if the path between the plate of one tube and the grid of the adjacent tube is too long. A small fraction of a wavelength (several centimeters) is all that is necessary to destroy oscillation in this case. The physical construction of the oscillator reflects all of the above considerations.

The design of the second oscillator, which operates at 100 MHz, eliminates many of the difficulties of the first oscillator and should be capable of operation at higher frequencies with some modifications.

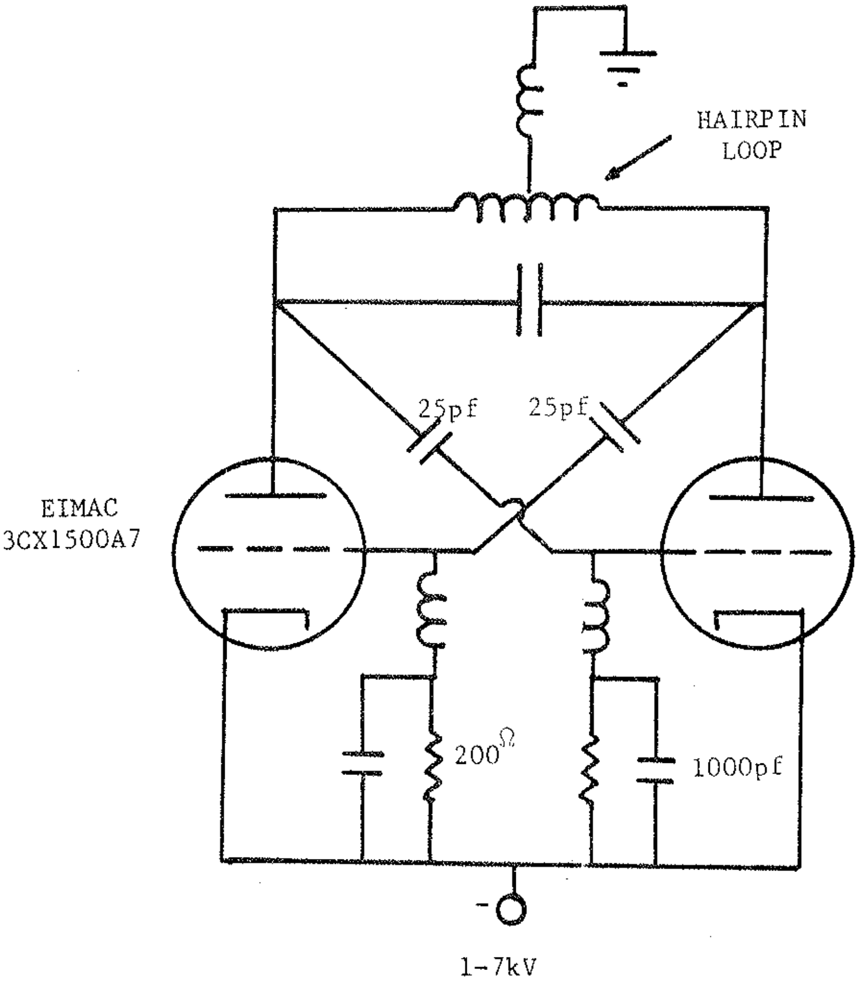
HAIRPIN LOOP
EIMAC 3CX1500A7
25pf
25pf
200Ω
1000pf
-
1-7kV

Figure 8. 140MHz oscillator.

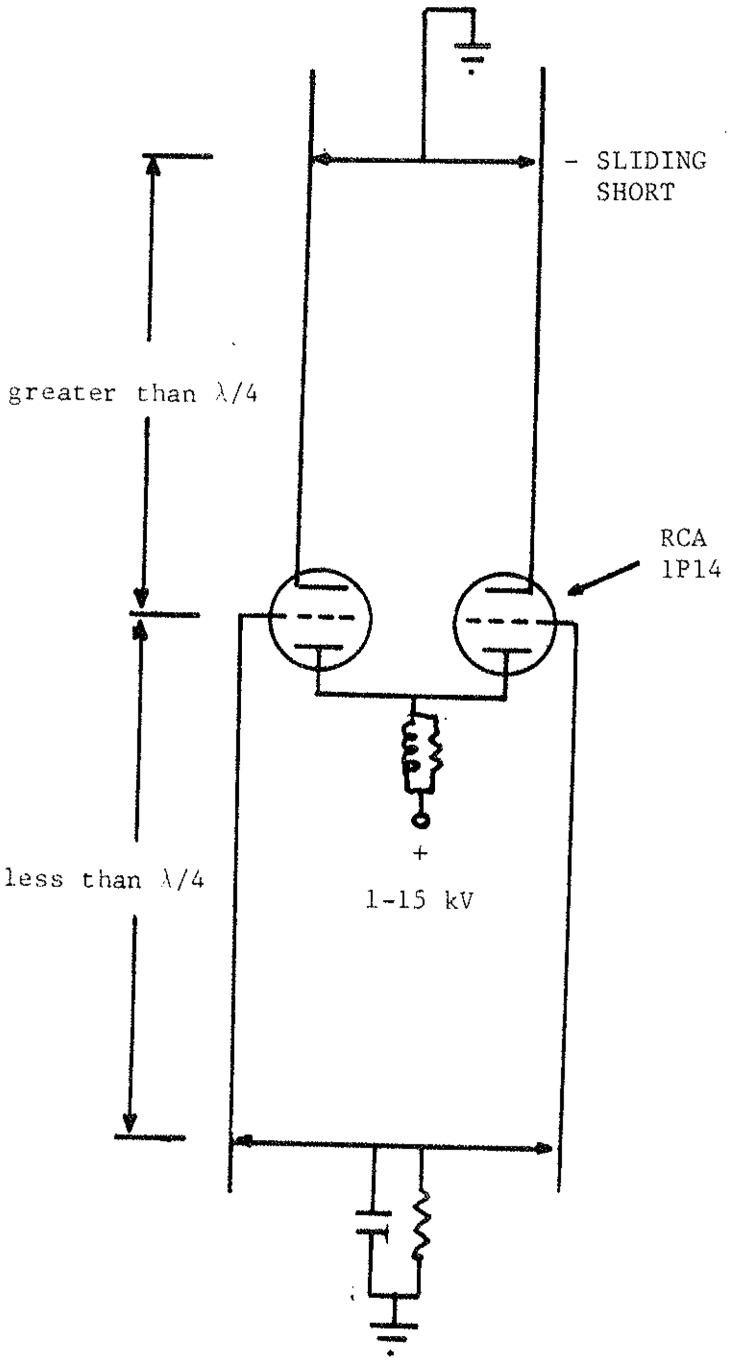
SLIDING
SHORT
greater than λ/4
RCA
1P14
less than λ/4
+
1-15 kV

Figure 9. 100MHz oscillator.

It uses a pair of 1P14 triodes operated push-pull, and functions much like a Colpitts oscillator. Circuit elements with adjustable impedance values are formed in this case from transmission lines with moveable shorting bars. A complete description of design considerations and construction of this oscillator is provided in Ref. 40.

Output coupling of both oscillators is matched to a fifty Ohm load by varying the size and position of the coupling loop. A matching circuit at the antenna,should one be required, consists of a line stretcher in series with the transmition line and an adjustable shorted stub in parallel with the line. The line stretcher transforms the real part of the antenna impedance to 50 Ohms while the shorted stub cancels the transformed antenna reactance at the end of the line stretcher.

C. Wave Coupling

The wave launching structure employed in this experiment is a T shaped rod antenna shown in Fig. 10. The antenna is insertable and rotateable at the edge of the plasma. In free space it is essentially a top loaded dipole.[41] A detailed analysis of this type of antenna in the presence of plasma is provided in reference 42.

The length of the antenna ($L = \lambda/4$) and its symmetry about the feed point are designed to produce a k_z wave power spectrum that satisfies the accessibility condition in the presence of plasma (see discussion after Eqn. (2.6)). In free space and with the antenna arms oriented along the magnetic field the value of $n_z = k_z c/\omega$ peaks at about $n_z = 4$. In the presence of plasma, some damping of wave energy along the arms

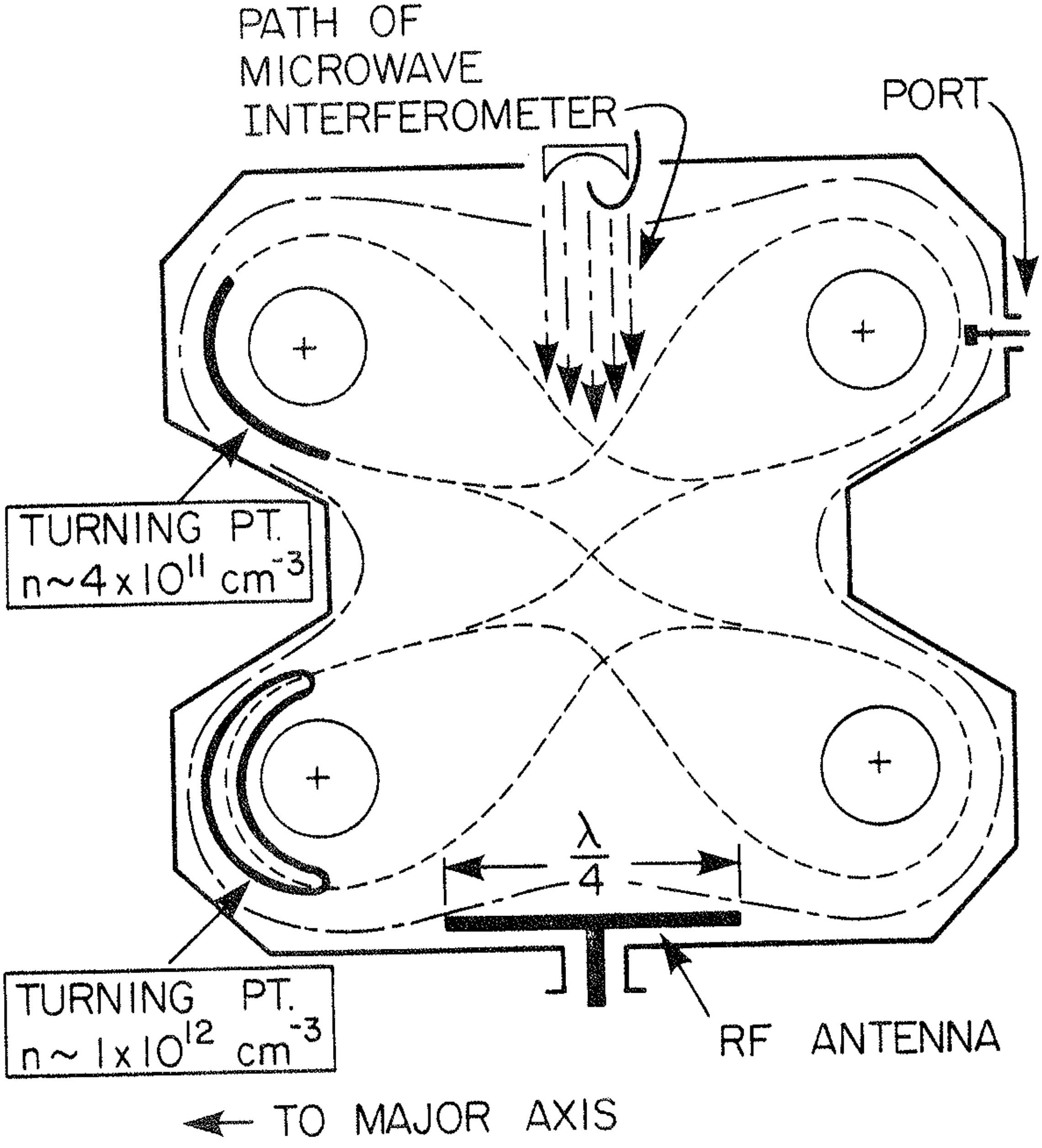
PATH OF MICROWAVE INTERFEROMETER
PORT
TURNING PT. $n \sim 4 \times 10^{11}$ cm^{-3}
TURNING PT. $n \sim 1 \times 10^{12}$ cm^{-3}
$\frac{\lambda}{4}$
RF ANTENNA
TO MAJOR AXIS

Figure 10. Lower hybrid RF antenna shown in relation to diagnostics and lower hybrid turning points for $n=4 \times 10^{11} \mathrm{cm}^{-3}$ and $n=1 \times 10^{12} \mathrm{cm}^{-3}$ with $k_z v_e/\omega=0.16$.

of the antenna is expected as wave energy is coupled to the plasma. This causes the current distribution to peak more toward the feed point. The effect produces a slight upshift and broadening of the peak in the n_z wave power spectrum. In addition, a slight upshift in n_z occurs in the presence of plasma because of an increase in the effective dielectric constant of the antenna environment. As shown in reference 42, both of these effects are small for low plasma densities near the antenna.

Besides the n_z spectral requirements, the wave electric field needs to have a component along the magnetic field in order to couple energy effectively to the plasma core. This fact is easily deduced from Eqn. (2.2). A real part to the loading impedance into the antenna terminals results primarily because of contributions to this field polarization by antenna currents.[42] Other polarizations contribute primarily reactive impedance values, and coupling to them is poor.

In actual practice, with proper antenna placement, along the edge of the plasma density profile, over 95% of the incident power is coupled to the torus without the need for a matching network at the antenna. A plot of this coupling efficiency versus radial position for several peak densities is shown in Fig. 11. The antenna arms are oriented along $\vec{B}$. It is observed from these figures that to achieve this excellent coupling we must have, $n > 3 \times 10^{11}$ cm^{-3}. As will be shown later, this is the density at which lower hybrid resonance appears in the machine and ion heating begins.

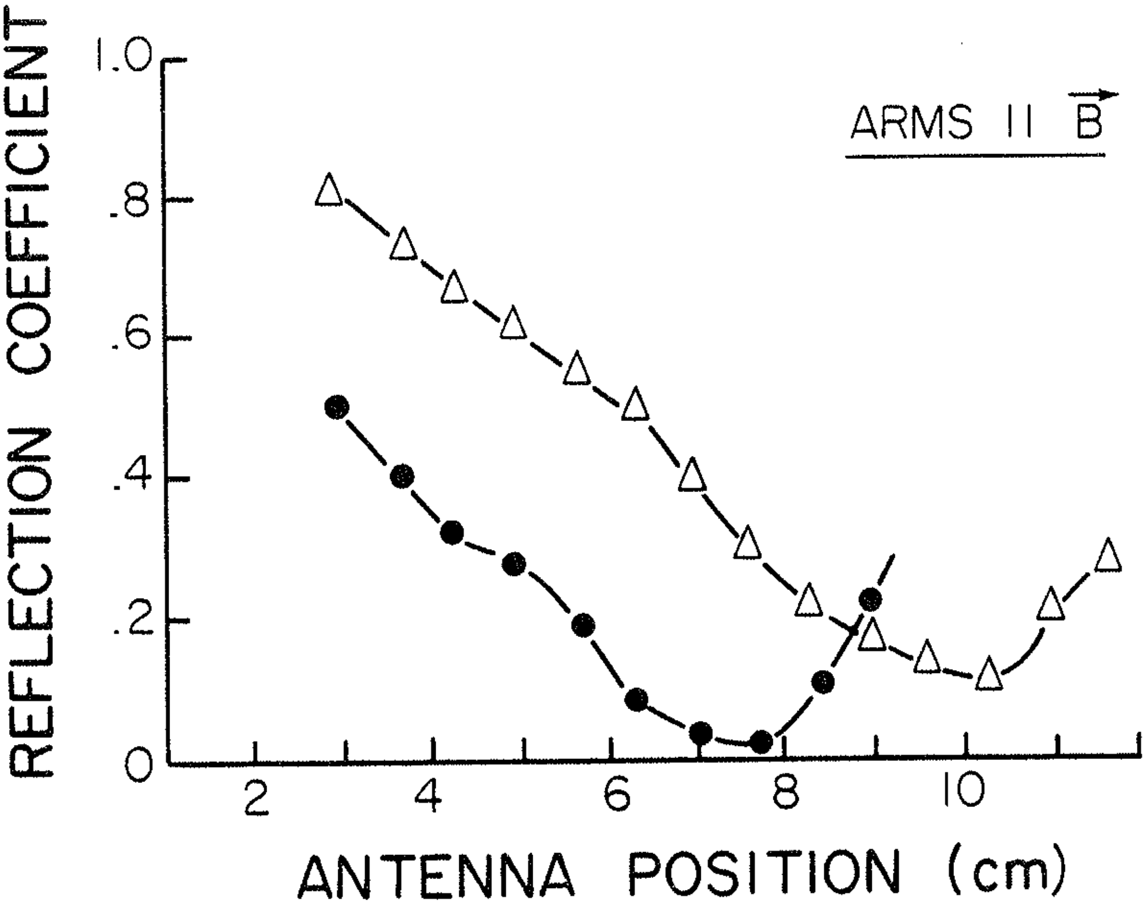

Figure 11. Reflection coefficient for the lower hybrid antenna versus inserted distance from the lower wall. Antenna arms are parallel to the magnetic field.

Δ - $n = 2 \times 10^{11} cm^{-3}$

● - $n = 4 \times 10^{11} cm^{-3}$

This together with antenna coupling behavior with position along the density gradient are about the only characteristics of wave coupling that are in agreement with theory.[43] Disagreements become apparent when the antenna arms are oriented perpendicular to the magnetic field. Coupling efficiency versus position for this case is shown in Fig. 12. Surprisingly the behavior is almost identical to that in Fig. 11. The fast wave should have been excited in this case. But coupling to the fast wave is more difficult because of a thicker evanescent layer near the plasma edge.[22] Also, coupling to the fast wave should not be sensitive to the presence of the slow mode resonance yet coupling is most efficient when this resonance is present in the machine just as it was when the arms were parallel to the magnetic field.

In addition, the fast wave should do no ion heating according to simple theory.[22] However, a measure of the ion energy distribution using a gridded perpendicular energy analyzer (to be described later) shows that ion heating is as great with the antenna perpendicular to the magnetic field. We must conclude that the slow mode is excited independent of the antenna's rotational orientation.

The reason for this apparent rotational symmetry is not known. It suggests, however, at least two possibilities. First of all, wave energy may be coupled to the plasma most strongly from wave fields near the antenna feed point, since this point has the rotational symmetry required to explain the results. A second possibility is that strong density fluctuations ($\Delta n/n \simeq 1$) near the plasma

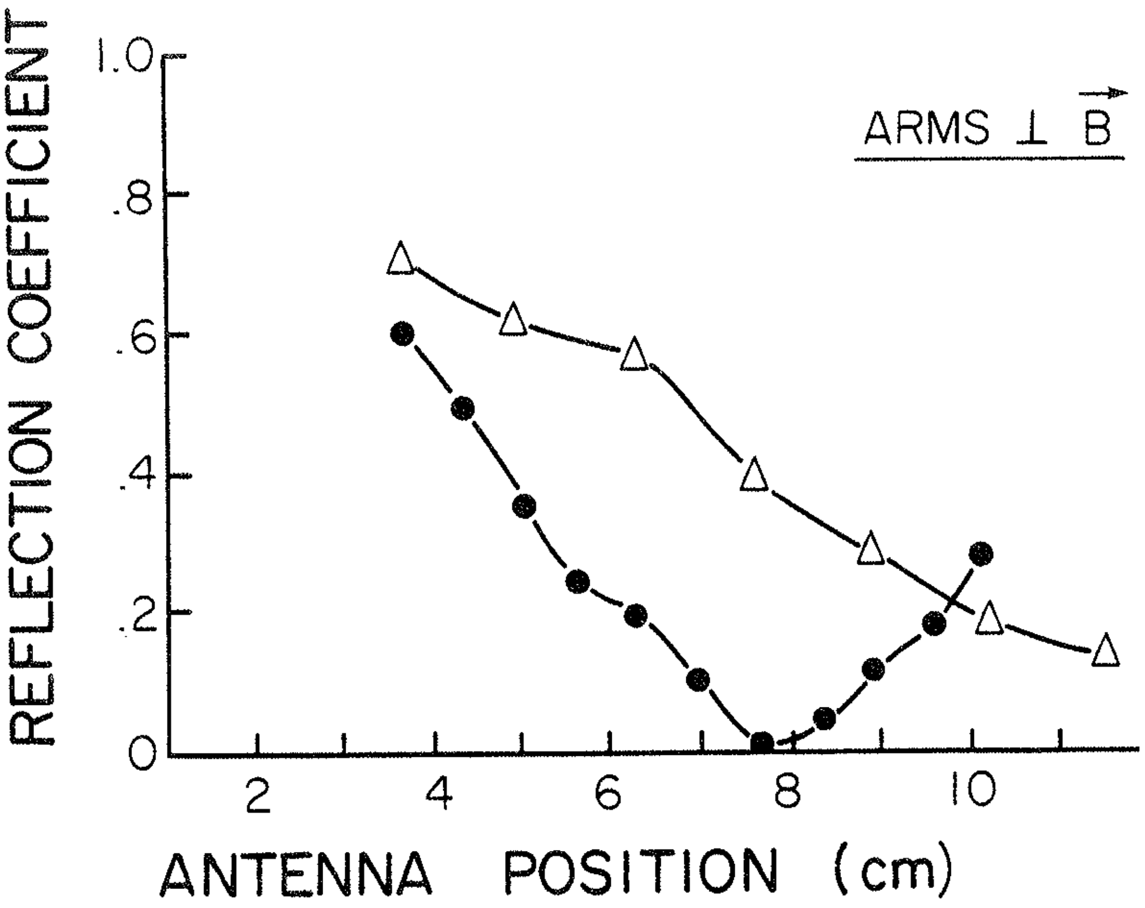

Figure 12. Reflection coefficient for the lower hybrid antenna versus inserted distance from the lower wall. Antenna arms are perpendicular to the magnetic field.

△ - $n = 2 \times 10^{11} cm^{-3}$

● - $n = 3 \times 10^{11} cm^{-3}$

edge randomly scatter the wave fields. Information in wave fields produced at the surface of the antenna could be smeared out in several scattering lengths making one antenna orientation indistinguishable from another as far as interior field polarization and wave dispersion are concerned.

Since the fluctuations can occur independent of the presence of RF waves the effect should be present no matter how small the RF power level may be. In fact, wave coupling in this experiment is observed to be independent of the antenna's rotational orientation down to power levels of only a few hundred milliwatts. Further investigation of the wave scattering idea is warranted.

The feedpoint coupling theory, by itself, does not adequately explain certain experimental results. For example, energy coupled from the feed point would look effectively like a point source. As such, it would create a very broad n_z spectrum. However, results to be described in chapter 5 indicate that the spectrum must be peaked. Other results indicate that n_z values originating at the plasma edge must be only slightly above the accessible n_z value.

An experiment was performed to see if strong wave attenuation along the arms of the antenna was occuring, which is one possible mechanism restricting fields to the feedpoint. An effectively shorter antenna was constructed for this purpose by replacing the original antenna arms with a small metal disk 2 cm in diameter. If wave power were strongly damped along the antenna arms, this antenna should have properties similar to the original antenna. However, the coupling efficiency of this second antenna was extremely poor. This indicates that there are, in fact, substantial currents flowing along the arms of the antenna and no significant attenuation occurs along them.

If, then, radiation into the plasma occurs only from fields near the feed point, the antenna arms must provide only reactive antenna loading, as is the case for a free space antenna. But this is a contradiction of the basic theory which says that if currents do exist on the antenna arms, wave fields are produced from these currents that should couple very efficiently to the plasma interior.[42] The theory is, admittedly, a linear one, but then we have established that the phenomenon occurs for minute power levels of a few hundred milliwatts where linear theory should apply. Based upon this sort of argument it is difficult to see how the feedpoint coupling idea could be responsible for the observed behavior.

Some theory has been developed on the scattering of lower hybrid waves near the edge of the plasma[7,8], the second possibility mentioned. Unfortunately,no adequate comparison is possible in this report based upon available data. These results suggest, however, that fluctuations could play a role and, therefore, are an improtant topic for future research.

CHAPTER 4

DIAGNOSTICS

Some of the principle diagnostic instruments for obtaining plasma density, and electron and ion temperatures will be discussed in this section. These include a microwave interferometer, an optical Fabry-perot interferometer, parallel and perpendicular gridded energy analyzers, and Langmuir probes.

The Fabry-Perot interferometer and the perpendicular energy analyzer will be described in greater detail partly because of the author's more extensive involvement in development of these particular diagnostics. In addition, the detail is needed to make clear the various limitations of each instrument, and facilitate proper interpretation of key results in the next chapter.

A. Microwave Fringe-Shift Interferometer

This instrument measures, basically, the average value of density across the path of a coherent microwave beam. The analysis is straight forward and leads to the result[44],

$$<n> = n_p \left(\ell_o \int_o^{\ell_o} \tilde{n}\, dx\right)^{-1} = (1.2 \times 10^2)\left(\frac{\Delta\phi}{\ell_o}\right) f \qquad (3.1)$$

where n_p is the peak value of density, $\tilde{n} = n(x)/n_p$, $\Delta\phi$ is the relative phase shift in radians measured by the interferometer, ℓ_o is the length of the path of the microwave beam through the plasma, and f is the frequency of the microwaves.

In the present experiment the beam path is across the machine mid-cylinder, where ℓ_o = 100 cm. Also f = 35 GHz so that,

$$\langle n \rangle = ((4.2 \times 10^{10})\ \Delta\phi)\ \mathrm{cm}^{-3} \qquad (3.2)$$

Frequently, we will be interested in the peak value of density, which requires a knowledge of the density profile. This can be determined from Langmuir probes. For more approximate measurements a lower bound on this peak density can be determined by assuming a uniform density profile. Thus, the average value indicated in Eqn. (3.2) also gives a lower bound on peak density. The more sharply peaked the profile, the higher will be the peak density indicated by a given number of fringe shifts. For a triangular density profile, which is an approximation to the experimental profiles,

$$n_p = ((8 \times 10^{10})\ \Delta\phi)\ \mathrm{cm}^{-3}. \qquad (3.3)$$

From a knowledge of typical variations in the density profiles for a variety of conditions, it is safe to say that Eqn. (3.3) will probably be within a factor of two of the actual peak value for most conditions.

Small reproduceable fluctuations, frequently superimposed on the interferometer fringe pattern are believed to be due to diffraction effects.[44] This is entirely possible since the size of the microwave transmitting and receiving structures (parabolic reflectors in this case) are only a little more than 10 times the free space operating wavelength, and since perfect plane waves are undoubtedly not produced, particularly because of slight focussing in the presence of plasma. The antennas thus look essentially like microwave "pinholes", with the focus of the parabolic receiver picking up zones of constructively and destructively interfering wave components as the amount of beam focussing changes. The phenomenon is related to ordinary Fresnel diffraction. However, since the effect is slight and does not seriously interfere with interpretation of results, it will not be considered further.

B. Optical Fabry-Perot Interferometer

The Fabry-Perot interferometer is a widely used instrument in high resolution spectroscopy. A schematic of the instrument used in the present experiment is shown in Fig. 13. It will be used in this case to measure the Doppler broadening of the line profile of the helium II 4686 Å n = 4 → 3 transition, although it can be adapted to measure other lines in the visible spectrum. Ion temperature will be deduced from the full-width at half-maximum (FWHM) of the profiles as described below. Detailed principles of operation of the instrument are provided in the appendices.

B.1. General Considerations

The Fabry-Perot was chosen over prism and grating monochromators primarily because of its greater luminosity at a given resolving power (see appendix B). In addition, because of its higher resolution, it is capable of measuring low temperature plasmas ($>$ leV) that may be expected late in time after gun injection in the octupole. Finally, the very narrow line profiles of high Z impurites, such as carbon and oxygen can be measured with the instrument if desired.

There are a number of difficulties associated with spectroscopic measurements of this sort. First of all, since a hydrogen ion has no line radiation, we are restricted to measuring line profiles for neutral hydrogen and ions of heavier atoms (bound electrons must be retained). However, measurements of light from small amounts of impurity doping ($\gtrsim$10%) in hydrogen can many times be used to estimate the majority species temperature.

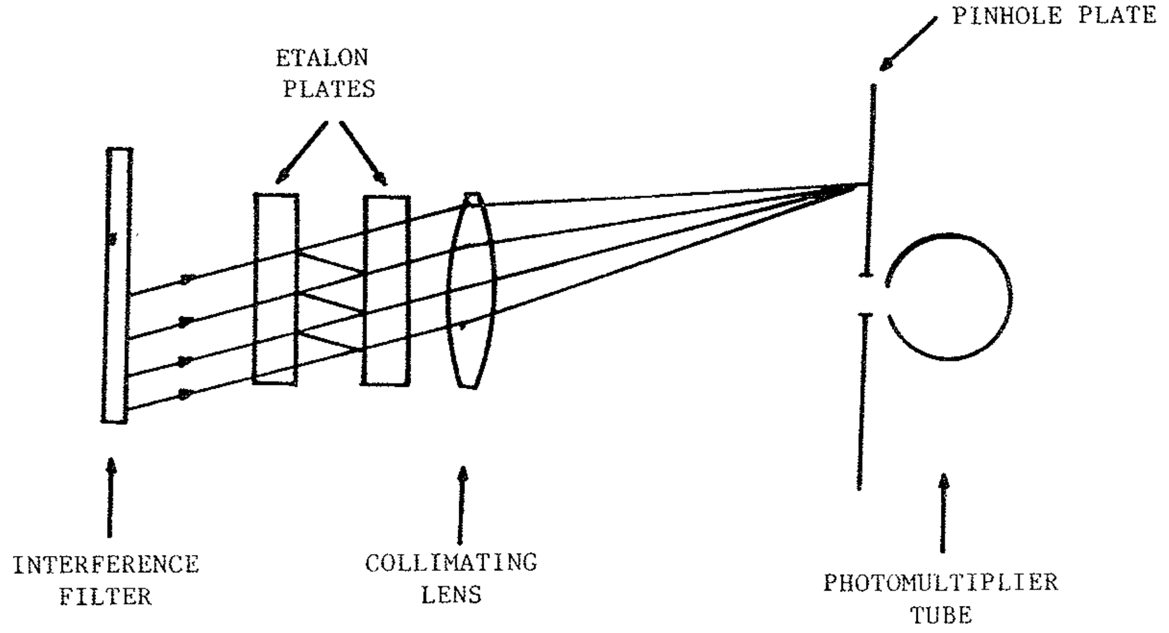
PINHOLE PLATE
ETALON
PLATES
INTERFERENCE
FILTER
COLLIMATING
LENS
PHOTOMULTIPLIER
TUBE

Figure 13. Optical Fabry-Perot interferometer.

A further limitaion is that a given line will not have measureable intensity above electron temperatures producing complete burnout of the ionized state. A lower bound of measureable intensity is set by excitation and deexcitation conditions of the state but these are generally not very restrictive. Measurements with He II 4686 Å have been taken in various experiments over the range $100\text{eV} < T_i < 0.06\text{eV}$.[45,65]

Difficulties occur in intermediate temperature ranges because of fine structure splitting of the 4686 Å line. This appears as a series of thirteen separate components of varying intensity spread over a spectral width of about 0.5 Å.[45,65] Measurements of the fine structure profile widths can be used to obtain ion temperatures, but this requires that broadening be less than or on the order of 0.04 Å to assure that the lines are resolvable. For greater line broadening, the fine structure becomes smeared together. Interpretation of true broadening then requires a knowledge of the oscillator strengths of individual components, which cannot be accurately determined in the present experiment. If, however, one component of the fine structure is dominant, the overall line profile will be an accurate representation of true broadening. Without knowing if this is the case, we can assign an upper bound to the line width, and thus the ion temperature, by assuming that this is the case. A lower bound can be estimated by subtracting the spectral width of the overall fine structure from the measured overall spectrum.

Finally, it should be mentioned that most of the theory for line radiation is based upon equilibrium situations. This is sometimes a questionable assumption for transient plasmas. Since it takes collisions to produce equilibrium, we can expect the theories to be more accurate as temperature decreases and density increases (recall that collisional relaxation times are proportional to $T^{\frac{3}{2}}/n$).

Keeping this in mind, we will next compare various broadening mechanisms based upon these approximate theories to determine that Doppler broadening will be the dominant profile effect.

i. Doppler Broadening

For a Maxwellian distribution of emitting atoms the full-width at half-maximum from Doppler broadening is given by[47],

$$\Delta\lambda = (7.7 \times 10^{-5})\ \lambda\ \left(\frac{KT_i}{A}\right)^{\frac{1}{2}} \qquad (3.4)$$

where $\Delta\lambda$ is obtained in Angstroms (Å) if λ is in Angstroms, KT_i is in electron volts, and A is the atomic weight. For the He II 4686 Å line, this becomes, $\Delta\lambda = (.1807)(KT_i)^{\frac{1}{2}}$. Typical experimental temperatures on the order of 10eV then have a Doppler width of about 0.57 Å.

It should be mentioned that for a Maxwellian plasma the intensity of the line as a function of wavelength will have a Gaussian shape.[47] Other distribution functions will have other shapes. It can be a rather involved process to determine these shapes exactly unless the instrumental profile is very sharply peaked compared to the actual profile shape. Otherwise various trial line shapes must be convoluted with the instrument profile and then fitted with the output profile.

In our experiment only slight deviations from a Gaussian shape occur. In addition, energy analyzer measurements indicate that, under most conditions, the bulk of the plasma is Maxwellian. We will therefore not be concerned with the above complications.

ii. Zeeman Effect

The presence of a magnetic field in the experiment can cause broadening, in addition to the Doppler effect, on the order of,

$$\Delta\lambda = 10^{-9}\,\lambda^2 B \tag{3.5}$$

where $\Delta\lambda$ will be given in Angstroms if λ is in Angstroms and B is in kiloGauss. The effect will be important only at low temperatures, where Doppler broadening is small, and for large magnetic fields.

In the experiment, the Fabry-Perot interferometer views a path across the midcylinder of the octupole. The magnetic field strength varies from about 200 G, near the peak in density, to about 1 kG, near the edge of the plasma. Zeeman broadening for 1 kG fields is 0.02 Å. It would thus be observable at the plasma edge only for temperatures below about 0.01eV, from Eqn. (3.4). Further into the plasma, where most of the line radiation for an optically thin plasma originates, the Zeeman effect will be even less significant and can be neglected for all practical purposes.

iii. Stark Broadening

Collisional broadening can occur when the lifetime of an excited state of an atom is long compared to the collision time with other particles. Collisions can take the form of interactions with the microfields of neighboring atoms.

Detailed methods of calculating the amount of broadening expected are given in Griem.[48] A more approximate result for hydrogen-like atoms, also given in reference 48 is,

$$\Delta\lambda = \frac{p^2 a_o^2 e^2}{4\pi\varepsilon_o} \frac{\lambda}{\hbar\omega} \frac{1}{\rho^2} \qquad (3.6)$$

where p is the principle quantum number of the upper state of a given transition, a_o^2 is the Bohr radius, ε_o is the dielectric constant of vacuum and ρ is an impact parameter which is approximated by,

$$\rho = (\frac{4\pi n}{3})^{-\frac{1}{3}} \qquad (3.7)$$

We see from this that the Stark width is mainly dependent upon density, being proportional to $n^{\frac{3}{2}}$. For maximum densities in the octupole of about $n = 1 \times 10^{12}$ cm^{-3} line broadening by this process will be on the order of a thousandth of an Angstrom and so can be completely neglected. It is generally important only when $n > 10^{15}$ cm^{-3} for temperatures on the order of a few electron volts.[47]

B.2. Experimental Procedures

The experimental instrument made use of a commercial etalon (Burleigh model TL-15) with 13 mm diameter plates. Plate spacing can be varied in seven discrete increments between 0.01-1.0 cm using invar spacers. From Eqns. (3.11) in the appendix and for λ =4686 Å, the free spectral range can then be varied between $\Delta\lambda$ = 11 Å-0.11 Å.

The etalon plates are flat to within $\lambda/100$, where λ = 5000 Å. Typical losses in the dielectric coatings due to absorption and scatter are 0.2%. Assuming perfectly flat plates, the maximum transmittance is given by,

$$\varepsilon = (1 - \frac{.002}{1-.93})^2 = 97\% \quad .$$

When the reflectivity finesse, F_A, is on the order of the plate flattness finesse, F_C, further reduction in the transmission will occur.[49]

From Eqn. (3.13) the reflectivity finesse is F_A=43, and from Eqn. (3.18) the flattness finesse is F_C=50 for $\lambda/100$ plates. The total mirror finesse is given by Eqn. (3.14) in the appendix, F_m=32. The effect of plate error reduces ε by a factor of 0.8 so the net transmittance should be better than 77%.

The maximum resolution is determined by the mirror finesse. For minimum plate spacing (0.01 cm), $\delta\lambda = \Delta\lambda/F_m = 0.34$ Å and for maximum plate spacing (1 cm) $\delta\lambda = 0.0034$ Å.

For expected plasma temperatures in the range $T_i \simeq$ 1-20eV, the Doppler broadening is 0.2 Å-0.85 Å. A plate spacing of 0.5 mm was chosen to give adequate resolution ($\delta\lambda = 0.07$ Å) while at the same time keeping a wide enough free spectral range ($\Delta\lambda = 2.2$ Å) to include most of the broadest line expected.

Scanning of the plates is achieved by means of 3 piezoelectric (PZT) pushers and is electronically controlled. Plate movement is 2.5μm per 1000^V applied to the PZT's and is linear with voltage to within 1%. Voltage is thus proportional to the wavelength to which the system is tuned. At λ = 4686 Å each order of interference is separated by 93.6 volts on the PZT's, which means that 0.024 Å are scanned per volton the PZT's.

The predisperser consists of a 10 Å bandwidth interference filter centered at λ = 4688 Å with a ±6.5% variation in throughput over a free spectral range centered at λ = 4686 Å. Throughput efficiency is about 40% at λ = 4686 Å. The bandwidth of the filter was chosen to block the He I 4713 Å line, which is considerably brighter than the λ = 4686 Å line early in time after gun injection.

The collimator lens has a focal length of 254 mm with a pinhole limited resolution of $\delta\lambda_p$ = 0.044 Å from Eqn. (3.17) of the appendix. The overall instrumental resolution is then $\delta\lambda_I = ((\delta\lambda_m)^2 + (\delta\lambda_p)^2)^{\frac{1}{2}} =$ 0.083 Å, using Eqn. (3.14). An improvement in throughput could have been attained by increasing the pinhole size, but this would decrease the resolution, which was undesireable.

The detector was a 1P21 photomultiplier used without refrigeration. Refrigeration would have greatly reduced the dark current and improved the signal to noise ratio, facilitating measurements of low light levels often encountered in the experiment.

Etalon plate adustments produce parallelism of the plates when uniform illumination is obtained on a card placed in the focal plane of the collimating lens, using an expanded beam monochromatic laser source to provide incident flux. This adjustment could also be performed by illuminating the etalon with an extended, monochromatic source and adjusting plate angles until the bullseye pattern is unchanged as one scans across the plates by eye. A third technique involves adjusting the plates for maximum output and resolution for a monochromatic source of light, which is more convienient once the instrument is permanently in place on the octupole.

A rough check of the actual resolution of the instrument and calibration of the voltage scale was performed from measurements of the He I 4713 Å line, using a helium spectrum tube. A 100 Å interference filter centered at λ = 4686 Å was used for predispersion. Line widths of 0.14 Å were measured with voltage separation between orders equal to about 94 volts ±5 volts. The voltage scale, then, is quite accurately related to wavelength scale and is close to instrument specifications.

The resolution, on the other hand, is almost a factor of 1.7 times the theoretical value. If the natural linewidth of the 4713 Å line were $\delta\lambda \simeq 0.1$ Å then the above measurement would be roughly the convolution of the actual natural line width with the instrumental function. Since we have not determined the natural line width, we will assume as a worst case that the resolution is given by the measured value $\delta\lambda \simeq 0.14$ Å.

Keeping in mind all of the background information on the instrument developed in this section, sample line profiles for the He II 4686 Å line are shown in Figs. 14 and 15. The profiles were taken on the octupole using gun injected helium plasma.

The profile in Fig 14 was taken 1 millisecond after gun injection and has a Doppler width of 1.2 Å, while the profile in Fig. 15 was taken 9 milliseconds after injection and has a width of about 0.5 Å. Both measurements are close to the actual widths since the resolution of the instrument is better than 0.14 Å. The error bars represent

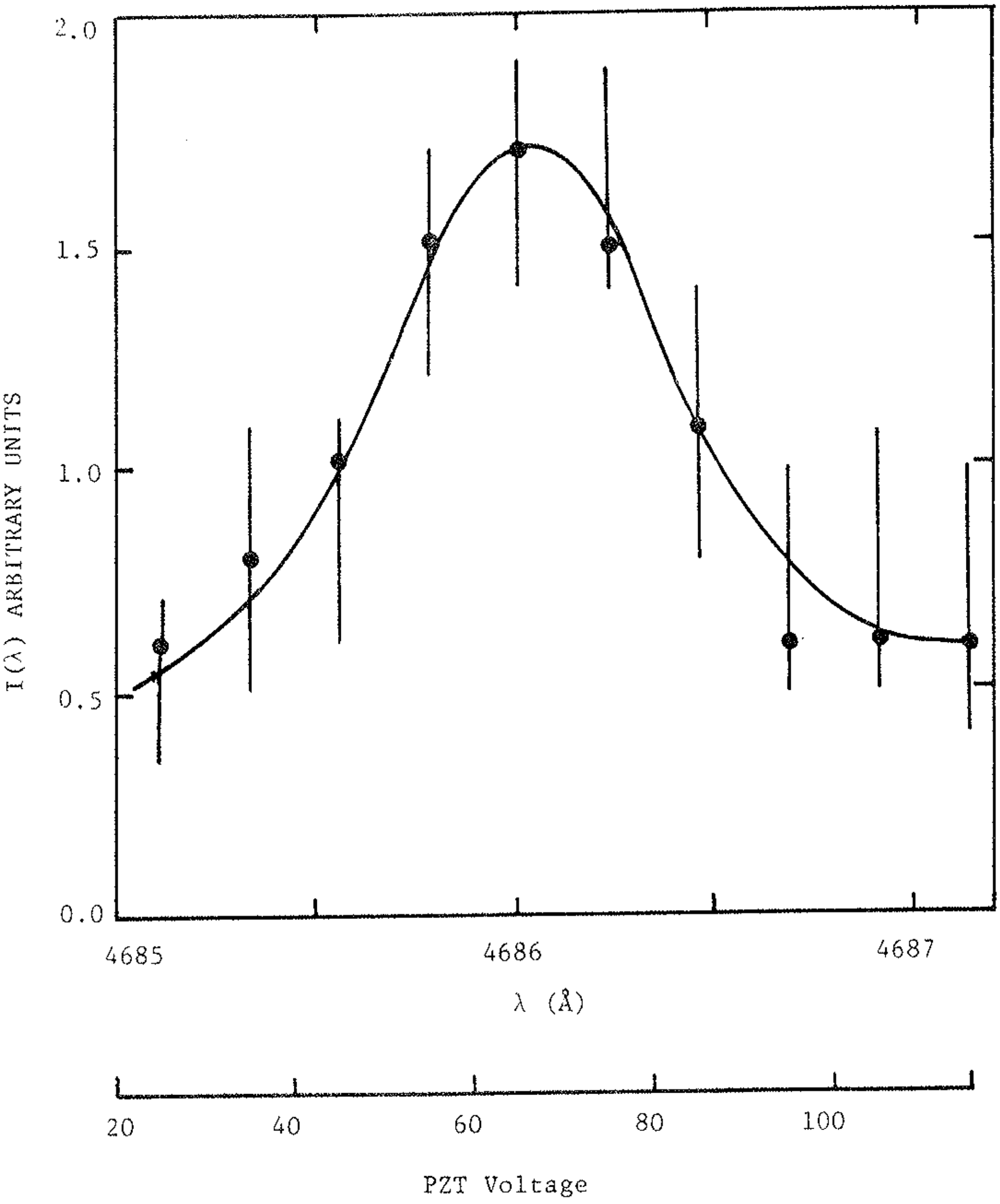

Figure 14. Line profile of He II 4686 Å taken 1 ms after plasma injection.

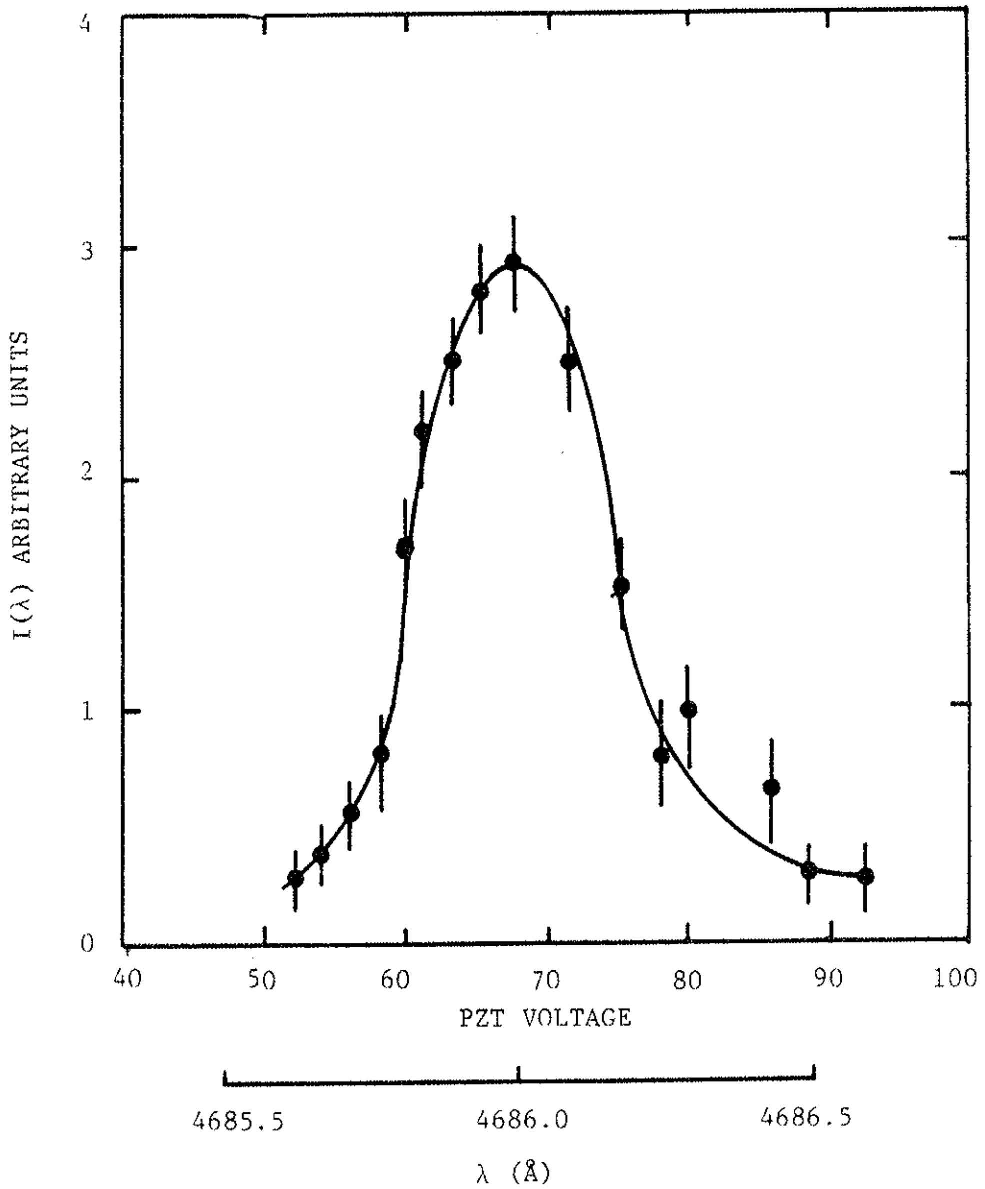

Figure 15. Line profile of He II 4686 Å line taken 9 ms after plasma injection.

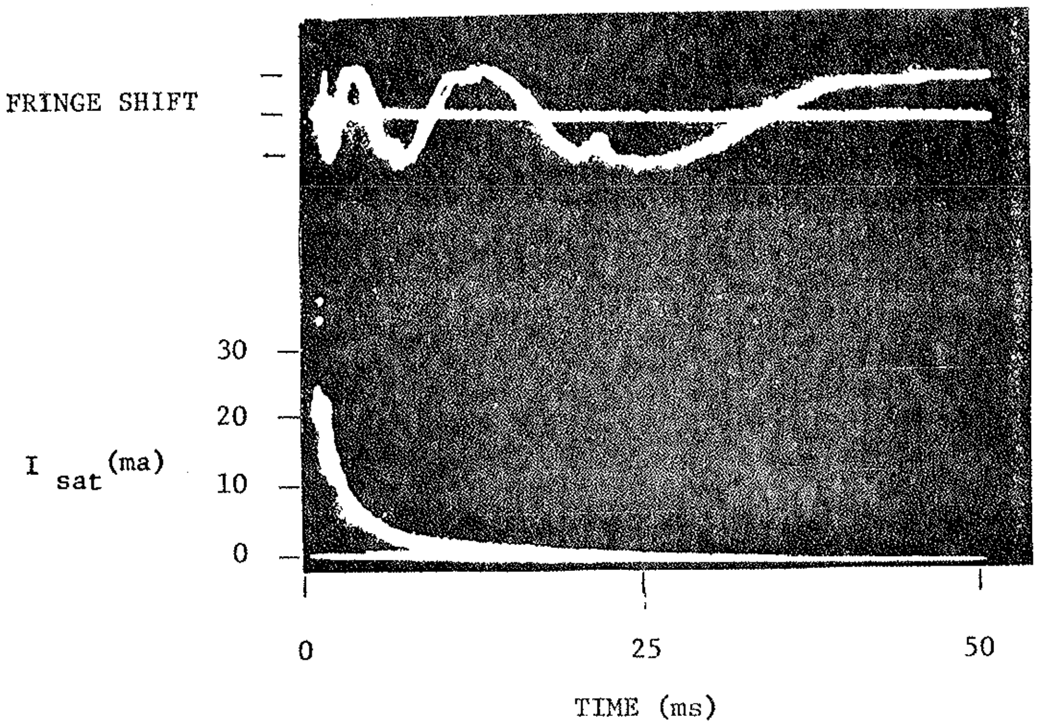
FRINGE SHIFT
30
20
I_{sat} (ma)
10
0
0
25
50
TIME (ms)

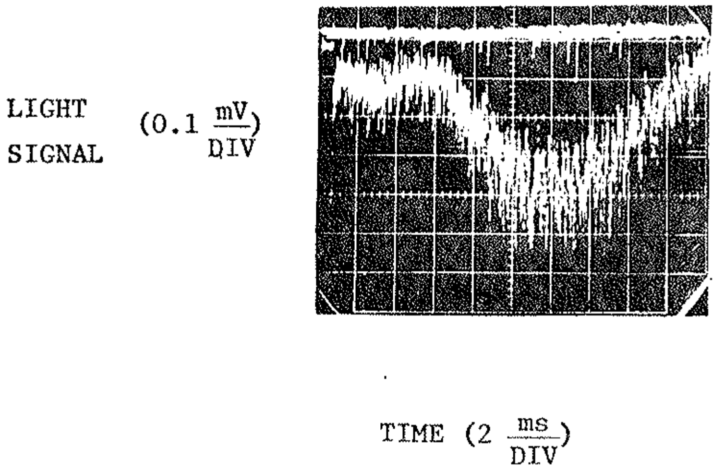
LIGHT SIGNAL
(0.1 $\frac{mV}{DIV}$)
TIME (2 $\frac{ms}{DIV}$)

bars in Fig. 14 are due primarily to lower light levels with only slightly decreased noise levels early in time after gun injection.

The measured line widths at a number of times after plasma gun injection in addition to Figs. 14 and 15 are shown in Fig. 17. The linewidths decrease rapidly in the first 2 milliseconds, then remain roughly constant at about 0.5 Å for essentially the lifetime of the plasma. This is much broader than the instrumental resolution. Recalling our earlier discussion, it is probably the case that after the first 2 milliseconds, we are measuring only the natural linewidth of the radiation, which we know is close to 0.5 Å.[45] The true Doppler broadening is thus only slight and the temperature is a few eV at most late in time.

For earlier times, considerable broadening is apparent (up to 1.6 Å). Figure 18 provides an estimate of the temperature range that can be calculated from these Doppler widths. The dashed curve represents the absolute maximum temperatures that can be deduced from the line widths. It ignores the natural linewidth of the radiation. The solid curve in Fig. 18 is a more conservative estimate found by subtracting the minimum linewidth measured (0.4 Å), which is close to the natural linewidth, from the values indicated in Fig. 17. We find that the temperature is initially $\gtrsim$ 40eV with an e-folding time of about 0.4 millisecond. The rapid temperature decay is indicative of very substantial ion energy losses. These temperatures will be compared with energy analyzer measurements in the next section.

Before concluding, it should be mentioned that when a substantial

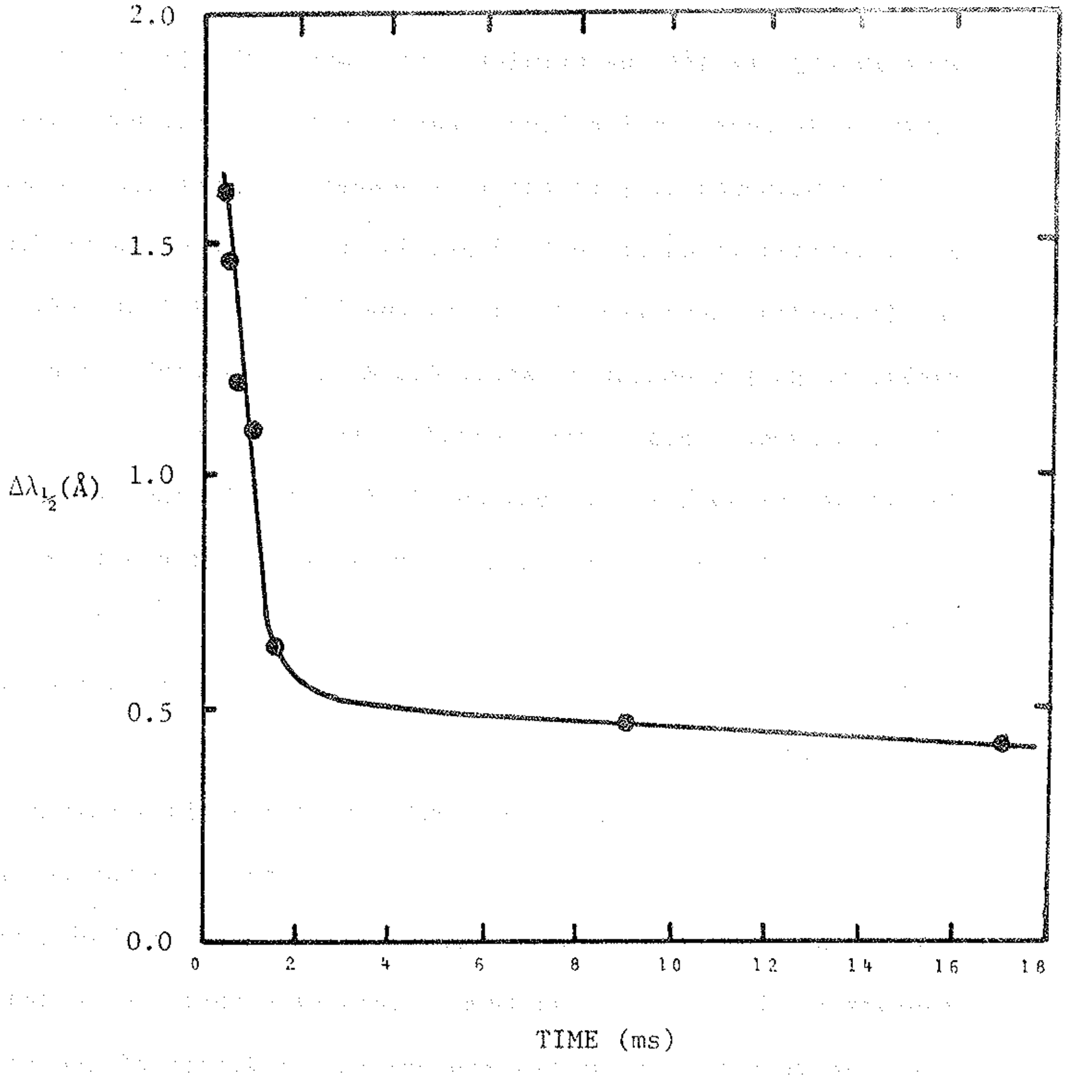

Figure 17. Measured full widths at half maximum for Doppler broadening of He II 4686 Å versus time after plasma injection.

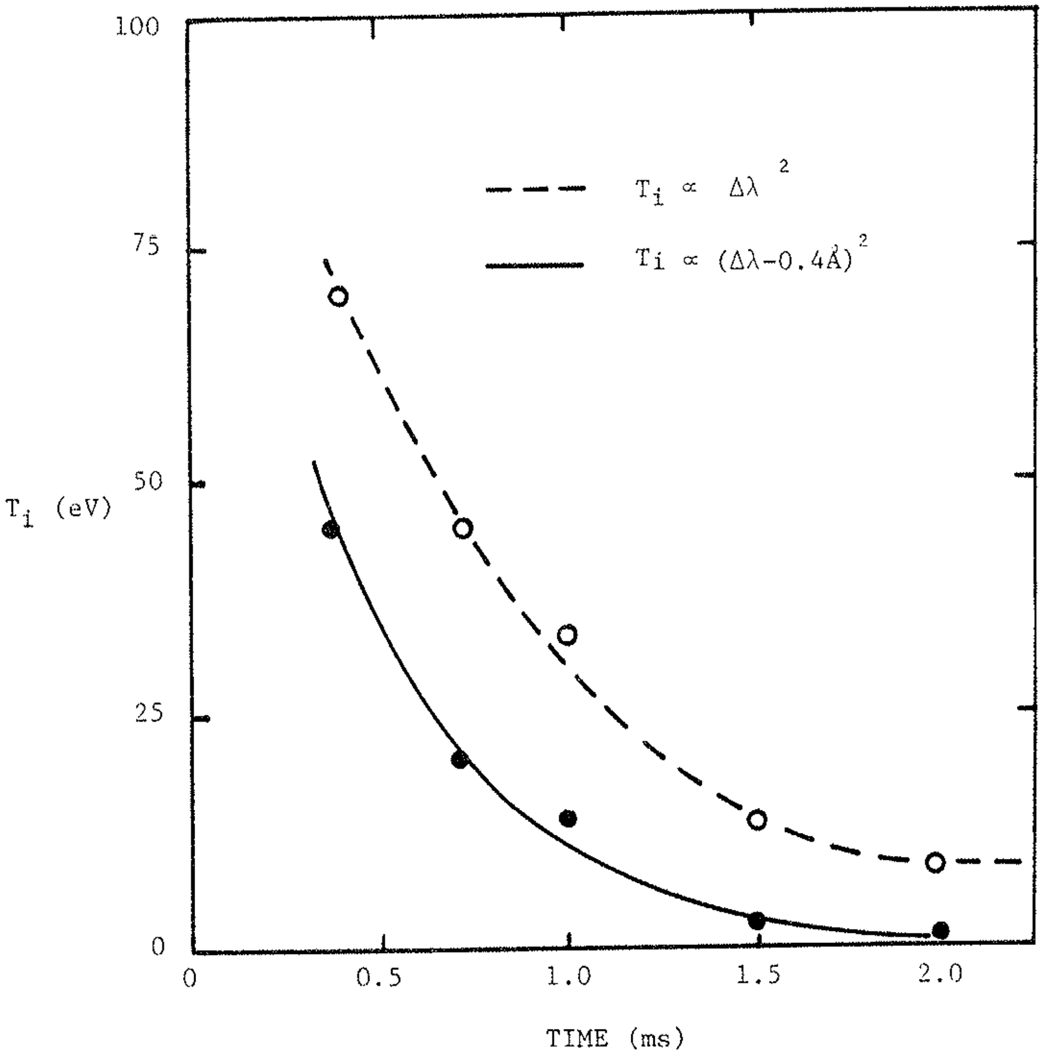

Figure 18. Ion temperature versus time after plasma injection deduced from Doppler broadening measurements of He II 4686 Å line.

part of the line profile extends beyond the free spectral range under observation, some error will be produced by superposition of the additional light from outside of that range. Its distribution in the spectral range being considered will depend upon the relative orders of interference between it and the main spectral components. For simplicity, we have ignored this effect here. It may be responsible for some of the assymetries observed in the measured line shapes.

C. Gridded Energy Analyzers

The spectroscopic ion temperature measurements discussed in the last section have a number of shortcomings, in addition to the complexity of line profile interpretation. First of all, spacial information is not easily obtainable in the configuration of the diagnostic described. This would require knowledge of the point along the density profile where peak emission of the line occurs, which cannot be adjusted independently of the temperature. Secondly, due to the contrast limit of the Fabry-Perot, only a limited range of energies in a given energy distribution can be measured. It can be easily shown that the maximum measureable wavelength deviation about the peak in the line profile is given by,

$$\frac{\Delta\lambda}{\Delta\lambda_{\frac{1}{2}}} = \left[\frac{\ell n\left(\frac{I\max}{I\min}\right)}{\ell n 2}\right]^{\frac{1}{2}} , \qquad (3.40)$$

where $\Delta\lambda_{\frac{1}{2}}$ is the Doppler half-width. For our instrument, Imax/Imin = 28 and so, $\Delta\lambda = 2.2\ \Delta\lambda_{\frac{1}{2}}$. Thus, the maximum energy in the distribution function that can be measured is only a factor of 2.2 times the thermal velocity.

Energy analyzers overcome both of the above difficulties, allowing both spacial information and a wide range of energy ditribution to be easily obtained. The type of analyzer used most often in the experiment is shown schematically in Fig. 19. It is a modified form of the type of analyzer used in references 54 and 55 and measures predominantly the ion energy distribution perpendicular to the magnetic field.

The axis of the analyzer is perpendicular to the magnetic field. The distance between the entrance hole and the collector plate is less than about 0.7 millimeter. In principle, ions with gyroradii greater than this are able to reach the collector, while electrons with much smaller gyroradii are skimmed off by the surface grid of the analyzer. For typical magnetic field strengths of about B=1.5kG this corresponds to collection energies of T_i > 1eV for hydrogen and T_i > 0.25eV for singly ionized helium. Accurate use of the analyzer will be restricted to ion temperatures greater that these values.

Metal parts of the analyzer are made of stainless steel and insulators are made of teflon. The wires of the first grid need not be finely spaced since they act only as obstacles for electrons moving along field lines. The second grid, on the other hand uses a fine mesh (0.1 mm wire spacing) with about 50% transparency. Biased with a variable positive voltage it acts as an ion discriminator and must maintain an equipotential across the plane of the grid.

The collector consists of a shallow cup about 0.2 mm deep. The

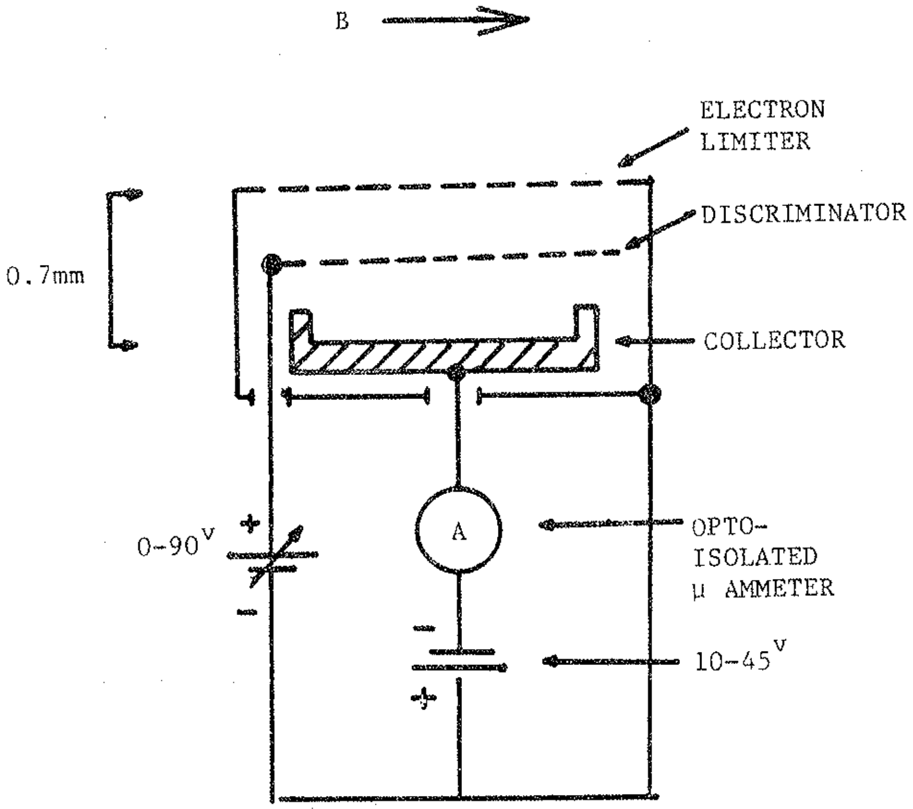
B
ELECTRON
LIMITER
DISCRIMINATOR
0.7mm
COLLECTOR
0-90^{V}
+
−
A
OPTO-
ISOLATED
μ AMMETER
−
+
10-45^{V}

Figure 19. Perpendicular gridded ion energy analyzer.

cup reduces secondary electron emission from the surface of the collector since any secondary electrons will flow along the magnetic field lines parallel to the surface of the collector and be recollected on the side wall of the cup. Because these low density, low energy, electrons stick quite well to the field lines the cup depth need not be great.

The collector is biased negatively with respect to the case of the device, which is at the floating potential in the plasma environment. This negative bias eliminates electron currents that result from secondary emission from the first two grids and from residual electron flux not skimmed off at the entrance grid.

A sample of the probe output is shown in Fig. 20. Collected ion flux is plotted versus positive bias votage on the discriminator grid. We find that the logarithm of the relative flux is linearly related to the bias voltage over more than two orders of magnitude in collected flux. This behavior is characteristic of a Maxwellian distribution function. A unique ion temperature may be determined from the slope of the line in Fig. 20 according to,[56]

$$\frac{\Delta V}{\Delta \ell n \Gamma} = \frac{KT_i}{e} \qquad (3.41)$$

If the voltage V is expressed in volts then KT_i/e will be in units of electron volts.

A good deal of experimentation and development has gone into the final design of the analyzer. The first analyzer tested was of

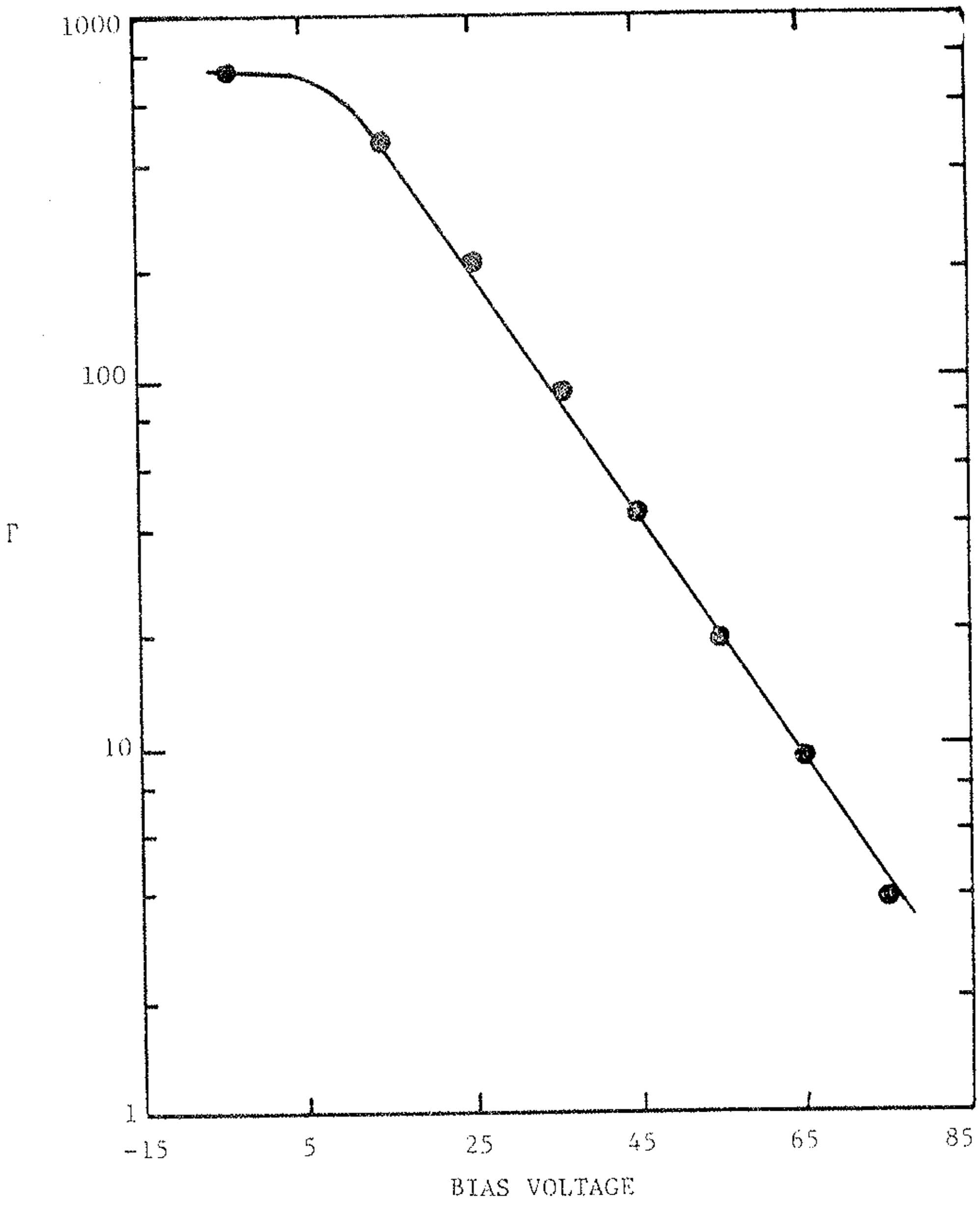

Figure 20. Collected ion flux, Γ, versus discriminator bias voltage for energy analyzer.

standard design[54,55], and did not have the second grid. The collector was biased a few volts negative with respect to the case to eliminate secondary electrons but positive with respect to the plasma potential to discriminate ion energies. Large electron current collection in this analyzer prevented ion temperature measurements. Electron collection could be reduced but not eliminated by placing a ring around the entrance to the analyzer or by using it in the high field ($B \gtrsim 2.5$kG) inner bridge region of the octupole. Sensitivity of electron current collection to magnetic field was also observed by Motley et. al.[58] They found that the magnetic field had to be above about 3kG before electron skimming became effective. It became clear that many of the electrons collected were a result of an anomolous electron diffusion across the field lines into the analyzer. Minimum electron currents in the inner bridge region of the octupole were about one-tenth of maximum ion currents. They increased with increasing positive bias to distort the higher energy part of the distribution function, giving low ion energy readings.

These electron currents were substantially reduced by adding a second electron repelling grid in front of the collector. The first analyzer of this design used on the octupole was constructed by David Brouchous. Unfortunately, the small amount of remaining electron current was still enough to prevent clear ion temperature measurements under many conditions. The source of these electrons is not clear but may be due to secondary emission from the second grid itself, or from insufficient repelling of external electrons.

It was found experimentally that these remaining few electrons could be eliminated completely by simply altering the biasing arrangement of the various electrodes to the final form shown in Fig. 19 and described at the beginning of this section.

One final problem was secondary emission by the collector. As we have seen, secondary emission at the grids or any other external flux of electrons produces a decrease in ion current at the collector and an effective lowering of ion energy readings. Secondary emission at the collector, on the other hand, results in an increase in ion current at the collector and an apparent increase of ion energy readings. Testing of the analyzer shows that this effect appears only as an apparent tail on the distribution function and is most apparent for low plasma temperatures.

The emission could be reduced by lowering the negative bias on the collector. This reduces the acceleration of ions into the collector and the associated secondary electron emission.

There are a number of complications in interpreting the data even after electron collection has been eliminated. First of all, particles with large ratios of velocity along the field lines to velocity perpendicular to the field lines will strike the walls of the analyzer or the grid wires because of geometrical considerations. This is expected to be a small effect, however, because the ratio of diameter to height of the analyzer is large (≈ 7). In addition, only the low energy part of the analyzer characteristic should be affected.

A second source of complexity arises because the guiding centers of high energy ions are farther from the analyzer than low energy ions. If there are significant density gradients over an ion gyroradius, the flux at a given energy will have to be weighted according to its respective density. The largest gyroradius encountered in the experiment is about 0.4 cm which is much less than the scale length of density variation ($\gtrsim$ 4 cm). This effect is therefore not expected to be important, unless the probe itself severely perturbs the density over distances of an ion gyroradius. A number of other sources of error involved in interpreting the analyzer characteristic are discussed in reference 55 and do not appear to be significant.

Keeping the above considerations in mind, sample ion temperature measurements were taken in a hydrogen plasma produced by gun injection and are shown in Fig. 21a. Results are compared with ion temperature measurements from a different gridded analyzer[57] placed in the zero magnetic field region at the center of the octupole. Because there is no magnetic field there, this analyzer does not suffer from the geometrical complications of the perpendicular analyzer. The comparison thereby provides a check on the perpendicular analyzer and an indication of how geometrical considerations affect performance. The agreement between the analyzers is very good except at early times where the perpendicular analyzer gives somewhat higher readings than the zero-field analyzer. It is interesting to note, however, that an analyzer used by Breun[58] also gave consistently higher readings than the zero field analyzer early in time.

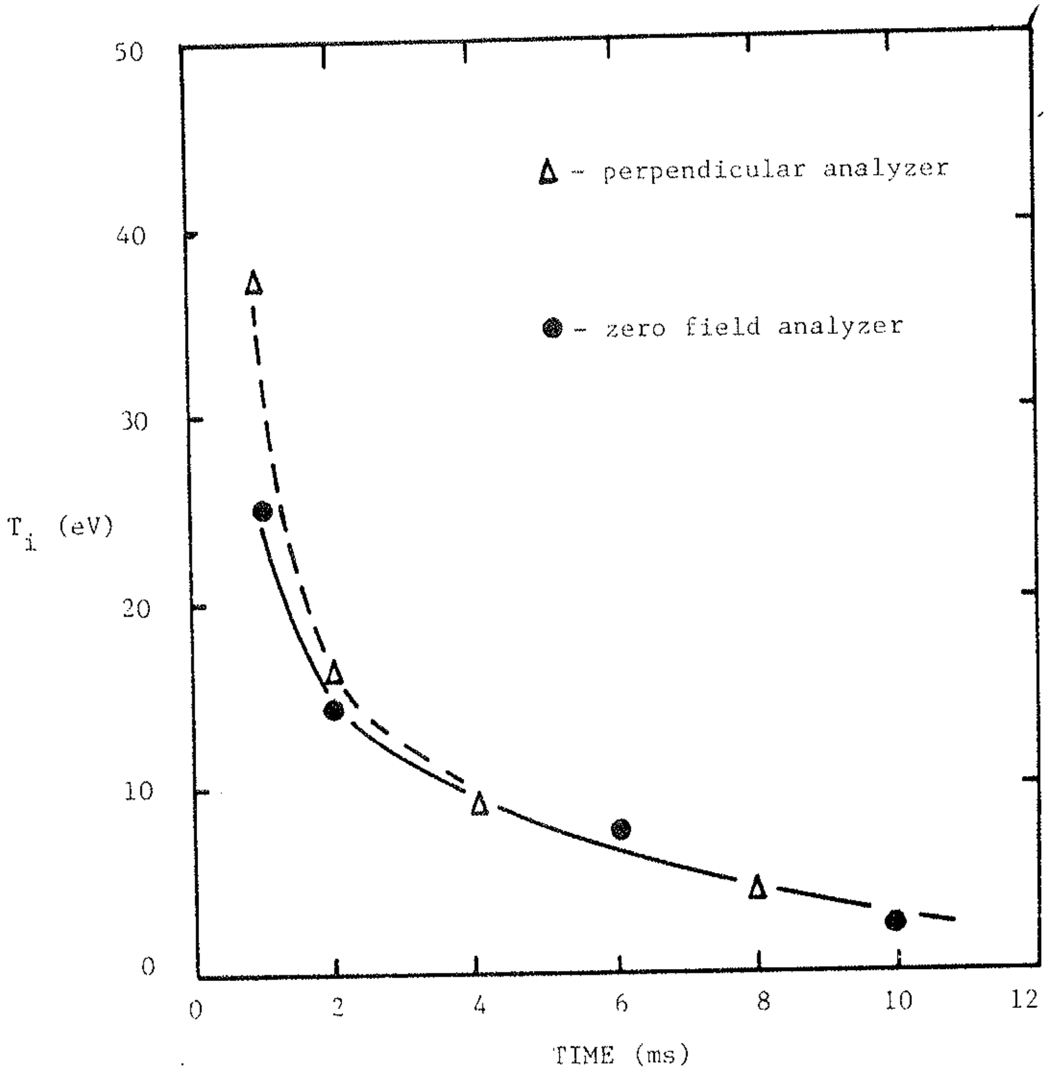

Figure 21a. Ion temperature versus time after plasma injection measured with perpendicular and zero field analyzers in hydrogen plasma.

Gun temperature is dependent upon neutral pressure as shown in Fig. 22b. Lower neutral pressures allow higher temperatures and longer decay times consistent with losses to neutral atoms. Initial temperatures for the hydrogen plasma between 30-50eV are in close agreement with Doppler broadening measurements in the helium plasma displayed in the last section. However, temperature decay times are typically greater than 1.2 milliseconds for hydrogen plasma, a factor of three longer than the decay time observed in the helium plasma. This is very likely because the helium plasma is injected into a higher background neutral density and because helium ion charge exchange cross sections in He gas are larger than proton cross-sections in H_2 gas at the energies in this experiment.[59]

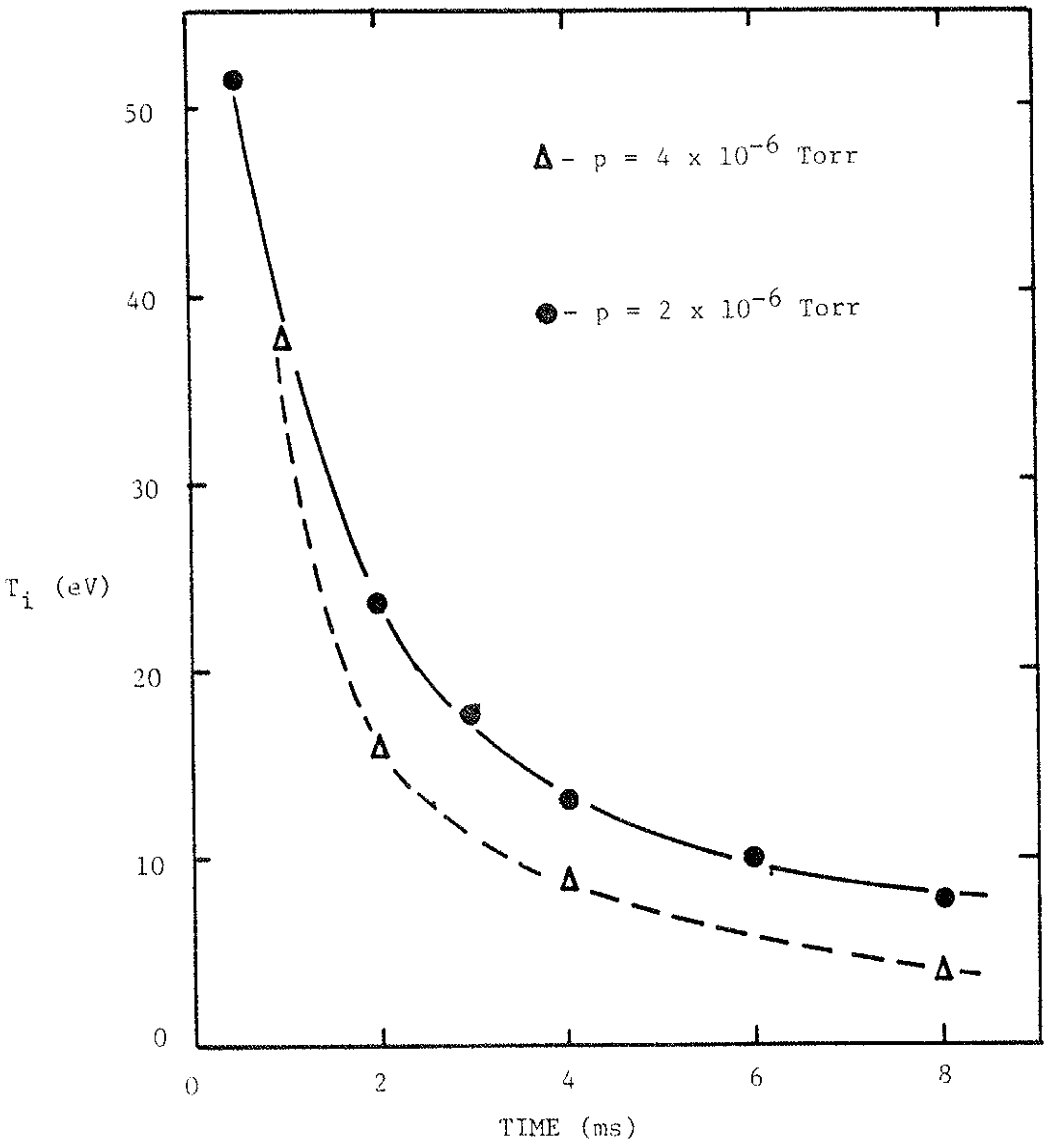

Figure 21b. Ion temperature versus time after plasma injection measured with the perpendicular analyzer for two different background neutral pressures.

CHAPTER 5

ION HEATING ASSOCIATED WITH MODE CONVERSION PROCESSES

In the last chapter we established a basis for confidence in the ion diagnostics and in Chapter 3 we demonstrated efficient wave coupling. We are now in a position to analyze ion heating by the lower hybrid wave. Variations in ion heating with density, magnetic field, spacial position, and power level together with the wave measurements in Chapter 8 will provide a fingerprint by which an identification of mode converion processes, described theoretically in Chapter 2, can be made.

A. Bulk Ion Heating

Before going into very detailed measurements of ion heating using the energy analyzers, we will first verify by a separate diagnostic, the optical Fabry-Perot interferometer, that ion heating is in fact occurring. Magnitudes of the ion temperature determined from Doppler broadening of the He II 4686 Å line can be compared to the energy analyzer measurements in the next sections of this chapter to establish some credibility in their calibration.

Sample Doppler profiles before wave heating and after wave heating are shown in Fig. 22. The experimental sequence of events involved in taking these profiles is shown in Fig. 23. A 2 ms pulse of 40 kW of wave power is injected into a helium plasma beginning 3 ms after gun injection with an initial density of $n \simeq 8 \times 10^{11}$ cm^{-3} measured on the

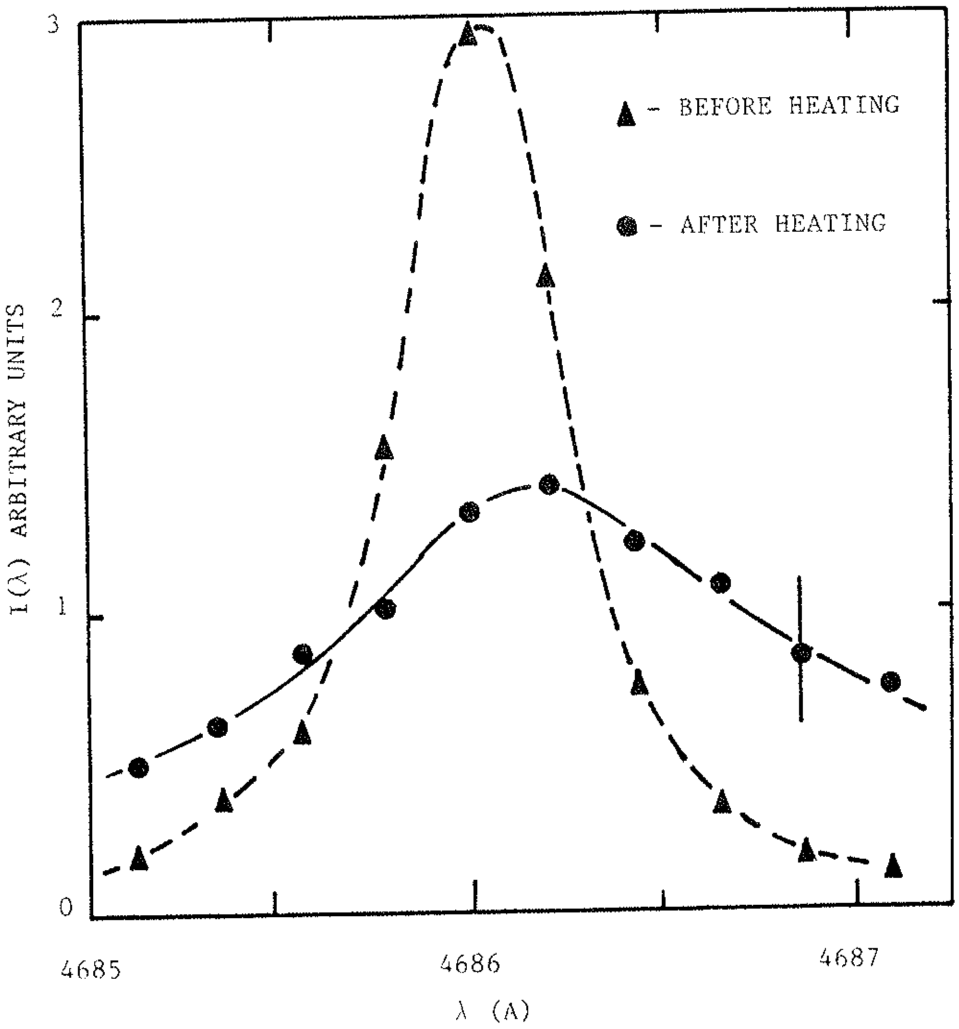

Figure 22. Doppler broadened line profiles before and after 40 kW of wave power. Peak density before heating is $n = 8 \times 10^{11}$ cm^{-3}.

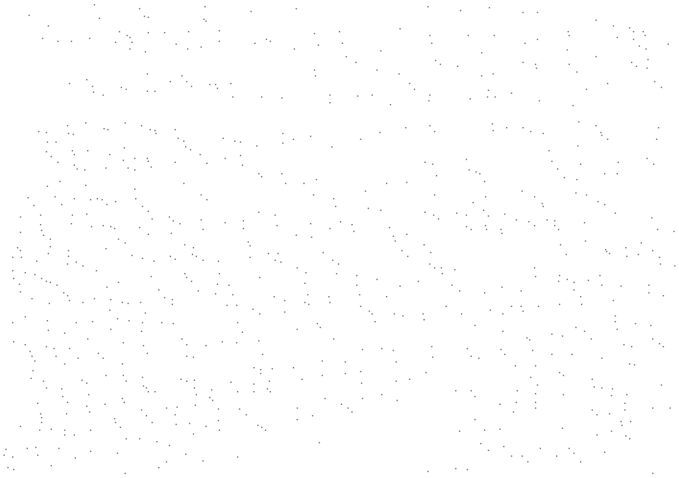

Figure 23. Upper photo: 35GHz microwave interferometer fringe shift and ion saturation current versus time after helium plasma injection (intermediate gun). An additional interferometer fringe exists off the scale of the photo.

Lower photo: Light signal and RF power versus time after plasma injection. Wave power = 40kW turned on at t ≈ 3ms.

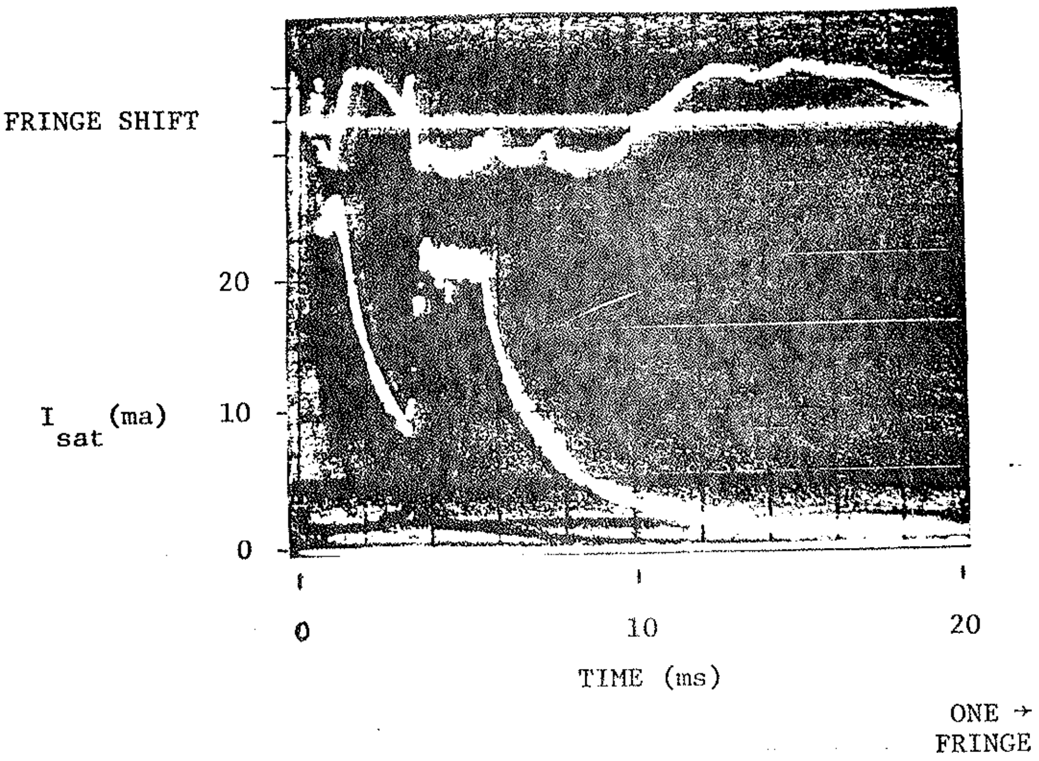
FRINGE SHIFT
I sat (ma)
20
10
0
0
10
20
TIME (ms)
ONE → FRINGE

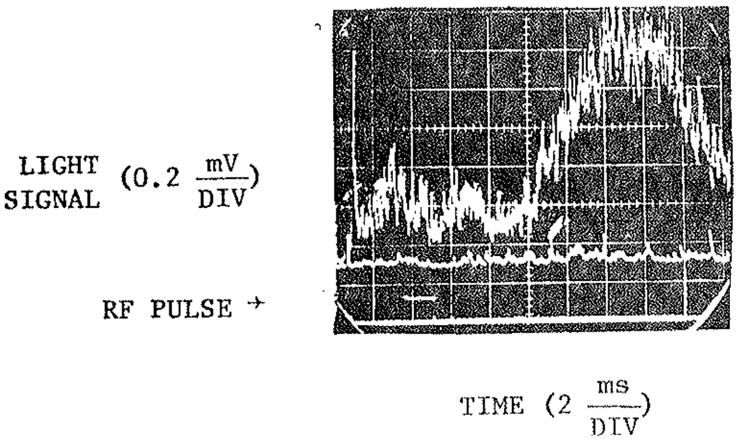
LIGHT SIGNAL (0.2 mV/DIV)
RF PULSE →
TIME (2 ms/DIV)

microwave interferometer. Forty kilowatts is the highest power level that has been injected into the plasma in this experiment. Considerable line broadening is apparent in Fig. 22 after wave heating. The width is 0.56 Å before and 1.6 Å after heating. Subtracting a linewidth of 0.4 Å (recall that this was the narrowest linewidth measured by the instrument in Chapter 4 indicative of the natural linewidth under present conditions) from these values and using Eqn. (3.4) we find a temperature of 3eV before wave heating increasing to 40eV after heating.

We see that the ion saturation current in Fig. 23 after wave heating is brought up to a value close to the initial gun value. Taking into account the smaller density after wave heating and since $i_{sat} \propto n\sqrt{KT}$ the relative value of currents in Fig. 23 indicates that the temperature after wave heating is 1.3 times the initial gun value. We know from the last chapter that the initial temperature of the gun is close to 40eV so the ion saturation current measurement is consistent with the Doppler broadening measurement.

The ion temperature as a function of time derived from Doppler profiles is shown in Fig. 24. The ion temperature decay time is 0.4ms which is 0.2 ms faster than the initial decay time found in Chapter 4 for gun injected plasma alone. Greater losses could be partly due to known increases in background neutrals resulting from unionized residual helium influx from the gun plenum following plasma injection. The decay time is, however, close enough to gun plasma decay times to indicate that the wave does not excite instabilities greater than

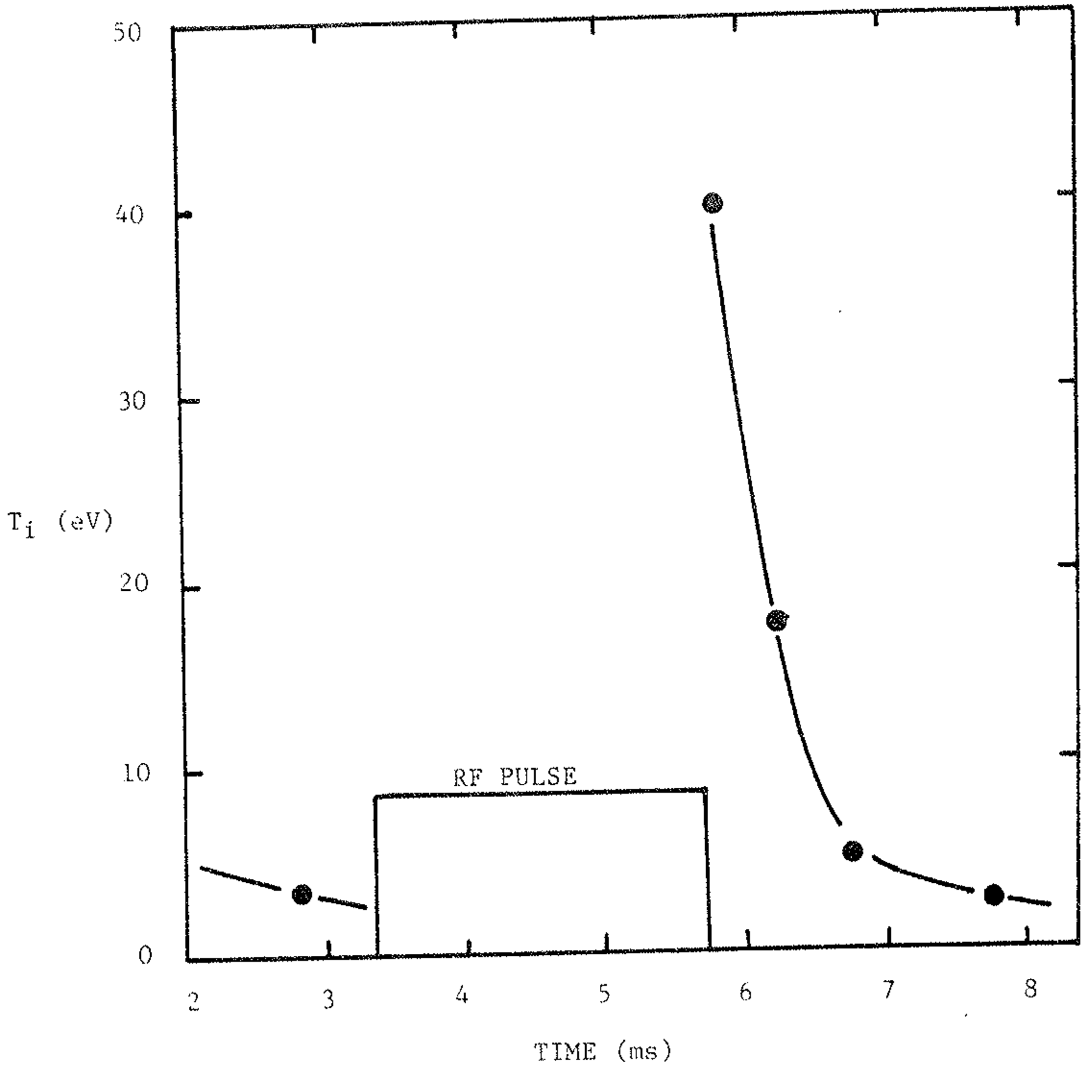

Figure 24. Ion temperature versus time after plasma injection measured from Doppler broadening of He II 4686 Å line. Wave power is 40 kW,and initial density before wave heating is $n = 8 \times 10^{11}$ cm^{-3}.

those present for the gun plasma.

The Doppler broadening measurements have proved to be possible with the present instrument only over a restricted range of experimental conditions. For electron densities below about 5 x 10^{11} cm^{-3}, the wave heating causes a normally strong light signal to vanish completely in a few hundred microseconds. Microwave interferometer measurements show that density decreases are slight on the time scale of the light disappearance. The light signal returns a few milliseconds after wave power is turned off.

The reason for this phenomenon is not known. It is not due to RF interference in the photomultiplier tube or its power supply, since a helium spectrum tube light source placed in front of the instrument does not show a variation in its signal as wave power is applied to the octupole.

At densities above 5 x 10^{11} cm^{-3} wave power levels need to be above about 20kW to have a clear effect on the plasma. This is because of large total gun plasma energies before the wave heating ($n \gtrsim 8 \times 10^{11}$ cm^{-3}, $T \approx 3eV$) and because of rapid energy loss mechanisms in the helium plasma.

B. Ion Temperature Profiles

More detailed information will be obtained in this section using Langmuir probes and the perpendicular ion energy analyzer described in Chapter 4. Energy distributions will be measured in addition to temperature profiles. These measurements will illuminate the physics processes involved and facilitate the determination of heating efficiencies. A hydrogen plasma is used throughout the remainder of this chapter.

B.1. Ion Saturation Current Profiles

This is perhaps the easiest measurement to take on the octupole. It provides a measure of $n\sqrt{KT}$ across the plasma where T is the larger of T_i or T_e.[47] Fig. 25 shows the profiles before RF heating and at two different times during heating for 20kW of incident power.

For this case, the heating peak shifts from about 0.25 inches inside the separatrix before RF heating to exactly at the separatrix after 1 ms of heating. The peak in the ion saturation current increases a factor of 3.4 during the first millisecond, then increases more slowly for the remaining 4 ms of RF heating.

Microwave interferometry indicates that the initial density is 2×10^{11} cm^{-3} and increases slowly over the duration of the RF pulse to 3×10^{11} cm^{-3}. This means that the increase in ion saturation current during the last 4 ms of heating is due primarily to a density increase rather than a temperature increase. The increase during the first millisecond, on the other hand, is caused primarily by a temperature increase which quickly saturates after a millisecond.

These current profiles, unfortunately, do not reveal if electrons or ions are being heatied. Furthermore, the temperature profiles cannot be determined for certain without an independent measure of the density profiles. The following energy analyzer measurements will provide a direct measure of ion temperatures.

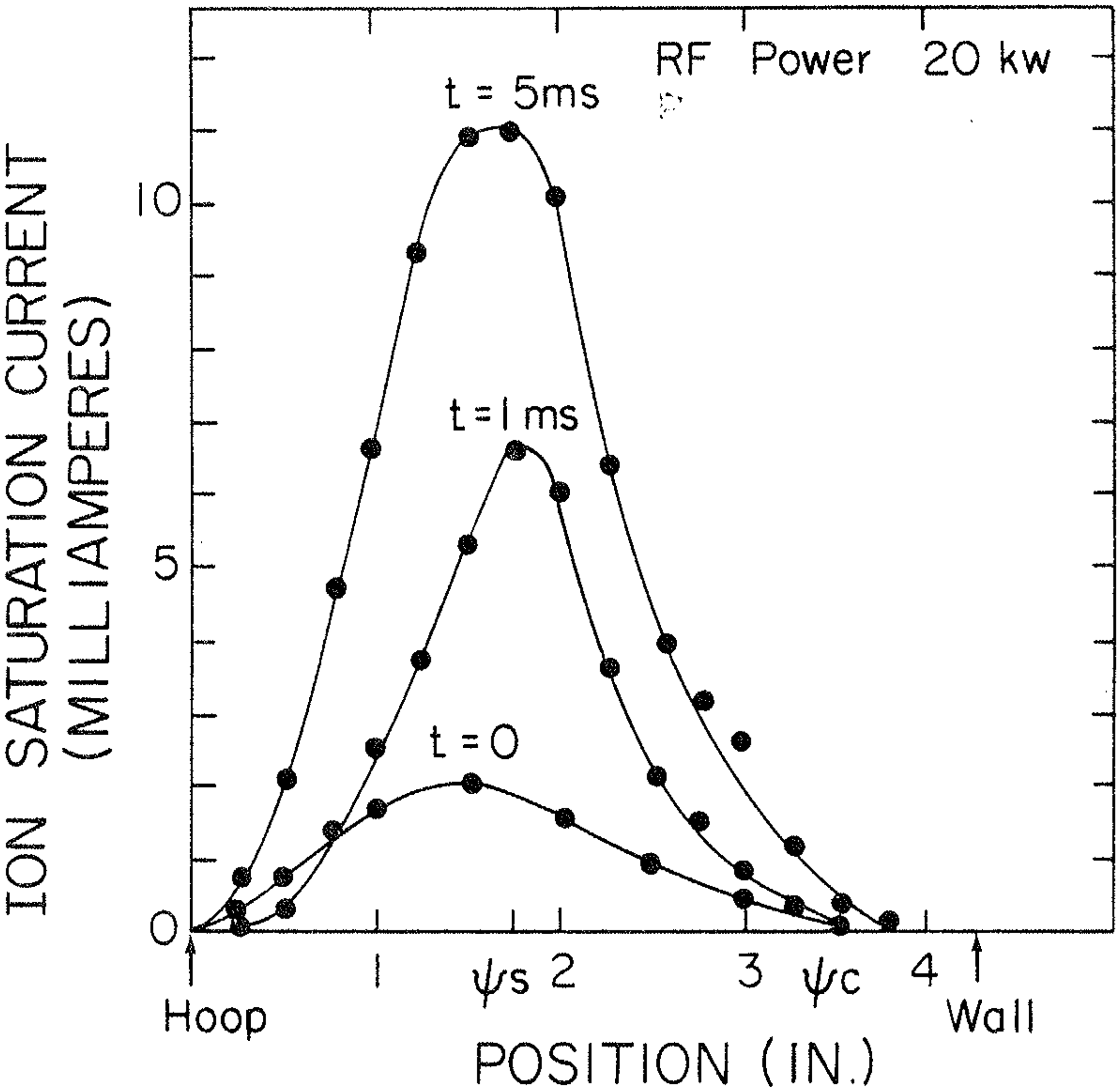

Figure 25. Ion saturation current profiles at various times after wave heating. The t=0 profile is obtained before RF heating.

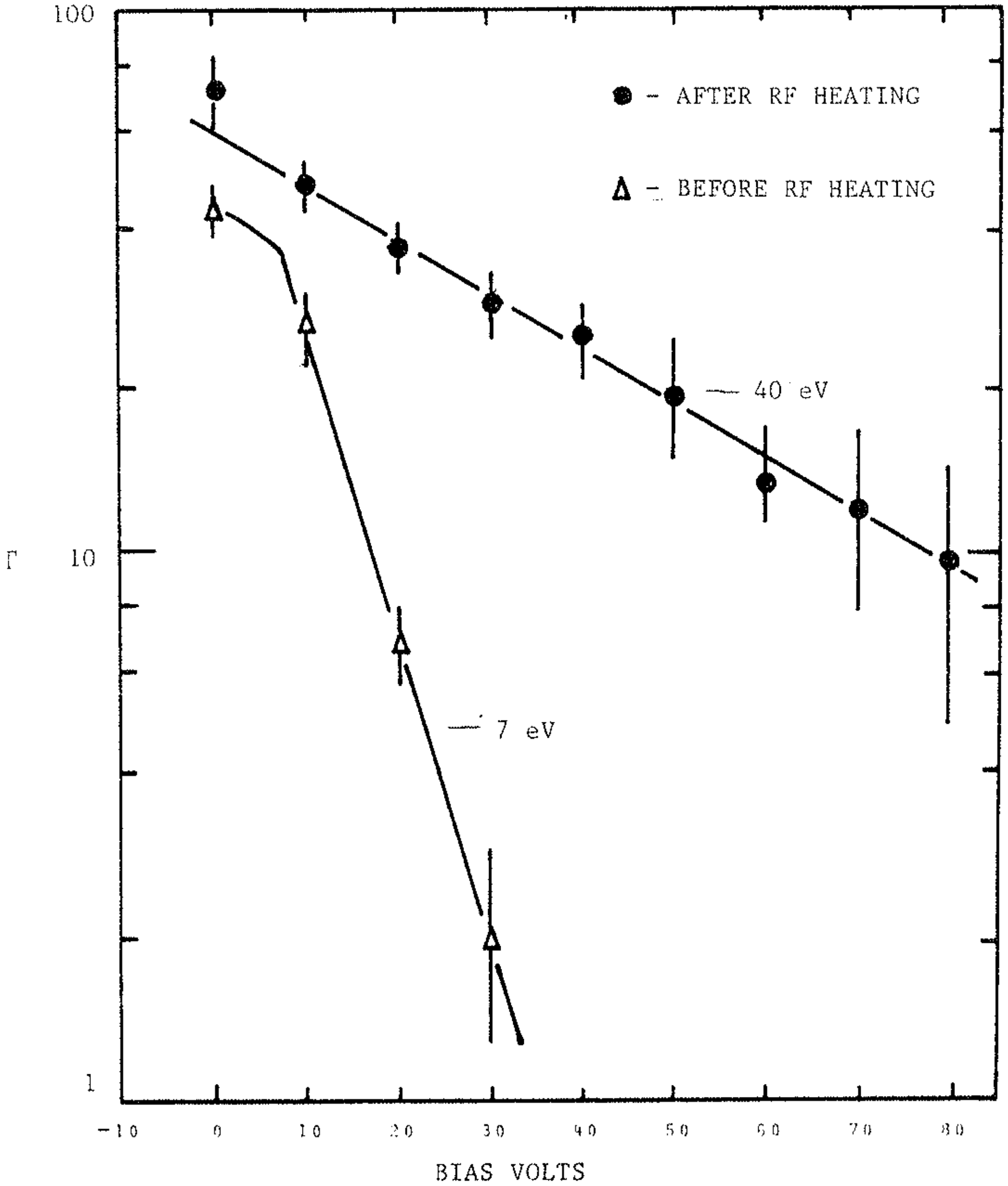

Figure 27. Similar to Fig. 26 except peak density is

$n = 8 \times 10^{11}$ cm^{-3}.

$$\tau_e = 7.2 \times 10^6 \frac{(A_\alpha T_\beta + A_\beta T_\alpha)^{\frac{3}{2}}}{n_\beta Z_\alpha^2 Z_\beta^2 \; (A_\alpha A_\beta)^{\frac{1}{2}} \ln\Lambda} \qquad (5.1)$$

where α and β refer to the plasma components, A is the atomic mass number, Z is the charge, n is the background plasma density, T is the temperature in eV, and $\ln\Lambda$ is the coulomb logarithm. For the 68eV tail shown in Fig. 26, equilibration with a 24eV background plasma having a density of $n \simeq 1 \times 10^{11}\text{cm}^{-3}$ takes at least 2 ms, a time much longer than observed tail lifetimes. Therefore another factor must be involved which shortens tail lifetimes.

Charge exchange cooling of the tail in the present case does not provide an adequate explanation of the short tail lifetimes since, as calculated from formulas in reference 61, the time scale for charge exchange is about 9 ms for measured neutral pressures of $p=2\text{x}10^{-6}$ Torr. This is much longer than thermal equilibration times.

A third possibility is that the tail is lost simply because it is unstable and/or poorly confined relative to the main body. A detailed analysis of this question is beyond the scope of this thesis. However, as will be shown in Chapter 7, plasma that is heated off the separatrix (recall that the present measurement is 2 cm outside) is indeed unstable and is lost very rapidly.

From the theory outlined in Chapter 2, collisionless ion absorption is a finite gyroradius effect. As such, we would expect the high energy portion of the distribution function to absorb wave energy before it is absorbed by the main body. Thus, the observed tail formation is consistent with theory.

Note that with thermal equilibration times on the order of a few milliseconds from Eqn. (5.1), the main body heating can be due largely to energy exchange with the tail particles for RF heating periods from 1.2-10 ms.

The fact that the distribution measured in Fig. 27 is Maxwellian does not mean that there are no high energy tails. They may break away from the Gaussian characteristic at an energy outside the range of measurement. Because of this possbility, it is difficult to speculate on the trends governing tail behavior.

In the remainder of this section we will quote only the main body temperatures, without specifying whether they occur through direct wave-particle interaction or through absorption of tail energy. The perpendicular analyzer will measure the main body of the distribution for energies greater than a few electron volts. Above these temperatures most of the distribution function will have ion gyroradii greater than the distance between the entrance limiter of the analyzer and the collector.

Keeping the above preliminary considerations in mind, the ion temperature profiles in Fig. 28 were taken. Each point is derived by obtaining analyzer plots similar to Figs. 26 and 27, which requires up to ten shots per point. Plasma shot-to-shot variation is less than a few percent as monitored on the microwave interferometer and ion saturation current probes in additon to the analyzer.

The profiles in Fig. 28 are taken at two different densities using

Figure 28. Ion temperature increases across the lower outer bridge region in the same azumuth as the lower hybrid antenna. Hydrogen plasma is produced by the large Marshall gun.

▲ - $n = 3 \times 10^{11} cm^{-3}$

● - $n = 1 \times 10^{12} cm^{-3}$

Wave power = 20kW, initial ion temperature is less than 4eV.

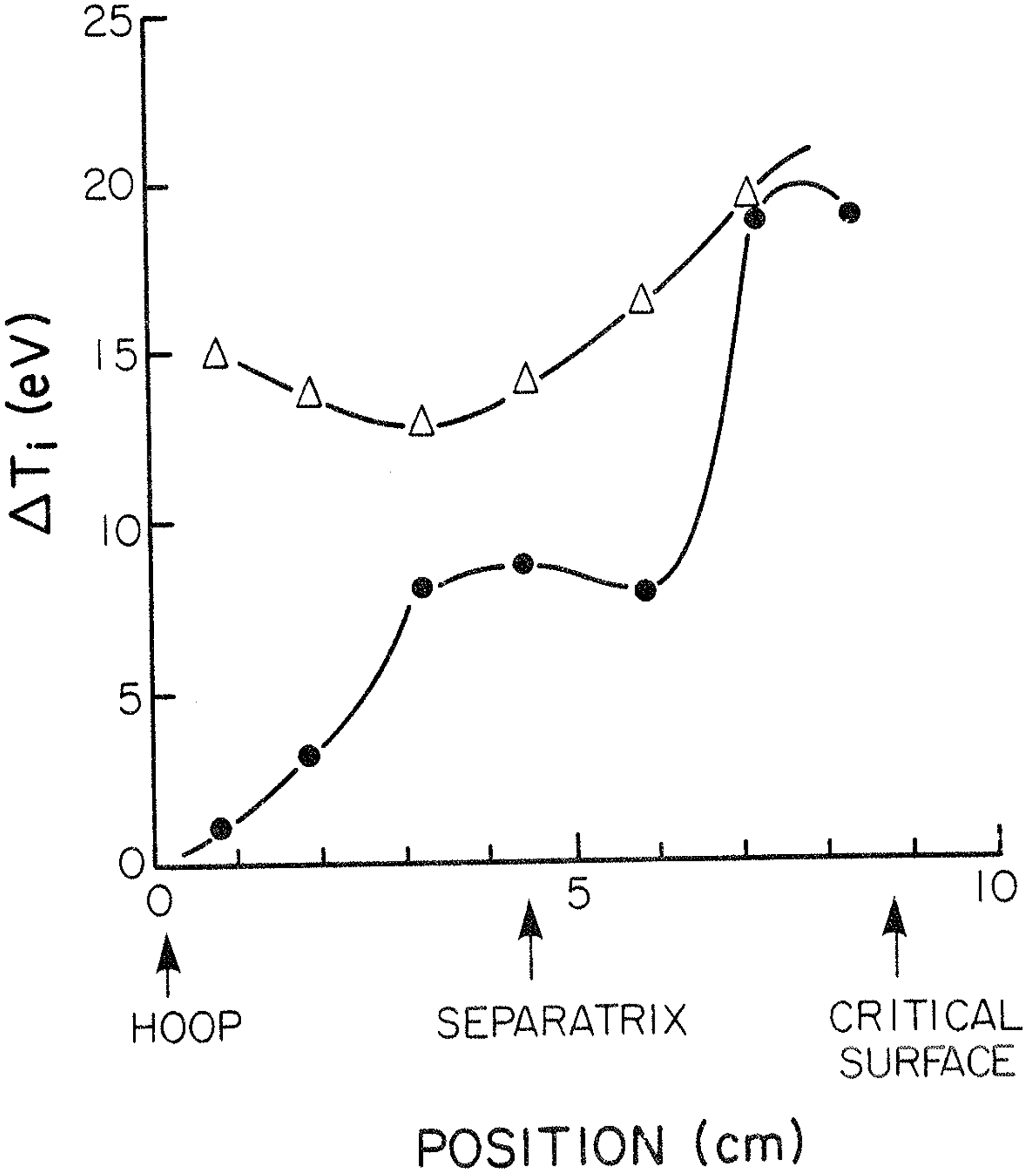
25
20
15
10
5
0
ΔT_i (eV)
0
5
10
HOOP
SEPARATRIX
CRITICAL SURFACE
POSITION (cm)

the octupole's large Marshall gun.[57] The analyzer is placed in the lower,outer bridge region of the octupole in the same azimuth as the lower hybrid antenna. We find, in accordance with theory, a general movement of heating to the plasma core as density is lowered. However, a number of features need additional explanation. First of all, why does substantial edge heating remain when the density is lowered? Secondly, for the high denstiy case, why is there not a second peak in temperature between the hoop and the separatrix, since we found in Chapter 2 that at these densities the resonance exists on both sides of the denstiy profile? Finally, why is heating obtained at a density of only $3 \times 10^{11} cm^{-3}$? The cold plasma theory in Chapter 2 indicated that heating should have vanished below densities of about $n \simeq 7 \times 10^{11} cm^{-3}$.

A plausible answer to the second question stems from the fact that the analyzer does not measure plasma in the private flux regions of the inner hoops. Since this is also where a lower hybrid resonance exists, only the common flux heating will be measured by the analyzer.

To provide more information to answer the first and third questions, ion temperature profiles were taken at a density of $n=2x10^{11} cm^{-3}$ using the octupole's intermediate gun. This gun produces hotter, more collisionless plasmas with a factor of about ten fewer neutrals than the large gun. It was thought that if collisional heating or neutral ionization play a role in the anomalous edge heating at low densities, a difference in the profiles should be apparent.

The data is shown in Fig. 29. The profile after RF heating is not very different from Fig. 28, with the largest heating still leaning

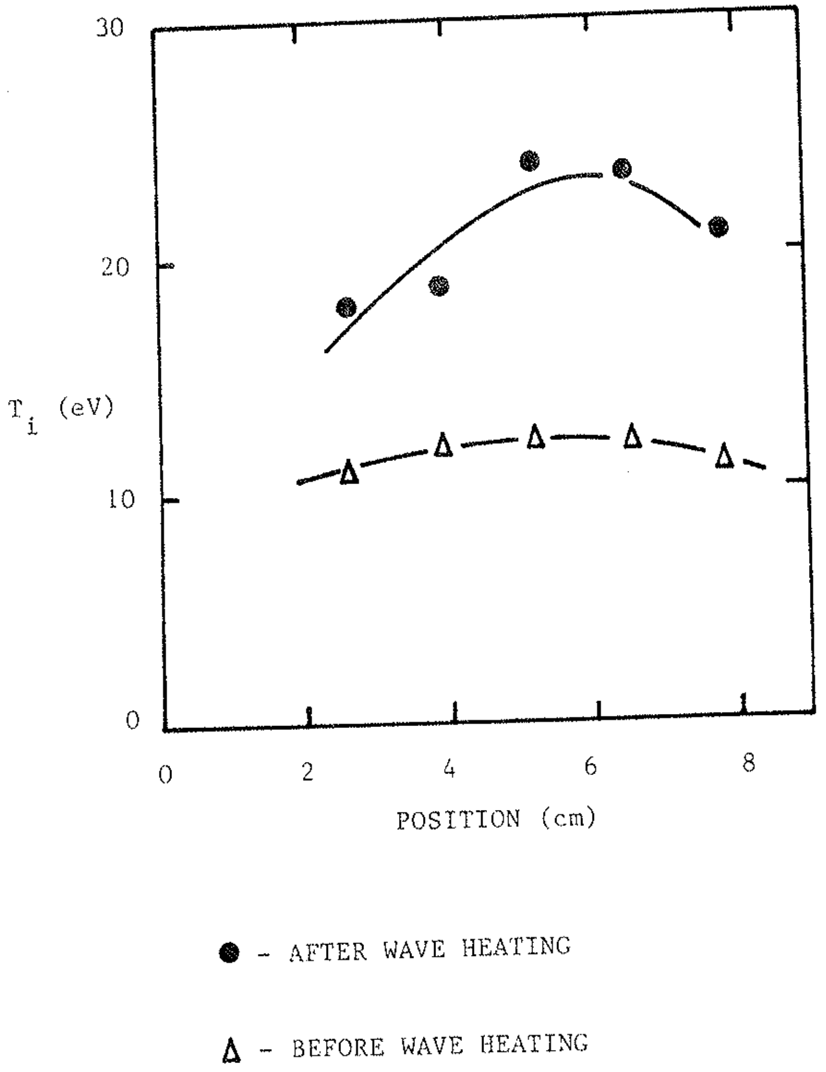

Figure 29. Ion temperature versus position across the outer bridge region measured with the perpendicular analyzer in hydrogen plasma (intermediate gun). Wave power is 20 kW and peak density is $n = 2 \times 10^{11}$ cm^{-3}.

slightly toward the outside of the plasma.

From the analysis in Chapter 2, section C, collisional heating at these temperatures could absorb no more than about 20% of the RF power. The remaining 80% should have been absorbed over a narrow region at the plasma center, producing a peak in ion temperature there. No such peak is observed in the data presented thus far.

Since the above measurements were taken only a few tens of centimeters from the antenna and in the same cross-sectional plane, it was thought that large electric fields near the antenna might play a role in the anomalies in the temperature profiles. To test this idea, measurements were taken 180 degrees around the machine.

It was found by doing this that heating at the edge was reduced considerably relative to values at the plasma center. Evidently some anomalous heating does occur very close to the antenna.

The new data shows results in clearer agreement with theory and is displayed in Fig. 30. Well defined peaks in the ion temperature develop with T_i = 39 - 17eV that are substantially above initial plasma temperatures of $T_i \lesssim 7$eV. We see that central temperatures are in line with temperatures of 40eV measured with the Fabry-Perot interferometer at twice the power level in the last section using a helium plasma. The peak temperature from the energy analyzer measurements is at the center of the density profile for peak densities of $n=3\times10^{11}cm^{-3}$ and moves toward the edge of the plasma for peak densities of $n=8\times10^{11}cm^{-3}$. The dashed line in Fig. 30 is a typical experimental density profile from which we see that, in fact, the peak in ion

Figure 30. Ion temperature profiles in hydrogen plasma. Wave power = 20kW, pulse period = 1.2ms.

a. $n = 3 \times 10^{11} cm^{-3}$, T_i = 4eV before wave heating.

b. $n = 8 \times 10^{11} cm^{-3}$, T_i = 7eV before wave heating.

Densities are peak values. The dashed line is a typical experimental density profile (normalized to peak density using the axis on the right).

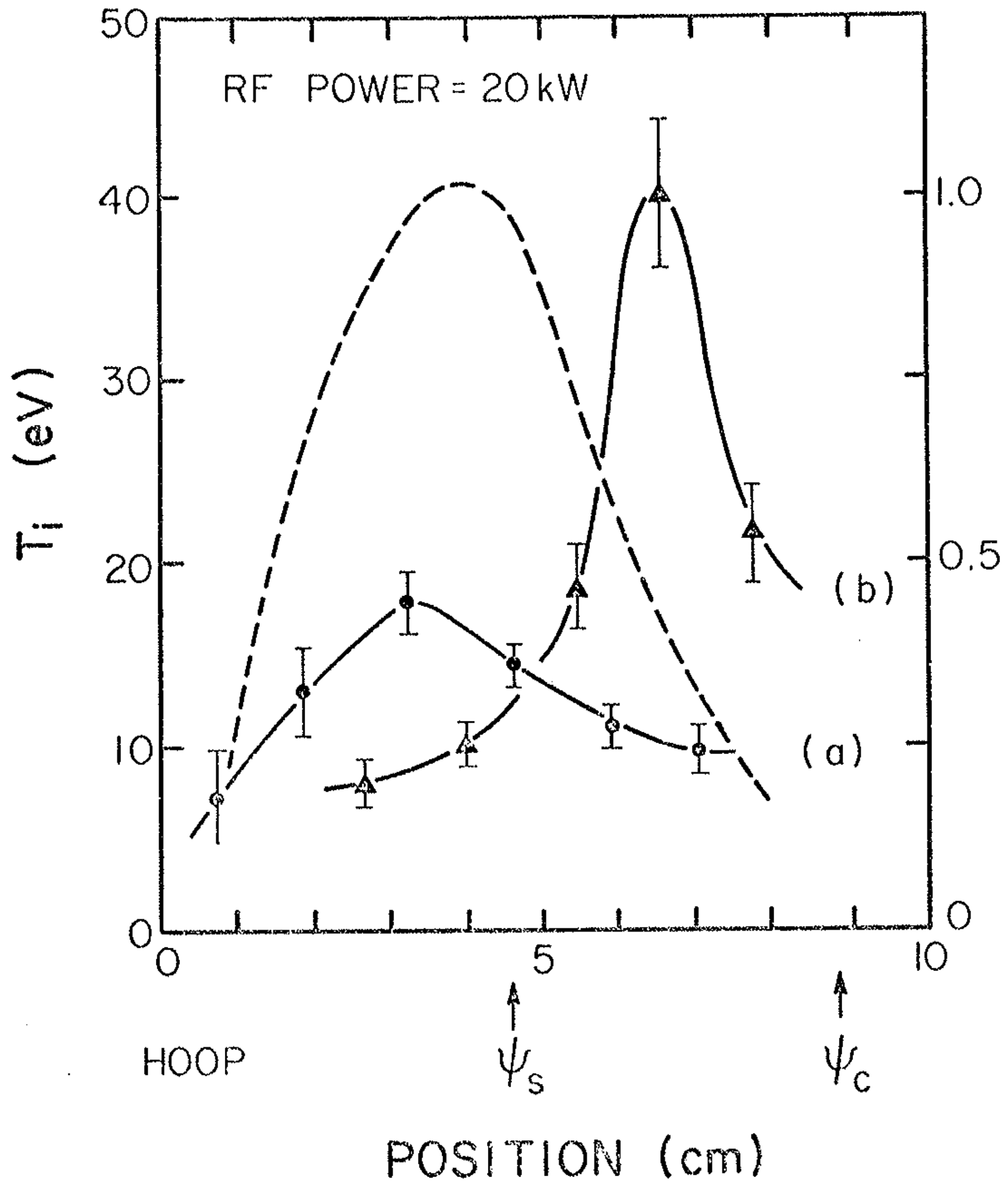
RF POWER = 20 kW
T_i (eV)
0
10
20
30
40
50
0
0.5
1.0
(a)
(b)
0
5
10
HOOP
ψ_s
ψ_c
POSITION (cm)

temperature follows the constant density surface $n=3\times10^{11}cm^{-3}$.

This is substantially below the density that is predicted from cold plasma theory ($n=7\times10^{11}cm^{-3}$) and also the value that is predicted from warm plasma theory ($n=6\times10^{11}cm^{-3}$) based upon the theoretical n_z spectrum of the antenna ($n_z\simeq4$). The next section will examine in greater detail how the heating varies with plasma parameters to provide additional insight into this anomaly.

C. Variation with Density and Magnetic Field

In Fig. 31 we have plotted $\Delta nKT_i/E$ versus density for three different magnetic field values between B = 1.4kG and B = 3.5kG. E is the RF energy input divided by the torus volume. Ion temperatures are measured on the separatrix with the perpendicular energy analyzer. Magnetic field values used are the highest fields found on the separatrix, since this is where the wave turning point will first appear in the machine as density and magnetic fields are increased.

We find that ion heating becomes effective above a specific value of density which increases with decreasing magnetic field. For magnetic field values below B = 1.4kG essentially no ion heating is obtained out to densities of $9\times10^{11}cm^{-3}$. These trends are perhaps the strongest evidence presented so far that a mode conversion process is involved in the ion heating.

To make this statement more quantitative, we plot in Fig. 32 the transition conditions where ion heating begins, obtained from Fig.31 together with additional data at B = 2.9kG. The theoretical turning point conditions derived from Eqn. (2.32) are also shown in the

Figure 31. Variation of ion heating with density for

a. $B = 3.5$kG

b. $B = 2.1$kG

c. $B = 1.4$kG .

E = (RF energy)/(octupole volume).

The density scale is labeled on curve c.

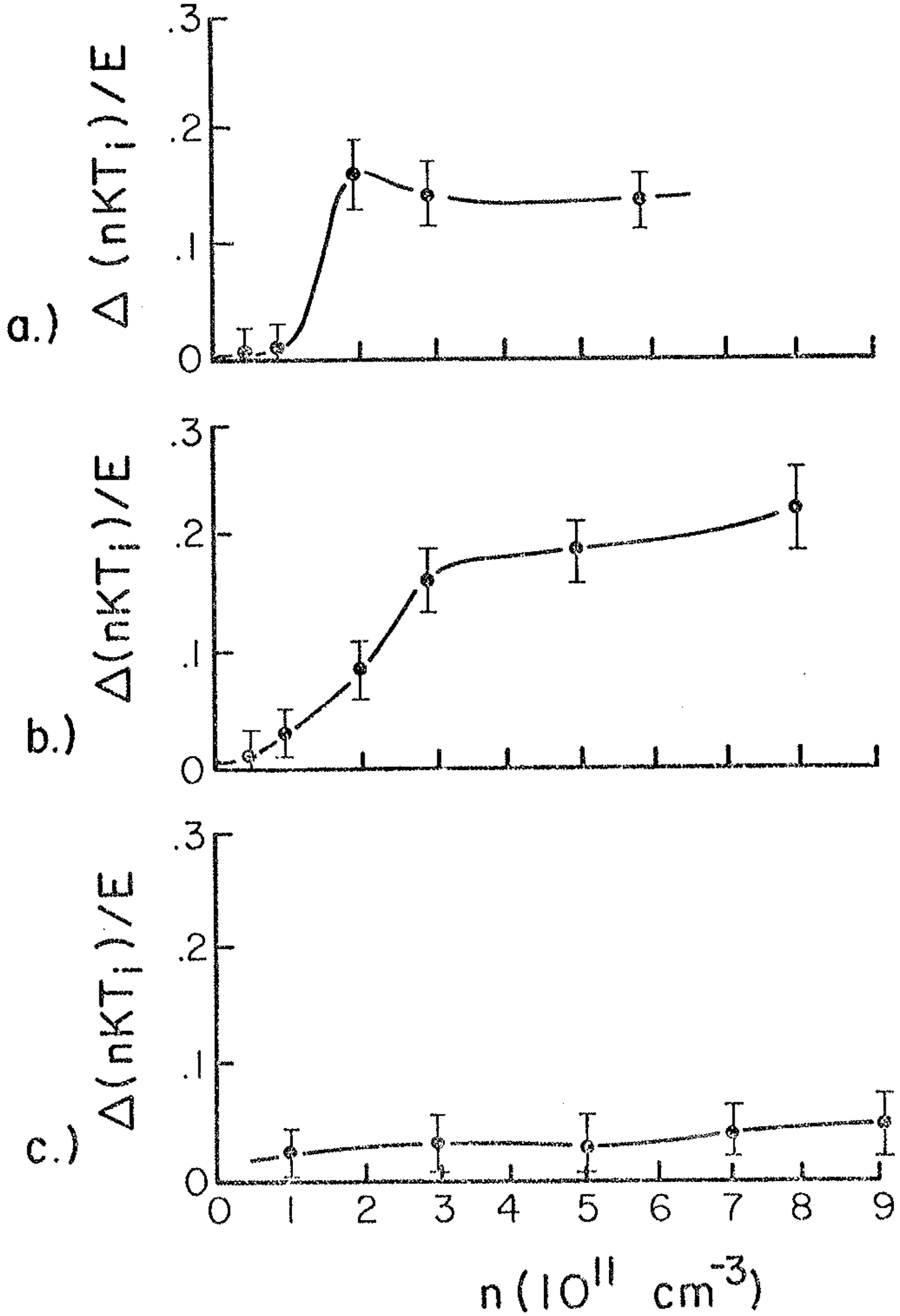
a.)
b.)
c.)
Δ (nKT$_i$)/E
Δ(nKT$_i$)/E
Δ(nKT$_i$)/E
.3
.2
.1
0
0
1
2
3
4
5
6
7
8
9
n (10^{11} cm^{-3})

Figure 32. Points represent magnetic fields and densities where ion heating first occurs as parameters are increased (from Fig. 31). Lines are theoretical turning point conditions for,

a. $\frac{k_z v_e}{\omega} = 0.02$

b. $\frac{k_z v_e}{\omega} = 0.16$

c. $\frac{k_z v_e}{\omega} = 0.3$

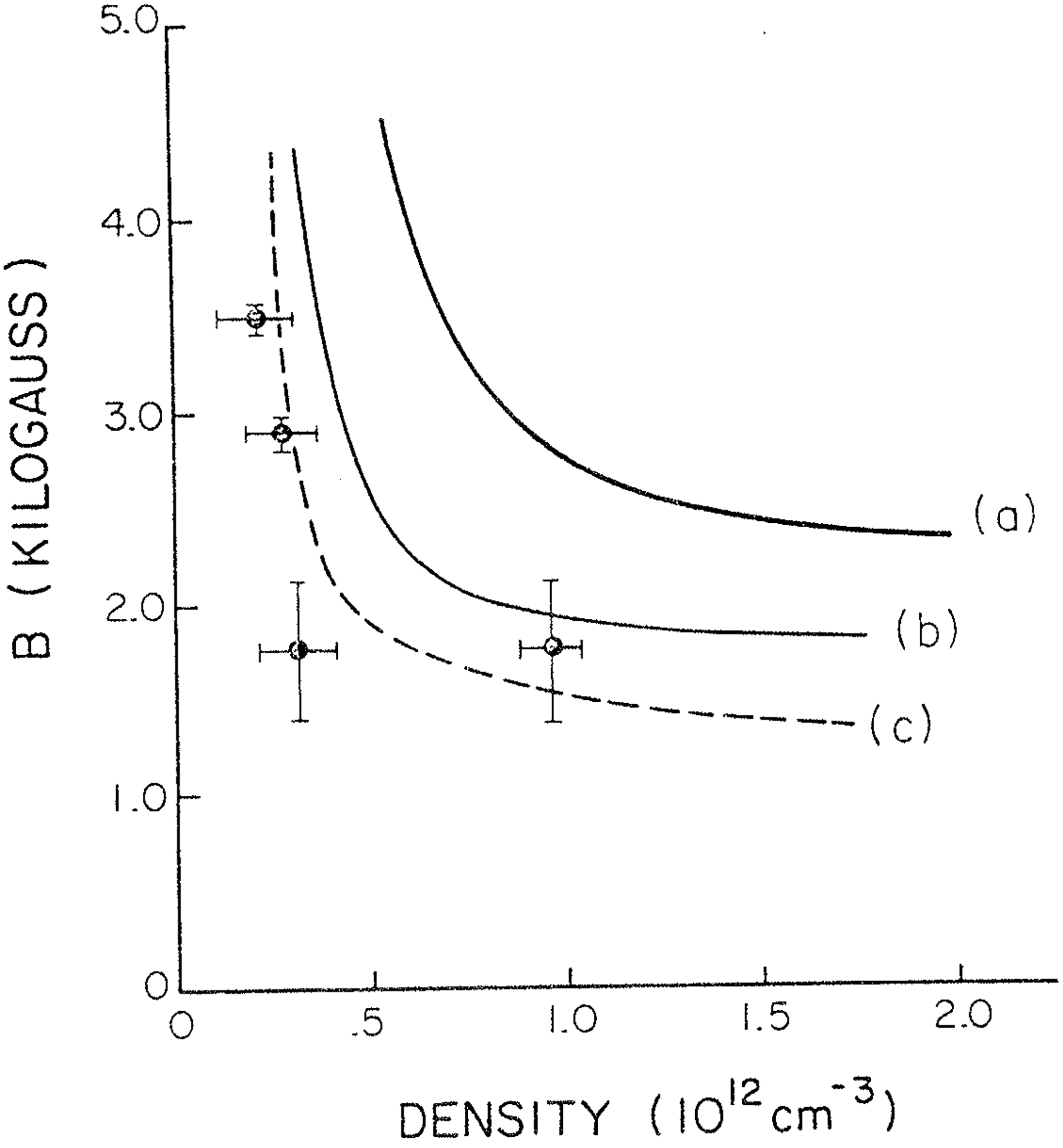
5.0
4.0
3.0
2.0
1.0
0
B (KILOGAUSS)
(a)
(b)
(c)
0
.5
1.0
1.5
2.0
DENSITY (10^{12} cm^{-3})

figure for comparison. Curve (a) ,for example, results if n_z equals the value at the antenna (n_z=4). We see that the experimental points are well below values of density and magnetic field that would result from such an n_z value. In fact, the fit with theory is good only for higher values of n_z such that $k_z v_e/\omega \simeq 0.3$. It now becomes clear that the density where energy deposition occurs in Fig. 30 of the last section ($n \simeq 3 \times 10^{11} cm^{-3}$) is very close to the turning point density for a wave having this same upshifted value for $k_z v_e/\omega$. This provides additional support to the possibility of an upshifted n_z spectrum.

If the n_z spectrum of the lower hybrid wave does shift to the higher value indicated in Fig. 32, energy in the spectrum at these values would have to be fairly substantial. This is because near the transition densities, considerable RF power is absorbed by the ions.

Interestingly, at the same time that this result was first reported, the Alcator group reported an increase in n_z from n_z=3 to n_z=5 in their lower hybrid heating experiments.[62] While this represents less than one fourth of the fractional increase in n_z found in our experiment, it yields about the same value for $k_z v_e/\omega$, due to their higher temperatures. A common mechanism producing this effect has not been identified, however.

Detailed wave measurements in Chapter 9 will support the idea that the n_z value is upshifted from its value at the plasma edge.

D. Power Dependence

The theory that is purported to explain results in the previous sections is a linear one. As such, one would expect heating to occur for all power levels no matter how small. This, unfortunately is not always the case.

Fig. 33 shows the increase in nKT_i versus RF power level for an initial density of $n = 2 \times 10^{11} cm^{-3}$. A clear threshold power level of 5kW must be exceeded before any ion heating is observed. The plasma density remained constant below 10kW, so the threshold has nothing to do with density changes.

The saturation in the heating at power levels exceeding 30kW may be partly due to increased impurity influx from the antenna. It has not been studied in any detail, however, and is not relevant in the present discussion.

The threshold behavior in Fig 33 suggests that a non-linear effect occurs somewhere between the antenna and the lower hybrid resonance. Because the results in the last two sections can be explained by a linear model at the resonance, it is possible that the non-linear response is formed at the plasma edge near the antenna.

Additional credence is lent to this idea by the fact that wave fields and wave energy per particle are largest near the antenna (measurements indicate at least a factor of six larger). In addition, non-linear response near the antenna with linear response near the resonance have been shown to be a possibility from a theoretical standpoint.[8] Finally, we know that something unusual is occurring at the antenna because of the anomalous heating near the antenna reported in section B.2 of this chapter. This complex question cannot be conclusively resolved in this thesis, unfortunately.

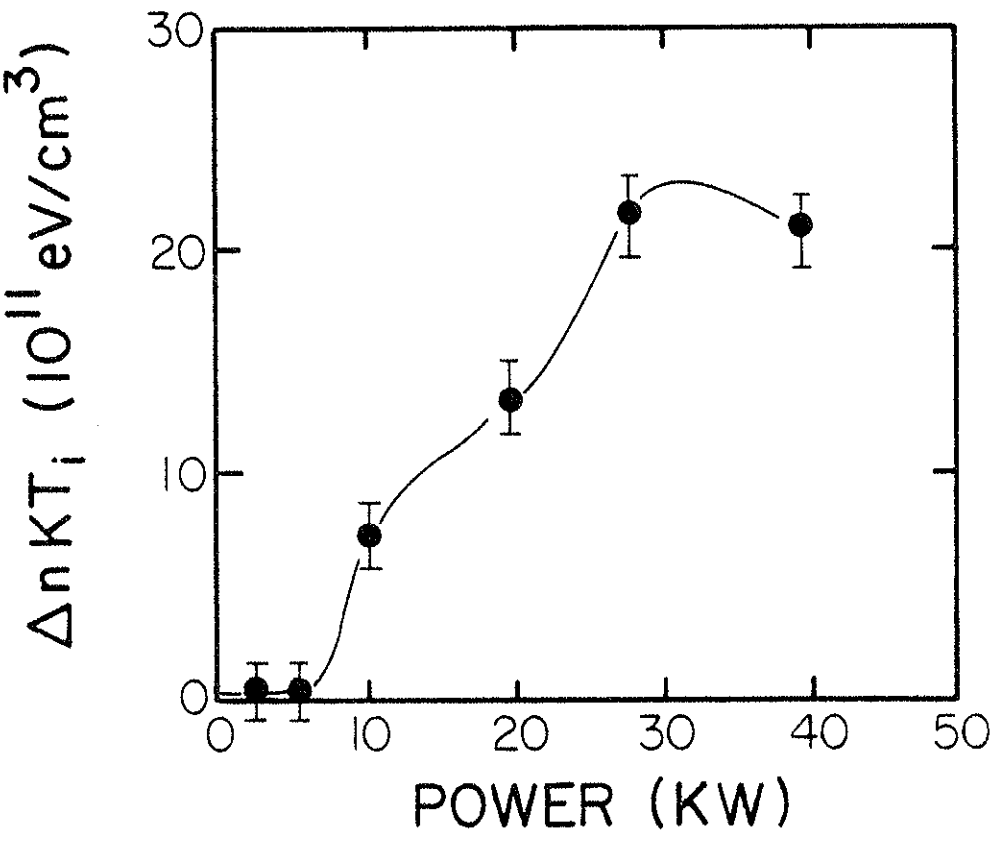

Figure 33. ΔnKT_i versus wave power. Initially, $n = 2 \times 10^{11} cm^{-3}$ for hydrogen plasma.

E. Heating Efficiency

Accurate determination of the ion heating efficiency requires a knowledge of all possible energy flow channels during RF heating. Possible loss channels include such things as particle and energy transport and radiation. Without explicitly identifying these channels we will obtain an estimate of the ion heating efficiency, ε_i, from,

$$\varepsilon_i = \frac{3}{2}\frac{1}{P\Delta t}\int_V \Delta(nKT_i)\, dV + \frac{Q_i}{P} \qquad (5.2)$$

where P is the RF input power, Δt is the RF pulse duration, Q_i is the rate of ion energy loss, ΔnKT_i is the increase in plasma energy density at the end of the wave pulse, and the integral is taken over the octupole volume. A lower bound on the efficiency will be found by taking Q_i equal to the measured rate of decrease of plasma energy just before wave heating. An upper bound will be estimated by taking Q_i equal to the measured rate of energy decrease immediately after wave power is turned off.

The volume integral can be calculated from the temperature and density profiles in Fig. 30 and a knowledge of $\partial\Omega/\partial x$, where Ω is the volume of a magnetic flux tube and x is the distance across the bridge region where the profiles in Fig. 30 were taken. Practical values of $\partial\Omega/\partial x$ are estimated from planometer measurements of computer flux plots of the octupole and are shown in Fig. 34. This curve is first multiplied with the experimental temperature profiles. The resulting curve is then multiplied with the density profile. Finally, the

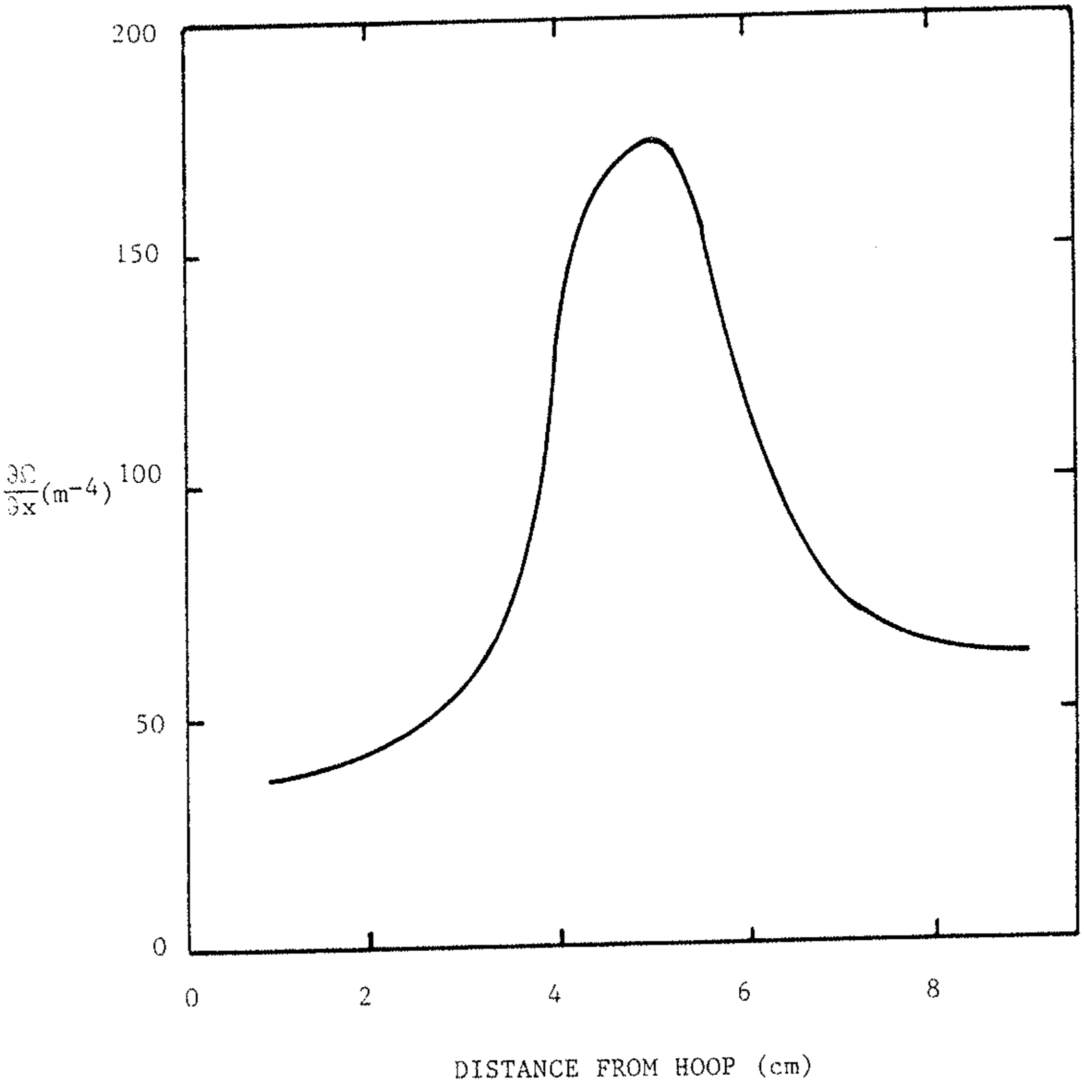

Figure 34. $\partial\Omega/\partial x$ versus distance from the hoop across the outer bridge region. Ω is the volume of a flux tube.

integrated area under this last curve is taken to determine the total ion energy increase.

Based upon this procedure, for a 1.2ms, 20kW wave pulse, the efficiency is $25\% > \varepsilon > 15\%$ when the peak density is $n=3\times10^{11}\mathrm{cm}^{-3}$ (Fig. 30a) and $50\% > \varepsilon > 30\%$ when the peak density is $n=8\times10^{11}\mathrm{cm}^{-3}$ (Fig. 30b). It should be noted that the factor 3/2 in Eqn. (5.2) occurs for an isotropic velocity distribution whereas the measurements in Fig. 30 provide only perpendicular temperatures. Earlier parallel energy analyzer measurements show temperature increases close to those in Fig. 30, indicative of velocity isotropy, thereby justifying the 3/2 factor.

Additional contributions to the efficiency will be provided by electron heating described in the next chapter.

CHAPTER 6

ELECTRON HEATING

As discussed in Chapter 5, sections B and C, the variation in ion heating with density and magnetic field and the location of the heating zone along the density profile suggest that the n_z spectrum of the wave undergoes a substantial upshift. For values of n_z such that $k_z v_e/\omega \simeq 0.3$, as indicated in Fig. 32, considerable electron Landau damping should occur with associated electron heating.

In fact, electron heating is observed with $\Delta T_e \geq 7\text{eV}$ at $n = 3 \times 10^{11}\text{cm}^{-3}$ for 20kW of input RF power. This lends further support to the possibility of a k_z upshift. Electron temperature versus time is plotted in Fig. 35 based upon Langmuir probe measurements. Temperature decay times are on the order of 1-2ms after wave heating.

In determining the temperatures in Fig. 35 the entire probe characteristic is plotted for each point, and standard analysis is used.[47,63] A sample probe characteristic after wave heating is plotted in Fig. 36. The portion of the characteristic between ion and electron current saturation is exponential over at least an order of magnitude Occasionally, a high energy tail is observed on the characteristic just as was the case for the ion distribution. The tails are generally more apparent near the edge of the plasma and last for less than 100μs.

From Chapter 2, we found that if ordinary Landau damping is occurring, it should be strongest near the edge of the plasma.

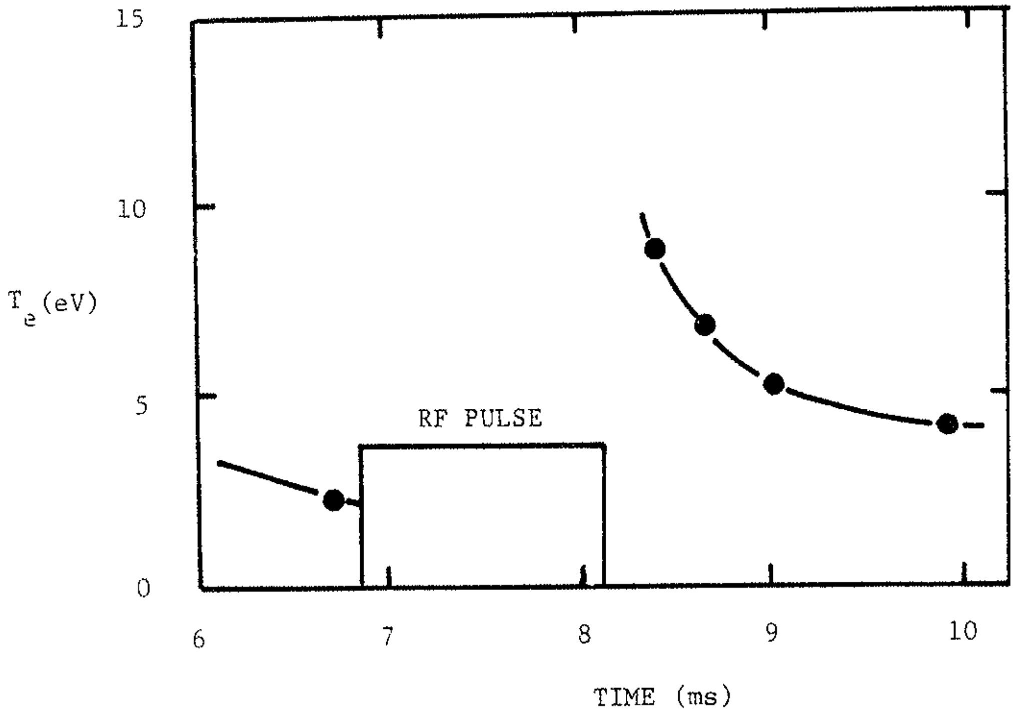

Figure 35. Electron temperature versus time after plasma injection. Wave power = 20kW, $n = 3 \times 10^{11} cm^{-3}$.

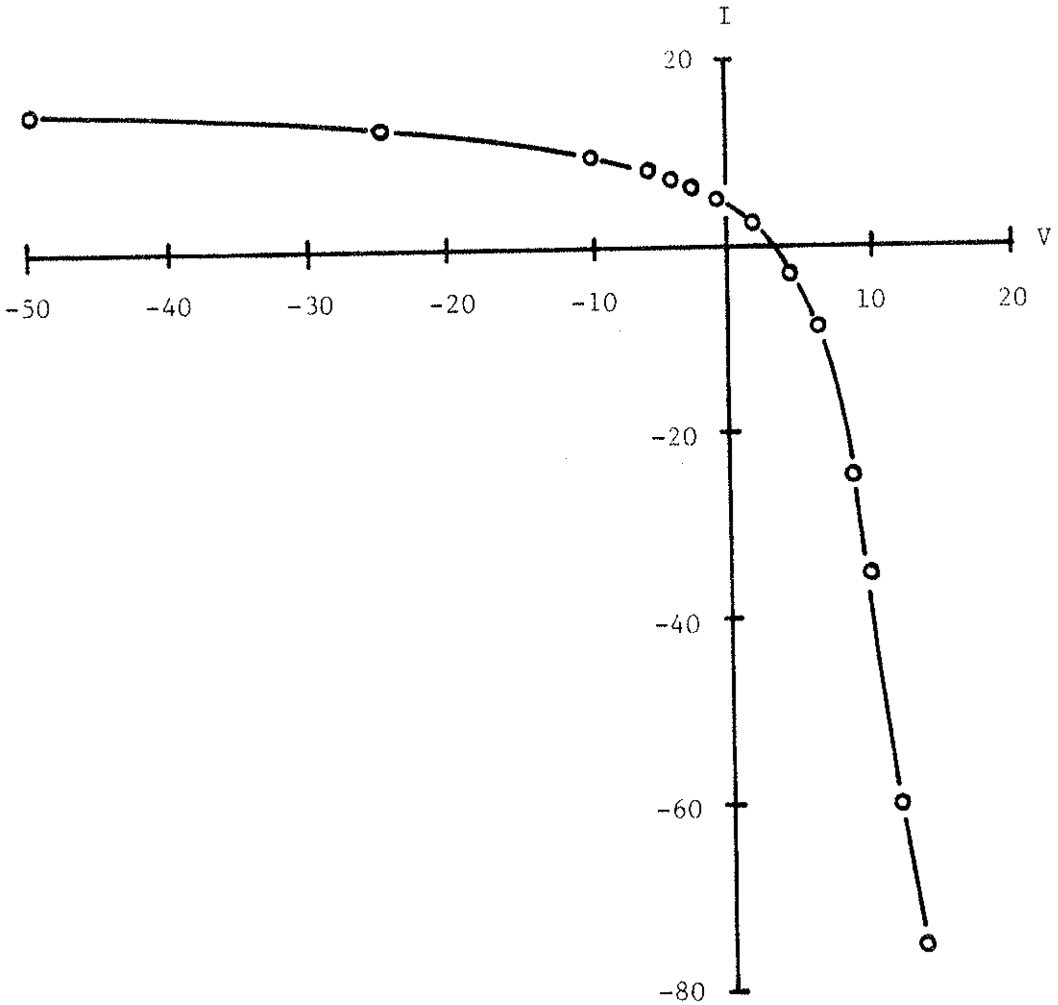

Figure 36. Sample Langmuir probe characteristic after wave heating.

This has been observed in mirror machine experiments.[10,27] To test this possibility on the octupole the electron temperature profile after RF heating was taken using Langmuir probes and is shown in Fig. 37 for a density of $n = 3 \times 10^{11} cm^{-3}$. The entire probe characteristic was plotted for each point, once again.

Surprisingly, the electron temperature is nearly uniform 150 μs after the RF. Uniform electron temperature after lower hybrid heating was also observed on the FM-1 Spherator.[20] A broad electron temperature profile can be expected in the present case if the cross field electron thermal transport occurs on a time scale faster than 150 μs. The electron temperature profile would then have time to spread before the measurement in Fig. 37 could be taken. Detailed calculations of transport ratesare needed to determine if this is a possibility.

Measurements during wave heating would provide a better indication of local energy deposition to the electrons if it occurs. This measurement was not possible in this experiment because of RF interference on the diagnostic during wave heating. The profile can still be broad in this case if the local heating rate is less than the thermal transport rate.[64].

Figure 37. Electron temperature profiles.

$n = 3 \times 10^{11} cm^{-3}$, wave power = 10kW.

a. Before wave heating

b. 150μs after the end of the RF pulse.

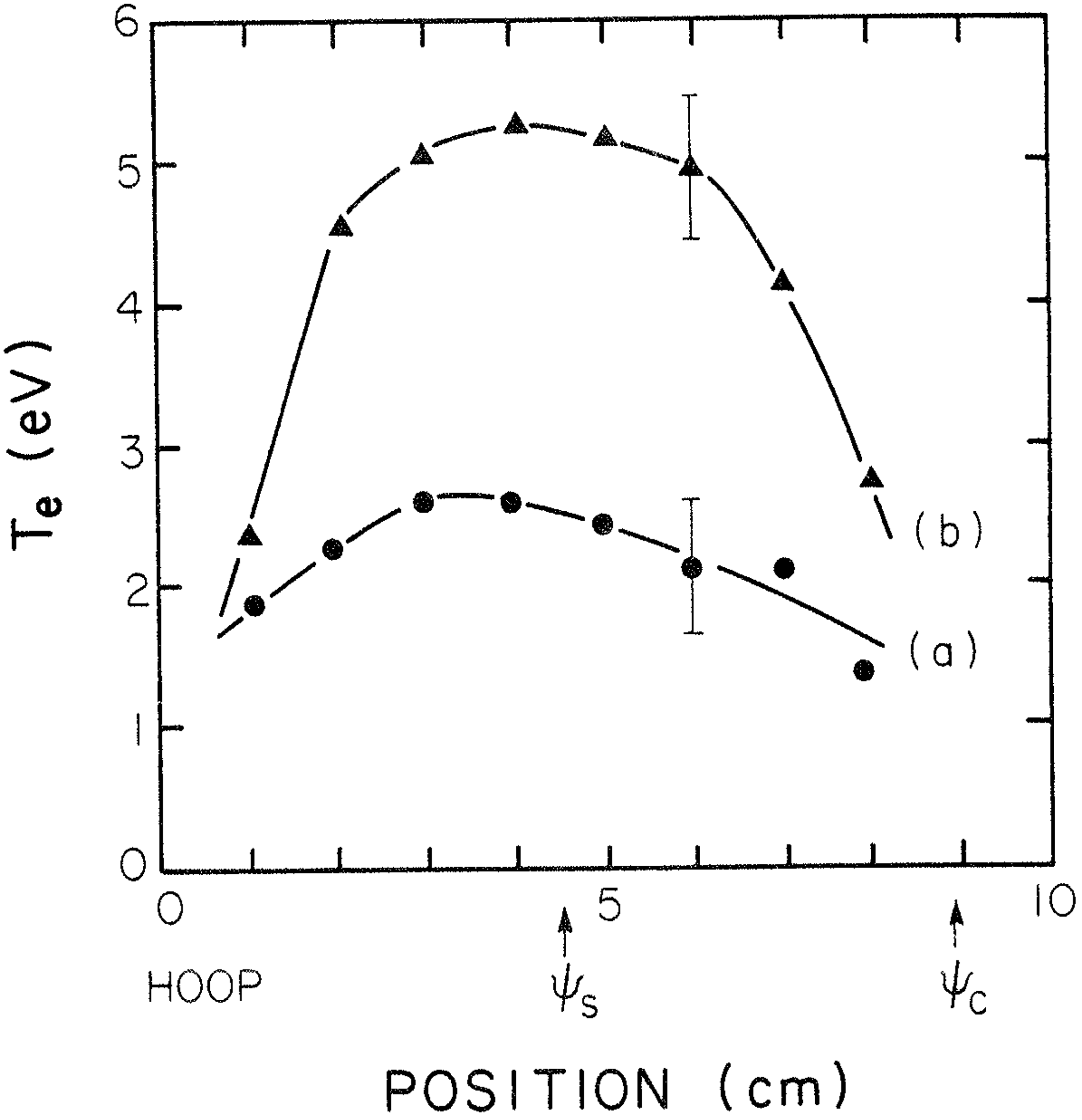
T_e (eV)
0
1
2
3
4
5
6
(b)
(a)
0
5
10
HOOP
ψ_s
ψ_c
POSITION (cm)

CHAPTER 7

EFFECTS OF HEATING ON PARTICLE CONTAINMENT

Considering the magnitude of the perturbation of the ion and electron temperatures from RF heating described in Chapters 5 and 6 ($\Delta T_i/T_i \gtrsim 3$ and $\Delta T_e/T_e \geq 2$) it is not difficult to imagine that plasma stability and confinement will also be affected. In fact, the effect on the octupole is considerable.

In Fig. 38 are photos of typical microwave interferometer traces with and without RF heating. For the samples shown, the peak density before RF heating is $n = 1.8 \times 10^{12} cm^{-3}$ which is well above the density at which lower hybrid wave energy is deposited. Ion heating at the edge of the density profile, similar to Fig. 30b, is initially occurring as we know from energy analyzer scans. The rate of density decay increases sharply when RF power is applied as evidenced by rapid interferometer phase shifts. This behavior is apparently associated with the edge heating.

The data displayed in Fig. 39 makes this clear. The density decay measured on the interferometer is plotted versus time after gun injection for four different initial densities between $n = 1.5 \times 10^{12} cm^{-3}$ and $n = 5 \times 10^{11} cm^{-3}$. RF power levels are 15kW with pulse periods of 10ms. We find in all cases that the density decays rapidly in 1-2ms after RF heating until $n = 3 \times 10^{11} cm^{-3}$. The density is then held constant at this value for the duration of the wave pulse.

Note that this is the density at which wave energy is deposited at the peak in the density profile near the separatrix, as we found in

Figure 38. Fringe shift on the microwave interferometer and ion saturation current versus time after plasma injection.

Upper photo: No wave heating.

Lower photo: 20kW of wave heating applied 1ms after plasma injection.

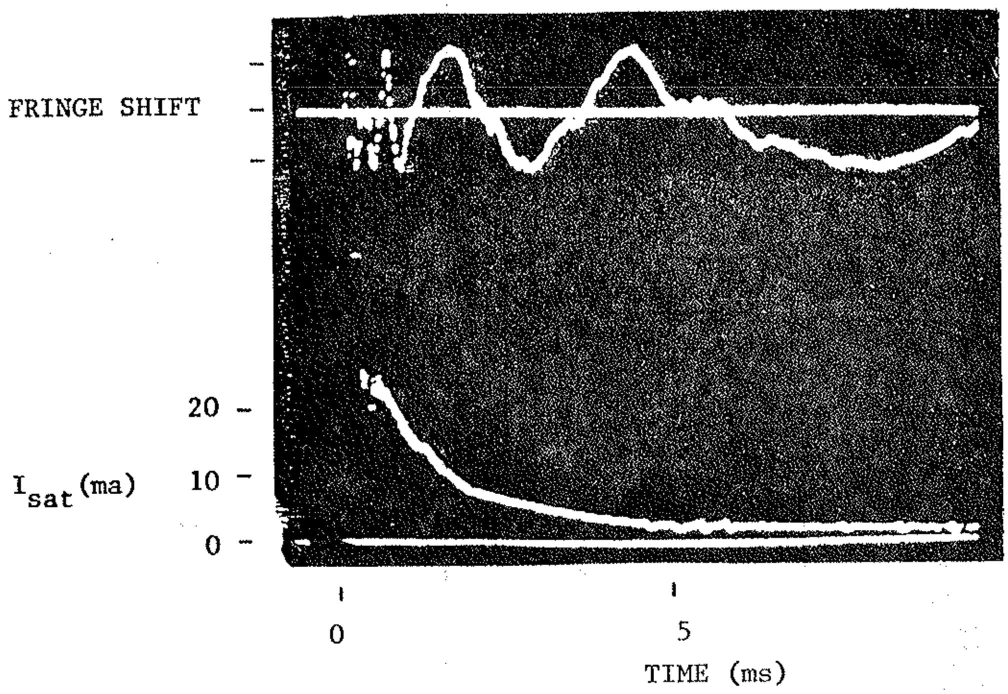
FRINGE SHIFT
20
I_{sat} (ma)
10
0
0
5
TIME (ms)

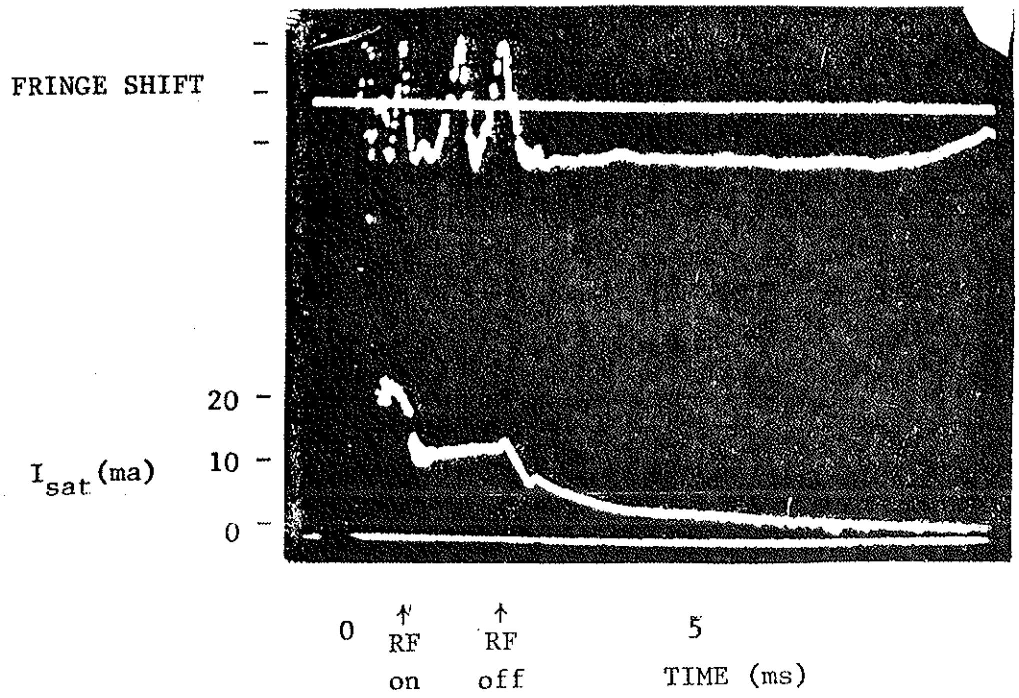
FRINGE SHIFT
20
I_{sat} (ma)
10
0
0
RF on
RF off
5
TIME (ms)

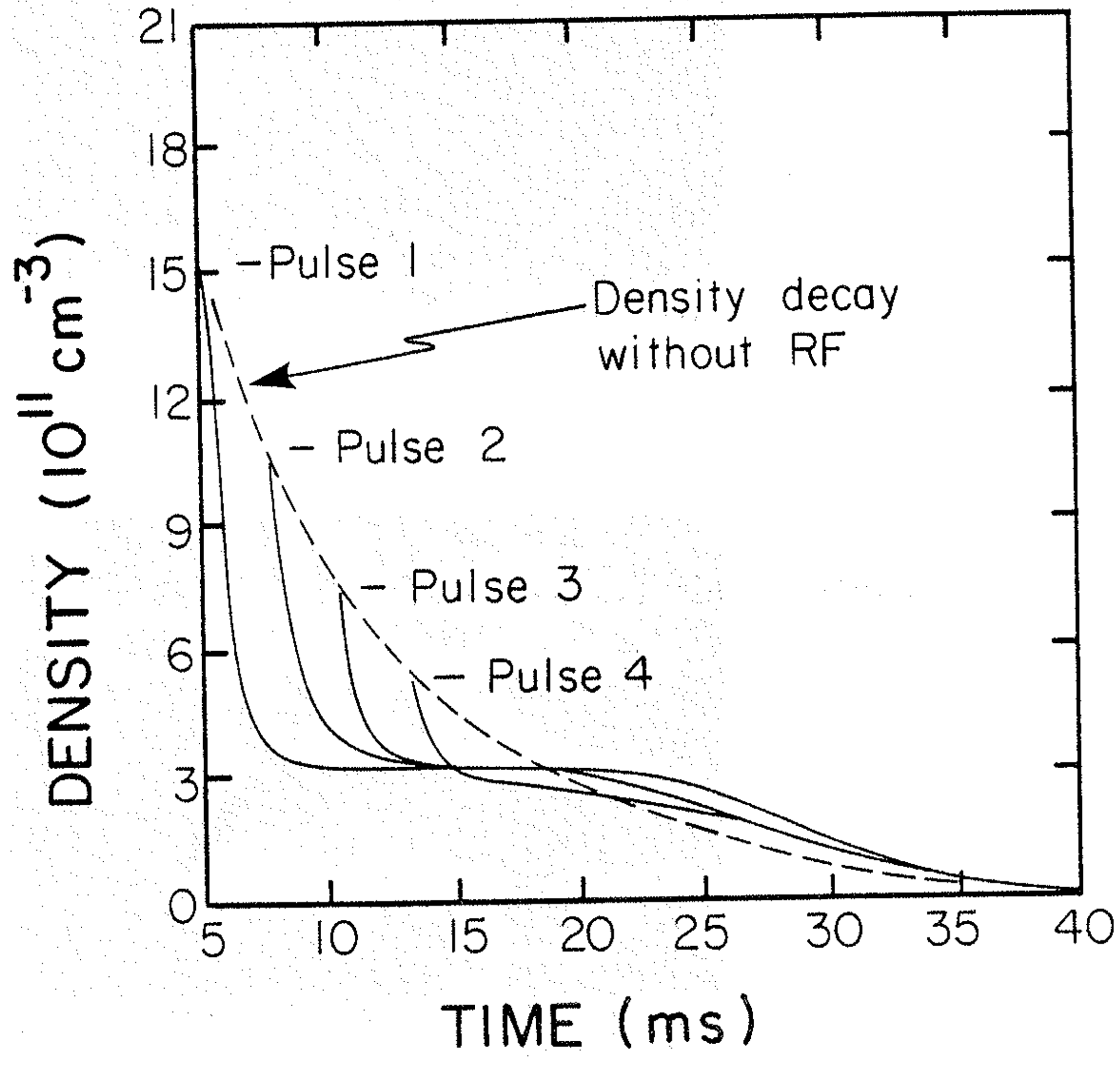

Figure 39. Density decay from wave heating for RF pulses injected into four different initial densities. Wave power = 15kW, pulse period = 10ms.

Fig. 30a. Apparently, the edge heating at higher densities is an unstable situation, while heating on the separatrix is stable. The stability at $n = 3 \times 10^{11} cm^{-3}$ confirms the strong wave-particle interaction at this density that was found in Chapter 5 for comparable wave power levels.

It should be noted from this result that, while the edge heated plasma in Fig. 30b absorbed wave power more efficiently, it was unstable and poorly confined. Temperature decay times were on the order of a few hundred microseconds which is shorter than loss times for charge exchange under the conditions of the measurement. Therefore the reduced heating at $n = 3 \times 10^{11} cm^{-3}$ in Fig. 30a is really better.in the sense that it is stable with temperature decay times on the order of 1-2ms based upon energy analyzer measurements.

CHAPTER 8

LOWER HYBRID WAVE FIELDS

The following wave measurements reveal a number of complexities in the physics of lower hybrid wave heating. In section C of this chapter wavelength measurements support the earlier idea that the k_z wave power spectrum shifts to higher values. In addition,they show that this upshift occurs near the wave turning point. However, section A reveals that a dominant fast mode is excited through some unknown process. Observation of the slow mode is obscured by its presence. Finally, section B show that parametric instabilities are present but they do not appear to play an important role in heating.

A. Spacial Profiles

Wave potentials are measured with a coaxially shielded probe having a small (0.5 mm), flat, insulated copper disk at the tip of the probe which couples capacitively to the plasma. The signal passes through a high pass filter (f_c = 100MHz) to either a Tektronics 7704 high speed scope terminated in 50 Ohms, or a Hewlett Packard 8551B spectrum analyzer fix-tuned to 140 MHz with a 500 kHz bandwidth. Both signal monitors give the same potential profiles.

Sample profiles are shown in Fig. 40 for densities between $n = 6 \times 10^{11} cm^{-3}$ and $2.4 \times 10^{12} cm^{-3}$. Measurements are taken in the upper inner hoop region near the lower hybrid resonant surfaces. Surprisingly, we find that the wave fields propagate everywhere across the density profile even for the highest density shown. Theory says that

Figure 40. Capacitive RF probe voltage, V_p (arbitrary units) versus position near the upper inner hoop.

a. $n = 6 \times 10^{11}\text{cm}^{-3}$

b. $n = 1.2 \times 10^{12}\text{cm}^{-3}$

c. $n = 2.4 \times 10^{12}\text{cm}^{-3}$

Actual electric field values are found from,

$$|E|^2 \simeq K(R^2 + \frac{1}{\omega^2 C_p^2})V_p^2$$

where $R = 50\Omega$, K is a constant, and C_p is the probe capacitance in the presence of plasma, which decreases with density. A typical experimental density profile near the inner hoop is shown by the dashed line in (a).

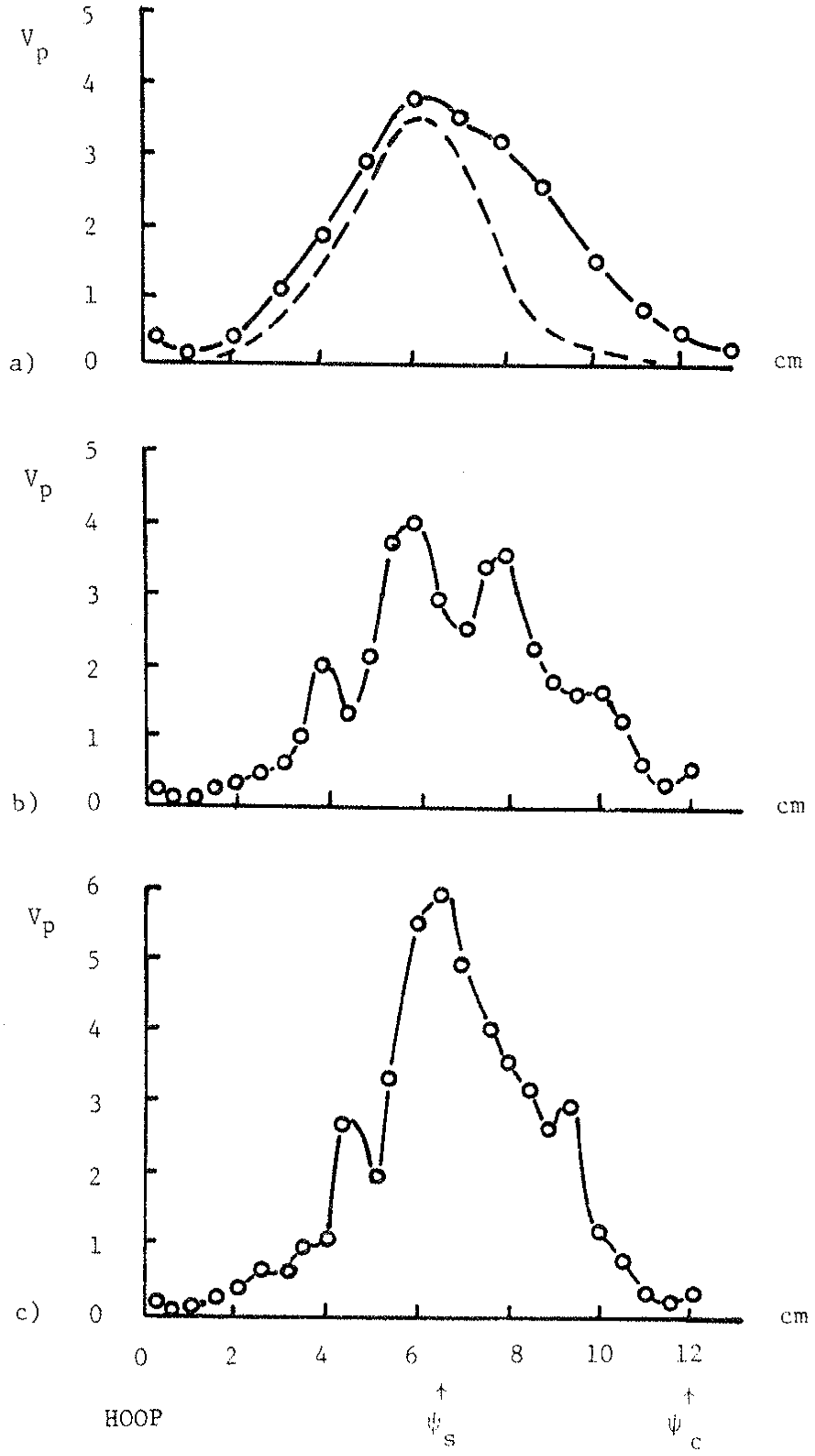
V$_p$
5
4
3
2
1
0
a)
cm
V$_p$
5
4
3
2
1
0
b)
cm
V$_p$
6
5
4
3
2
1
0
c)
cm
0
2
4
6
8
10
12
HOOP
↑
ψ_s
↑
ψ_c

the lower hybrid slow mode should have been absorbed near the edge of the density profile for these high densities.

In addition, for densities above $n = 6 \times 10^{11}$ cm^{-3}, a structure to the wave pattern develops that looks much like a standing wave. In fact, careful examination of wave patterns (b) and (c) reveals that the peaks in (c) are closely coincident with the valleys of (b) as if the mode pattern changes from an odd mode to an even mode as density decreases. The photo in Fig. 41 supports this possibility. In this photo, field amplitude is measured as a function of time, as density decays. We find that field amplitudes are large for densities at which patterns (b) and (c) exist but drop significantly for densities between these values. This drop is consistent with standing wave fields undergoing a transition between odd and even eigenmodes. Finally, spatial scans using a pair of subtracting probes placed 1 cm apart (described in section C) reveal that the phase between adjacent peaks is 180 degrees, consistent with a standing wave.

The first thing to note about this behavior is that absorption for this mode must be rather weak since standing waves are generally associated with high Q situations. The other observation is that the wavelengths indicated by the patterns are a few centimeters which is much longer than slow mode wavelengths even at lower densities. The wavelengths are, however, on the order of fast branch lower hybrid wavelengths.

From Eqn. (2.3c) we can approximate n_x^2 for the fast wave branch at these high densities $(\omega_{pe} \simeq \omega_{ce})$ using,

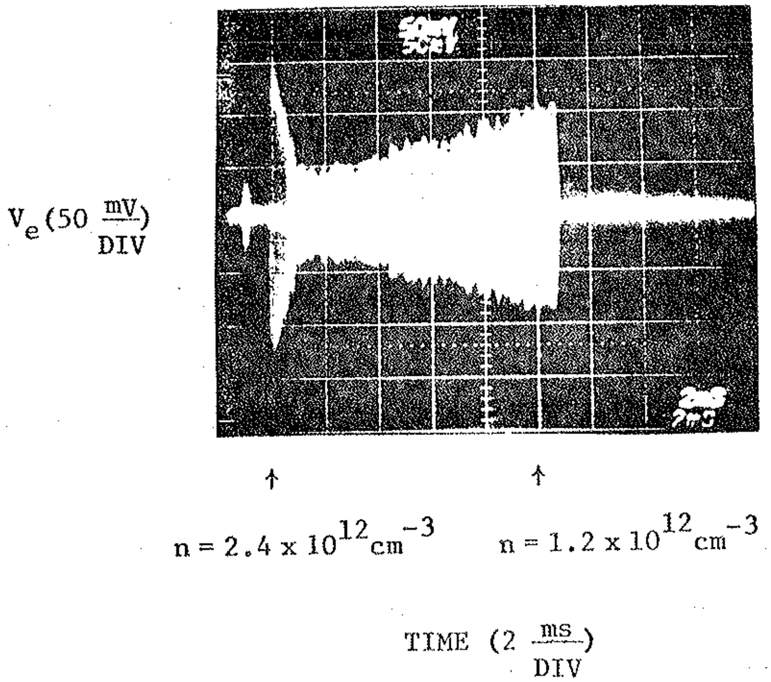

Figure 41. RF probe voltage versus time. Wave power = 10kW, initial density is $n = 2.4 \times 10^{12} cm^{-3}$ and density after wave turn off is $n = 1.2 \times 10^{12} cm^{-3}$. Probe is placed on the separatrix near the upper inner hoop.

$$n_x^2 \simeq -\frac{c}{b} = \frac{K_{xz}^2 - (n_z^2 - K_{xx})^2}{n_z^2 - K_{xx} + \frac{K_{xz}^2}{K_{zz}}} \,. \qquad (8.1)$$

Taking pattern (b) as an example, with $\lambda_x \simeq 3.5$ cm. $B = 2.5$kG and $n = 1.2 \times 10^{12}\mathrm{cm}^{-3}$, we find that $n_z \simeq 0.5$ must be imposed to satisfy Eqn. (8.1). Curiously, at this value of n_z cold plasma theory predicts that the slow mode branch of the dispersion relation joins to the fast mode branch at the plasma edge. However it is not known how the wave can propagate to the plasma interior since it must pass through an evanescent region just beyond the thin propagating region at the plasma edge. A similar mode was observed on the FM-1 Spherator experiment which also dominated wave fields and was identified with the fast lower hybrid wave.[20] More will be said about this mode in section C.

B. Parametric Instabilities

As mentioned in the introduction, parametric instabilities have been correlated with ion heating on the ATC experiment[16] and are seen in almost every high power experiment.[14-18]

Parametric instabilities are also observed in this experiment with representative spectra shown in Fig. 42. A lower sideband and an associated low frequency spectrum are observed, characteristic of parametric modes. Anomalous peaks in the spectra occur at frequencies of 90MHz and 100MHz.

It is observed, however, that the sidebands are more than 30dB down from the main pump signal. In addition, the total area under the sidebands is only about 0.01 times the area under the main pump signal.

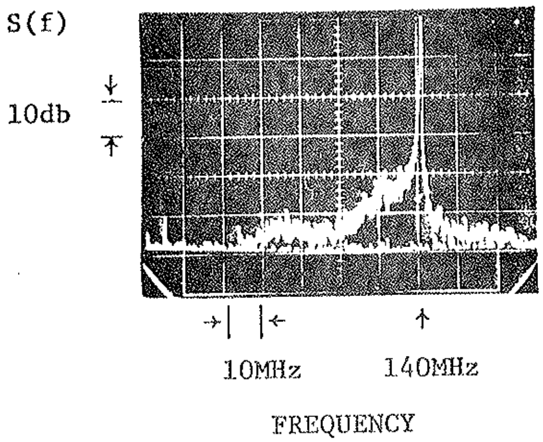

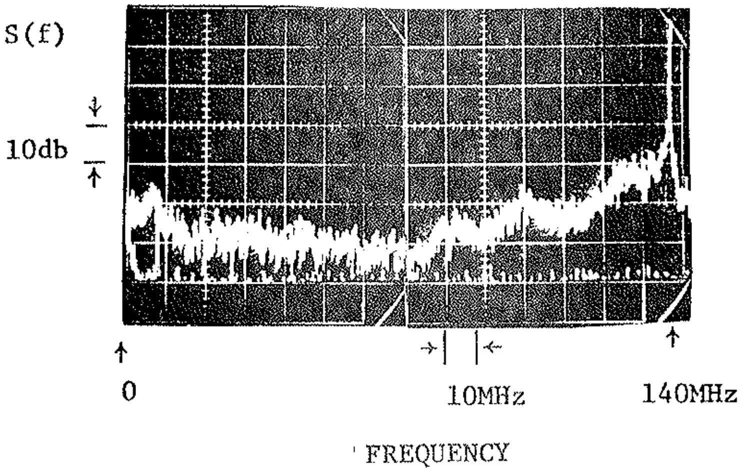

Figure 42. Wave power per unit frequency, S(f), versus frequency measured near the upper inner hoop separatrix. Wave power = 20kW, $n = 4 \times 10^{11} \text{cm}^{-3}$ (lower traces use higher gain on spectrum analyzer).

It is difficult to imagine how such small signals could have much of an effect on plasma heating.

Spacial scans of sideband and low frequency amplitude show no significant changes relative to the pump wave. This indicates that the small amplitude of the sidebands cannot be due to strong absorption by ions since we know from Chapter 5 that ions are heated locally. This would cause a rapid drop in sideband amplitude near the heating zone, which was not observed.

Further arguments against heating by parametric instabilities stems from the fact that the sidebands saturate with increased pump power levels above 20kW, while ion heating continues to increase. The data is shown in Fig. 43 which should be compared to Fig. 33 from Chapter 5. (Note also that clear thresholds occur in sideband amplitudes as power is increased, another indication that these are parametric modes). We must conclude that these modes are not responsible for the observed heating.

C. Slow Mode Wavelengths

The heating behavior presented in Chapters 5, 6 and 7 as well as the coupling behavior in Chapter 4 point strongly to heating by means of the slow lower hybrid mode rather than the fast mode. This is why the wave results in section A of this chapter were so puzzling.

A possibility for this unexpected behavior was that the slow mode could still be present in the machine, but was simply swamped out by the weakly damped fast mode. The arrangement shown in Fig. 44 was constructed to test this idea. Signals from two identical RF probes, spaced 1 cm apart, first pass through a high frequency wideband balun

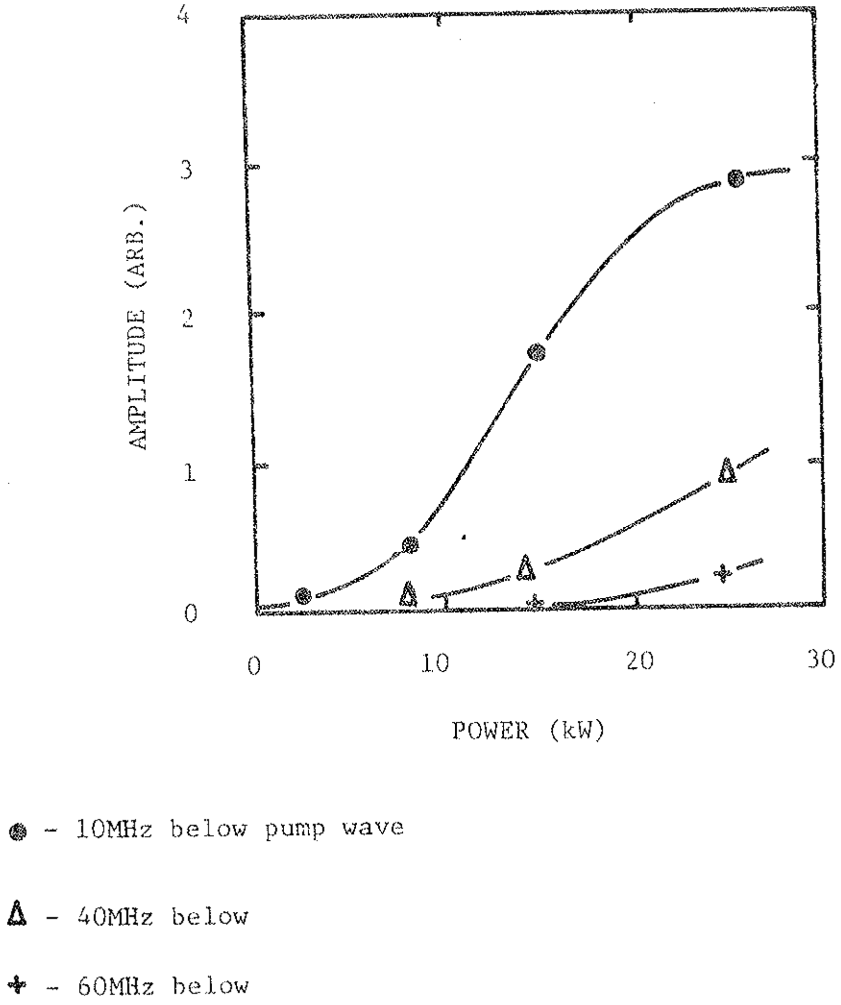

Figure 43. Amplitude of lower sideband parametric instability versus pump power for sideband peaks at 130, 100 and 80MHz.

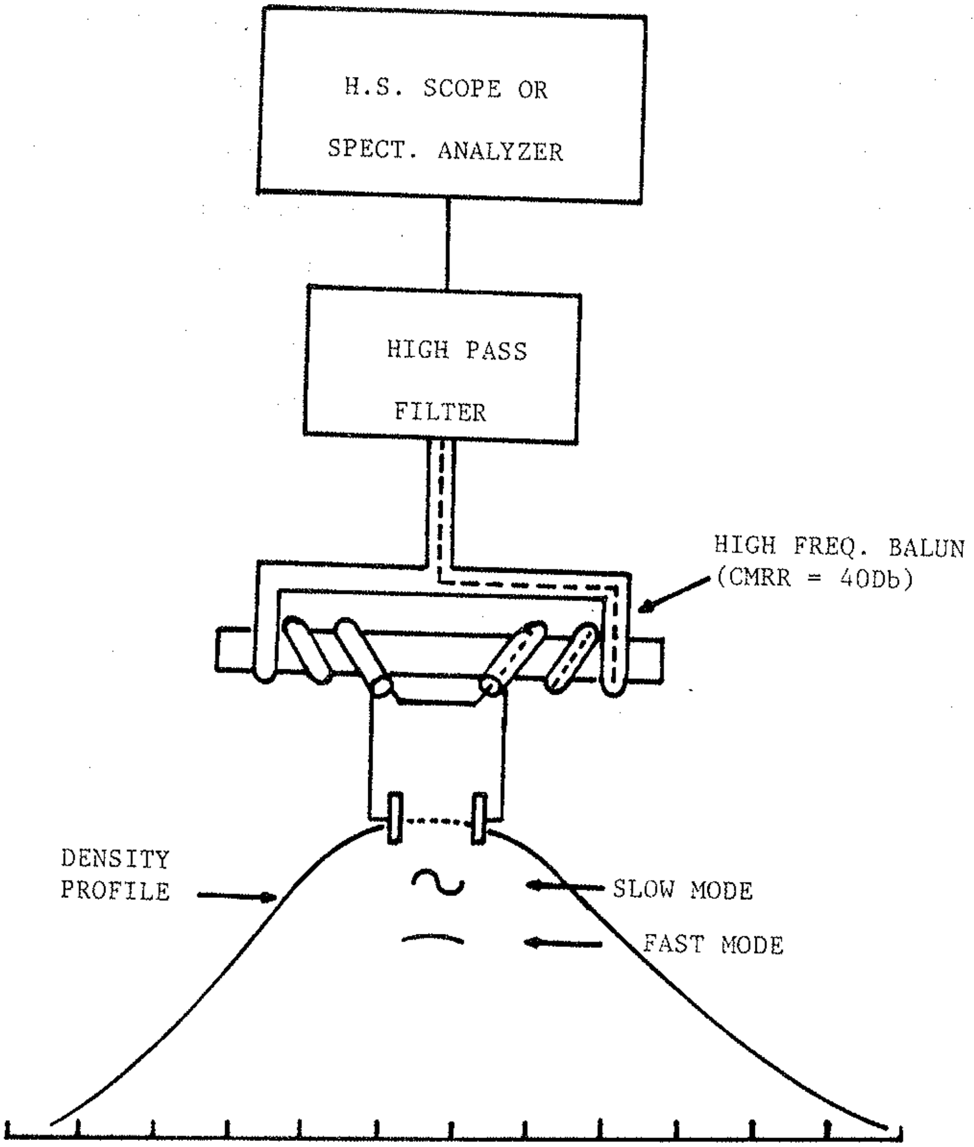
H.S. SCOPE OR
SPECT. ANALYZER
HIGH PASS
FILTER
HIGH FREQ. BALUN
(CMRR = 40Db)
DENSITY
PROFILE
SLOW MODE
FAST MODE

Figure 44. Subtracting probe arrangement for measuring short wavelength slow lower hybrid mode.

and then through a high pass filter to the high speed scope or the fix tuned spectrum analyzer. The output signal will then be proportional to the potential difference between the two probe tips. The common-mode rejection ratio through the balun was 40 db at 140 MHz. The long wavelength fast mode will produce no output signal, while the short wavelength slow mode ($\lambda << 1$ cm) will produce a difference signal between the tips. By allowing the density to decay from some high value such that $\omega \lesssim \omega_{pi}$, the signal should go through maxima and minima as the wavelength between the tips (and thus the relative phase) changes. The entire dispersion relation could conceivably be obtained from one shot in this way.

In practice, the experiment worked better than imagined. Fig. 45 shows typical output signals. The upper two traces are the signals to each individual probe tip, while the lower trace shows the difference signal as the plasma decays from $n \simeq 4 \times 10^{11} cm^{-3}$ to $n \simeq 2.5 \times 10^{11} cm^{-3}$. A phase shifting pattern, much like an interferometer trace, is observed just as expected. The amplitude of the peaks in the fringe pattern are from ¼ to ½ of the amplitude of the longer wavelength fast mode, which would explain why the slow mode could not be measured earlier.

The fringe pattern that develops in Fig. 45 cannot result from the parametric sideband components observed in the last section. This is because the amplitude of the sidebands are less than one-eighth of the amplitude of the peaks in the fringe pattern. Therefore the fringe pattern must result from wave components at the frequency of

Figure 45. Voltage to probe tip 1, V_{p1}, probe tip 2, V_{p2}, and $V_{p1}-V_{p2}$ versus time. Wave power = 10kW and density at the beginning of the RF pulse is $n \simeq 4 \times 10^{11} cm^{-3}$. The double probe is placed on the separatrix near the upper inner hoop.

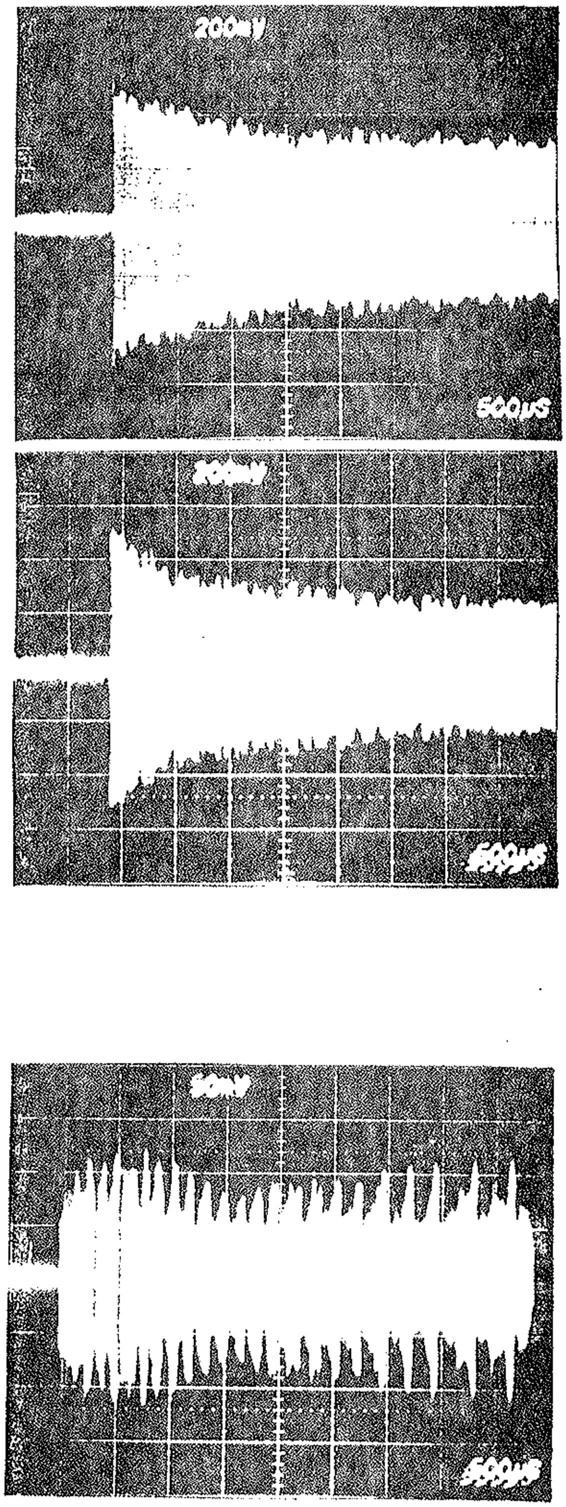
200mV
V_{p1} (200 $\frac{mV}{DIV}$)
500µS
200mV
V_{p2} (200 $\frac{mV}{DIV}$)
500µS
50mV
$V_{p1}-V_{p2}$ (50 $\frac{mV}{DIV}$)
500µS
TIME (0.5 $\frac{ms}{DIV}$)

the pump wave (140MHz).

It is very unlikely that the pattern is caused by two wave components of slightly different frequency beating together and forming a modulated envelope signal. From Fig. 45 the beat frequency would have to be close to about 6kHz. The pump wave, however, has a bandwidth of a few megahertz. It is difficult to imagine how two very distinct and closely spaced frequency components could be isolated from the myriad of possible frequencies within this band.

It is also unlikely that the fringe pattern is due to a plasma fluctuation. Because of the high pass filter, these fluctuations would have to modulate the wave fields. The lack of modulation in the unsubtracted signals in Fig. 45 is evidence that no such fluctuation is occurring. In addition, lower frequency plasma probes do not show any regular fluctuating signals resembling those in the photo.

We can obtain the wavelength of the wave from the fringe pattern in Fig. 45, having established some credence in the measurement from the above discussion. Combining the wavelength measurements with measurements of ion temperature and density, we obtain the dispersion relation shown in Fig. 46. The theoretical dispersion relation for $k_z v_e/\omega = 0.29$, 0.16, and 0.02 with B=2.2kG are included in the figure for comparison.

For densities below about $n = 2.75 \times 10^{11} cm^{-3}$, the wavelength is slightly less than values based upon the theoretical antenna n_z spectrum. Above this density the curve can be explained by invoking a monotonic increase in the edge values of n_z as the wave propagates

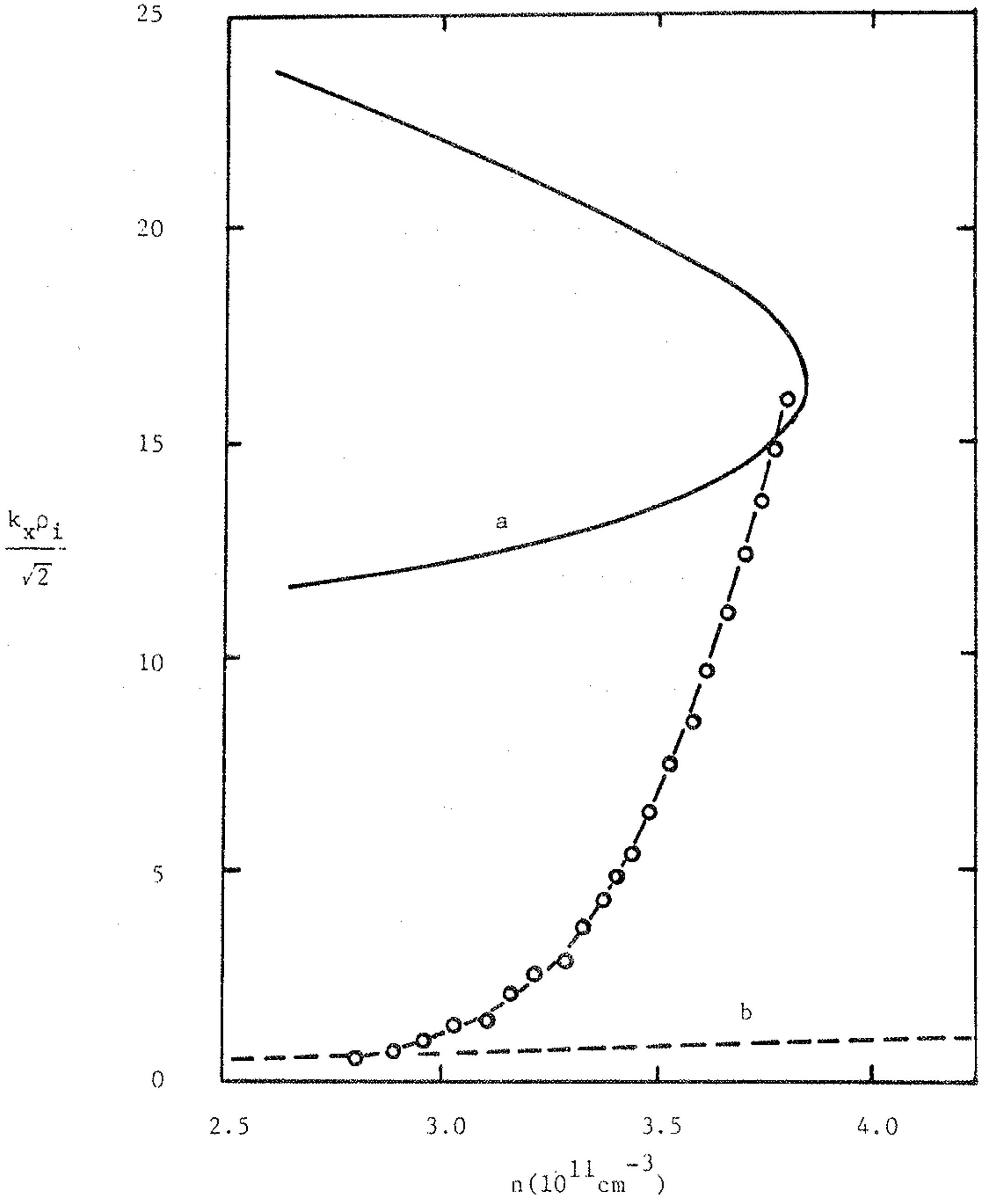

Figure 46. Measured values of $k_x \rho_i/\sqrt{2}$ versus plasma density. Theoretical curves are for (a) $k_z v_e/\omega = 0.3$ and (b) $k_z v_e/\omega = 0.02$.

toward the plasma interior, consistent with the heating results in earlier chapters.

The manner in which n_z must increase in order to explain Fig. 46 is shown in Fig. 47 which is derived from the dispersion relation, Eqn. (2.28). We see that values of $k_z v_e/\omega$ determined in this manner are in close agreement with heating results (see Figs. 30 and 32 for example).

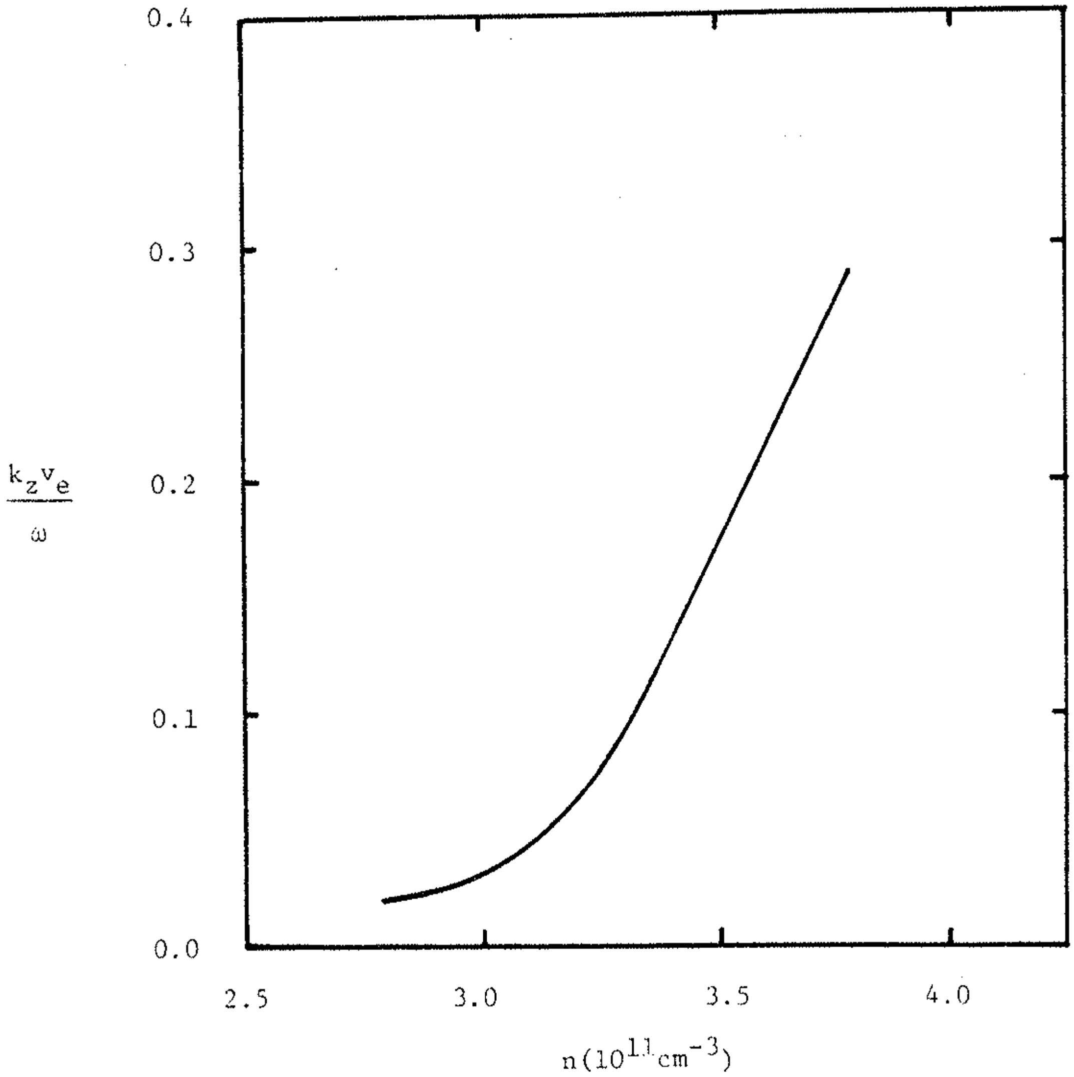

Figure 47. Enhancement of $k_z v_e/\omega$ versus density deduced from Fig. 46 and Eqn. (2.28).

CHAPTER 9

CONCLUSIONS

We have demonstrated that lower hybrid wave heating is an effective method of heating both ions and electrons in the complex geometry of a toroidal octupole. Heating efficiencies between 20-40% have been obtained with stable confinement when the wave turning point is coincident with the magnetic separatrix.

The heating zone follows the wave turning point if we assume that the k_z wave power spectrum is upshifted to a value defined by $k_x v_e/\omega = 0.3$. This represents a factor of between eight and fifteen increase in the value of k_z over its value at the antenna.

Assuming this same value for $k_z v_e/\omega$, ion heating is measured only when the theoretical lower hybrid wave turning point is present in the machine. This is perhaps the strongest evidence presented supporting the idea that the wave undergoes a mode conversion from a cold plasma backward wave into a warm plasma forward wave which is then absorbed near the conversion point.

Calculations in chapter two show that over 80% of the wave should be able to mode convert for typical experimental conditions. In addition, we have eliminated in chapter eight the possibility that ion heating is due to parametric instabilities. Both of these points back up the possibility that ion heating results after a mode conversion process.

Finally, we have verified that a short wavelength mode ($k_x \rho_i \simeq 10-20$)

exists near the lower hybrid wave turning point. Typical wavelengths for this mode are very close to those required for the slow lower hybrid wave with $k_z v_e/\omega = 0.3$. This is consistent with the ion heating results and backs up the idea that $k_z v_e/\omega$ is increasing from its value at the antenna. In addition, the wave measurements indicate that the increase in k_z must occur near the wave conversion point where k_x increases rapidly.

The exact mechanism by which this upshift in k_z occurs is not well understood. The Alcator group has suggested in their experiment that the upshift in k_z that they observe is due to a parametric downshift in frequency of the entire pump wave near the plasma edge which simultaneously undergoes an upshift in k_z. While this result may apply to the Alcator experiment, it is not consistent with our results, since we observe the upshift near the center of the plasma rather than the edge.

It can be shown that plasma inhomogeneities cause substantial increases in k_z near the plasma center.[6,11] This provides a more reasonable explanation of our results, especially considering the nature of the octupole geometry. This possibility can be demonstrated most simply by reconsidering the electostatic equation for wave potential (Eqn. (2.37)),

$$\frac{\partial}{\partial x}\left(K_{xx}\frac{\partial \phi}{\partial x}\right) \quad \frac{\partial}{\partial z}\left(K_{zz}\frac{\partial \phi}{\partial z}\right) = 0$$

In the analysis of chapter two, the plasma was assumed to be uniform in the $\hat{z}$ direction. This allowed us to Fourier analyze this equation in the $\hat{z}$ direction and hold k_z fixed as we moved in the $\hat{x}$ direction. The value of k_x increased considerably along x. Because of the symmetry of this equation in the derivatives with respect to x and z, we could also assume uniformity in the $\hat{x}$ direction and non-uniformity in the $\hat{z}$ direction. In this case k_x would be held fixed and k_z would vary with plasma parameters. For non-uniformity in both $\hat{x}$ and $\hat{z}$ directions, we would expect both k_x and k_z to vary with position, which is what the experiment implies.

The argument can be made a little more quantitative by considering, as an example, the results of Briggs and Parker.[11] They assume that a slight density gradient exists along a magnetic field line in addition to a large gradient across the magnetic field. The total gradient then makes a slight angle, α, with the normal to the magnetic field lines. The angle need only be on the order of $\alpha \approx (m_e/m_i)^{\frac{1}{2}}$ to have an enormous effect upon wave behavior.

They find that the wave number along the density gradient, k_ρ, now grows to large values for densities close to $n=n_H(1+m_i/m_e \sin^2\alpha)^{-1}$, where n_H is the resonant density for the usual case of $\alpha=0$.

But this large k_ρ will now have a projection along the magnetic field ($\hat{z}$ direction) that will enhance the value of k_z at the plasma edge, k_z^e, according to,

$$k_z = k_\rho \sin\alpha + k_z^e \; . \tag{9.1}$$

Since α is small, we can take $k_\rho \simeq k_x$ and $\sin\alpha \simeq \alpha \simeq \ell_x/\ell_z$, where ℓ_x and ℓ_z are the scale lengths for density variation across and along the magnetic field, respectively. The amount of k_z enhancement will then be given by,

$$\frac{k_z}{k_z^e} \simeq \left(1 + \frac{k_x}{k_z^e}\frac{\ell_x}{\ell_z}\right) \tag{9.2}$$

Taking values from the experiment, $k_z^e\, c/\omega \simeq 4$, $k_x v_i/\omega_{ci} \simeq 20$, and $k_z v_e/\omega \simeq 0.3$, we find that $\ell_x/\ell_z \lesssim .05$ is necessary to produce sufficient k_z enhancement to explain our experimental results.

This represents a rather small variation in density along a magnetic field line that would be difficult to measure in practice particularly in the presence of RF heating. In addition it is possible that such a gradient would occur locally near the lower hybrid resonance in the inner bridge region of the octupole. Probe access to this region is very restricted and measurements along a magnetic field line would be almost impossible.

It is not unreasonable to expect, however, that local density perturbations do exist in the presence of RF heating, considering the magnitude of the ion temperature perturbation ($\Delta T_i/T_{io} \gtrsim 3$) and the fact that lower hybrid wave power is deposited locally in space. The RF heating could, for example, set up electrostatic potential barriers along a field line to restrict the flow of plasma along the field. Study of this area should have an improtant place in future research.

The results from this experiment imply for future lower hybrid heating experiments that efficient ion heating can be obtained even though careful control of the k_z wave power spectrum may not be possible. Experiments designed to achieve ion heating should therefore be flexible enough to allow for possible variations in the lower hybrid resonant parameters caused by changes in k_z from its value at the launching structure.

Flexibility is in addition warranted by the observation in the octupole that lower hybrid ion heating results from efficient wave absorption without producing unstable plasmas over a rather narrow window of plasma parameters. Once attention has been given to the above intricacies, however, effective lower hybrid heating can be obtained.

APPENDIX A

PRINCIPLES OF FABRY-PEROT INTERFEROMETRY

A basic schematic of the Fabry -Perot instrument is shown in Fig. 13. The main part of the instrument consists of two parallel and partially transmitting mirrors followed by a focussing lens. Rays of parallel light at an angle θ to the mirror normal undergo multiple reflections between the etalon plates and are then focused by the lens. Each ray will have a different phase at the focal point of the lens, producing an interference effect.

For an extended source, rays of many angles will be incident on the instrument. If this source is also monochromatic , a bullseye pattern will result in the focal plane of the lens. The distribution of intensity along any line through the center of the pattern in the focal plane is given by Airy's equation ,

$$I = I_m \left(1 + \frac{4R \sin^2(\phi/2)}{(1-R)^2}\right)^{-1} \qquad (3.8)$$

where R is the reflectiviy of the mirror, ϕ is the phase difference between successive transmitted rays, and I_m is the peak value of intensity. The value of ϕ is given by,

$$\phi = 4\pi\mu\sigma\ell \cos \phi \qquad (3.9)$$

where μ is the index of refraction of the medium between the mirror plates, $\sigma = 1/\lambda$, and ℓ is the distance between the mirror plates. The value of I_m will depend upon mirror reflection and losses according to,

$$I_m = \left(\frac{T}{1-R}\right)^2 I_o \qquad (3.10)$$

where I_o is the intensity of the incident radiation, and T is the transmittivity of the mirrors after losses and reflection.

Note from Eqn. (3.80)that maxima in the fringe pattern occur whenever $\phi = 2\pi n$, where n is the order of the fringe. For fixed σ, μ, and ℓ, we see from Eqn. (3.9) that peaks occur periodically in ∂, producing the bullseye ring pattern mentioned earlier. Each ring corresponds to a different order, n.

Normally, a pinhole is placed on axis in the focal plane of the lens (Fig. 13). This restricts us to measuring at the pinhole only rays that are nearly parallel to the axis of the device. With $\phi \approx 0$ and μ and ℓ now held fixed the peak intensity will be periodic in σ occurring whenever,

$$\sigma = \frac{n}{2\ell} \qquad (3.11)$$

where the free space value for μ, $\mu=1$, has been used. The change in σ between peaks, $\Delta\lambda = 1/2\ell$, is called the free spectral range of the instrument. It determines the maximum breadth of the spectrum that can be measured without confusion with other orders.

The spectral width at which the maximum intensity decreases by one-half is obtained from Eqn. (3.8) as,

$$\delta\sigma = \frac{1-R}{2\pi\ell\sqrt{R}} \quad . \qquad (3.12)$$

The ratio between the free spectral range and the spectral width as determined from Eqn. (3.8) is called the Airy finesse or reflective finesse and is given explicitly as,

$$F_A = \frac{\Delta\gamma}{\delta\gamma} = \frac{\pi\sqrt{R}}{(1-R)} \quad . \tag{3.13}$$

Physically, the magnitude of the Airy finesse equals roughly the number of monochromatic light beams, equally spaced in frequency, that can be resolved by the instrument within a free spectral range. Eqn. (3.13) represents the maximum finesse possible in a given instrument. The overall instrumental finesse will be reduced by such things as defects in the mirror plates, or finite pinhole size. Each of these can be assigned an effective finesse. The overall instrumental finesse will then be given by[49],

$$\frac{1}{F_I^2} = \sum_i \frac{1}{F_i} \ , \tag{3.14}$$

where F_i is the overall instrumental finesse.

Understanding these limitations, we can define the maximum resolution of the Fabry-Perot as,

$$R_r = \frac{\sigma}{\delta\gamma} = 2\ell\sigma F_A \ . \tag{3.15}$$

From Eqn. (3.13), we see that the maximum resolution is limited by mirror reflectivity. Attempts to increase the reflectivity in order to increase the resolution result in loss of transmission, as will be shown later. In addition, as the reflective resolution R_r increases and F_A increases, eventually other broadening mechanisms will dominate, as is evident from Eqn. (3.14).

One other quantity that will be important is the contrast, c, of the Fabry-Perot. From Eqn. (3.8) a minimum in intensity occurs when $\phi = (2n+1)\pi$. Taking the ratio of maximum intensity, I_m, to minimum intensity yields,

$$c = \frac{(1+R)^2}{(1-R)^2} \ . \qquad (3.16)$$

This characteristic of the instrument is sometimes a problem, particularly if very bright spectral lines are present besides the spectral line of interest. If the minimum in the profile of spurious lines is brighter than the maximum intensity of the line under investigation, measurements are impossible even if the interfering orders of the lines are arranged so that the peak of one occurs at the minimum of the other.

The pre-disperser in front of the etalon must be carefully chosen to eliminate these interfering lines (Fig. 13). It is generally made up of a prism or grating monochromator, or an interference filter. The predisperser will reduce the overall throughput of the instrument and under some conditions may even dominate the throughput efficiency.

The pinhole on axis in the plane of the telescope lens (Fig.13) can also limit overall light gathering efficiency if it is smaller than necessary. If it is too large, on the other hand, it can destroy resolution. More light is gathered as the pinhole size increases the instrument width should be on the order of the actual line width to give maximum throughput while at the same time maintaining acceptable errors in the determination of actual line widths.[50] This requires, however, use of a flexible instrument and knowledge of the approximate line width of the incident radiation.

APPENDIX B

COMPARISON OF FABRY-PEROT THROUGHPUT WITH PRISM AND GRATING MONOCHROMATORS

We begin by designating for each monochromator the incident power per unit solid angle per unit area per unit wavelength as the quantity S. The throughput will be given by,

$$\Phi = \int_A \int_\Omega \int_0^\infty S\varepsilon dA d\Omega d\lambda \quad , \tag{3.20}$$

where ε is the transmittance of the system, Ω is the solid angle of light accepted by exit aperature, and A is the area of the light beam passed by the system stop.

For uniform illumination of the system stop, and for incident power per unit wavelength equal to one, the throughput becomes,

$$\Phi = A\Omega\varepsilon \quad . \tag{3.21}$$

For monochromators having stops of equal area, we see that the throughput is simply proportional to the product of transmittance and solid angle of light accepted by each system. This assumes that the resolving power allowed by the exit aperature, R_p, is less than or on the order of the maximu possible resolving power of the system, denoted by R_o. Finally, to obtain a fair comparison among the various monochromators, we must examine throughput for equal resolving powers, in addition to equal areas. This will be facilitated by obtaining Ω in terms of the resolution for each instrument as follows.

For the grating and the prism monochromators, which use slits, $\Omega = \beta d\alpha$, where β is the angular height of the exit slit and $d\alpha$ is the angular width. The angular width of a monochromatic extended source at the detector will be given by,

$$\delta\lambda = d\alpha\left(\frac{d\theta}{d\lambda}\right)^{-1} \tag{3.22}$$

where $d\theta/d\lambda$ is the angular dispersion of the dispersing element. The angular width of the slit is thus related to the overall resolution of the monochromator according to,

$$d\alpha = \frac{\lambda}{R_p}\,\frac{d\theta}{d\lambda}\ . \tag{3.23a}$$

The total throughput can then be expressed as,

$$\Phi = \frac{A\varepsilon\beta\lambda}{R_p}\,\frac{d\theta}{d\lambda} \tag{3.23b}$$

Specializing this equation to the case of a prism monochromator, we find,

$$\frac{d\theta}{d\lambda} = \frac{w}{b}\,\frac{dn}{d\lambda} \tag{3.24}$$

where w is the longest distance of the beam through the prism, b is the height of the beam of light exiting the prism, and n is the index of refraction of the prism material. For a prism of length h, the throughput is then given from Eqn. (3.23b) as,

$$\phi = (wh)\varepsilon \frac{\beta\lambda}{R_p} \frac{dn}{d\lambda} = B\varepsilon \frac{\beta\lambda}{R_p} \frac{dn}{d\lambda} \qquad (3.25)$$

where B is the area of the base of the prism.

For the grating monochromator[52],

$$\frac{d\theta}{d\lambda} = \frac{m\eta}{\ell \cos\beta} \qquad (3.26)$$

where m is the order of interference, ℓ is the grating length, η is the number of lines in the grating, and β is the angle of observation relative to the normal to the grating surface. The following equation applies to reflecting grating monochromators,

$$(\sin\alpha - \sin\beta) = (\frac{\eta}{\ell})m\lambda \qquad (3.27)$$

where α is the angle of incident radiation with respect to the normal. The order, m, can then be eliminated in Eqn. (3.26),

$$\frac{d\theta}{d\lambda} \quad \frac{(\sin\alpha - \sin\beta)}{\lambda \cos\beta} . \qquad (3.28)$$

Noting that the area of the aperature stop is given by $A=G \cos\beta$ where G is the area of the grating, we obtain the throughput from Eqn. (3.23b) as,

$$\Phi = G\beta\varepsilon \frac{\sin\alpha - \sin\beta}{R_p} \qquad (3.29)$$

Obtaining the maximum intensity from the grating requires operating in the center of the spectral range for which the blaze angle of the groves is cut. The maximum intensity within this spectral range, in turn, occurs when $\alpha = \beta = \phi$, where ϕ is the blaze angle. Assuming this optimum operating condition, the grating monochromator throughput becomes,

$$\Phi = G\beta\varepsilon \frac{2 \sin\phi}{R_p} \tag{3.30}$$

Now taking the ratio of Eqn. (3.30) with Eqn. (3.25) we find[53],

$$\frac{\Phi_{prism}}{\Phi_{grating}} = \frac{\lambda}{2 \sin\phi} \frac{dn}{d\lambda}\Bigg|_{prism} \tag{3.31}$$

where we have assumed the area of the base of the prism equals the area of the grating, and the slit angular heights β, the transmittances, and the resolving power are all equal.

Now the blaze angle ϕ can be related in the following way to the blaze wavelength, λ_b, which is the wavelength of maximum intensity in the center of the spectral range for the grating,

$$2 \sin\phi = \left(\frac{n}{\ell}\right) \lambda_b \; . \tag{3.32}$$

If we assume, finally, that $\lambda = \lambda_b$ then Eqn. (3.31) becomes,

$$\frac{\Phi_{prism}}{\Phi_{grating}} = \frac{\ell}{\eta} \frac{dn}{d\lambda} \tag{3.33}$$

As an example, for a prism made of crown glass, $dn/d\lambda = 7.5 \times 10^{-6} \text{Å}^{-1}$ at $\lambda = 4861$ Å. A high quality grating could have 1200 lines per millimeter. Adjusting the blaze angle so that $\lambda_b = 4861$ A, Eqn. (3.33) yields,

$$\frac{\Phi_{\text{prism}}}{\Phi_{\text{grating}}} = 0.065 \quad .$$

There is thus a significant advantage of the grating over the prism monochromator.

We turn, finally, to the Fabry-Perot interferometer. In this case the solid angle accepted by the detector is given by, $\Omega \simeq \pi\theta^2$ where θ is the maximum angle of the incident rays with respect to the normal to the etalon plates. Now from Eqn. (3.17) and noting that $\psi=2\theta$, we can write,

$$\Omega = \frac{2\pi}{R_p} \quad . \tag{3.34}$$

But if we assume that the reflective finesse is equal to the pinhole finesse then from Eqn. (3.14) the overall resolution of the instrument is given by,

$$\frac{1}{R_I^2} = \frac{1}{R_p^2} + \frac{1}{R_A^2} = \frac{2}{R_p^2} \tag{3.35}$$

In terms of the overall resolution, then, the solid angle becomes,

$$\Omega = \frac{\sqrt{2}\,\pi}{R_I} \quad . \tag{3.36}$$

Notice that, as with the other monochromators, the resolution-intensity product is a constant, which was alluded to earlier and now is made explicit .

For a given monochromatic beam some of the line profile produced by the etalon at the focal plane will be blocked by the pinhole. This, in effect reduces the transmittance by a factor of $\pi/4$. The final expression for the throughput of the Fabry-Perot interferometer is then given by,

$$\Phi = \frac{\pi^2}{2\sqrt{2}} \frac{\varepsilon F}{R_I} \tag{3.36}$$

taking the ratio of Eqn. (3.36) with Eqn. (3.30) and using Eqn. (3.32) we find[53],

$$\frac{\Phi_{FP}}{\Phi_{grating}} = \frac{\pi^2}{2\sqrt{2}} \frac{\ell}{n} \frac{1}{\lambda_b \beta} \quad ; \tag{3.37}$$

where the peak transmittances and resolutions are taken to be equal for the two instruments, and the area of the grating equals the area of the etalon plates.

As a typical example, for a 1 meter grating monochrometer with 2cm slit height, $\beta = 1/50$. Assume, once again 1200 lines per millimeter, and take $\lambda_b = 4686$ Å. Eqn. (3.37) then becomes,

$$\frac{\Phi_{FP}}{\Phi_{grating}} \simeq 300 \ . \tag{3.38}$$

The superiority of the Fabry-Perot is clearly demonstrated.

REFERENCES

1. T.H. Stix, Phys. Rev. Lett. 15, 878 (1965).
2. G.J. Morales and Y.C. Lee, Phys. Rev. Lett., 35, 930 (1975).
3. A. Sen, C.F.F. Karney, G.L. Johnston, A. Bers, Nuclear Fusion, 18, 171 (1978).
4. M. Porkolab, Phys. Fluids, 17, 1432 (1974).
5. C.F.F. Karney and A. Bers, Phys. Rev. Lett., 39, 550 (1977).
6. P.L. Colestock, Nuclear Fusion, 18, 740 (1978).
7. E. Ott and R.V. Lovelace, Bulletin of the American Physical Society, 2, 765 (1978).
8. A. Sen and N.J. Fisch, Massachusetts Institute of Technology report PRR 78/16, 1978.
9. R.P.H. Chang and M. Porkolab, Phys. Rev. Lett., 32, 1227 (1974).
10. P.M. Bellan and M. Porkolab, Phys. Fluids, 19, 995 (1976).
11. R.J. Briggs and R.R. Parker, Phys. Rev. Lett., 29, 852 (1972).
12. P. Lallia in Symposium on Plasma Heating in Toroidal Devices, Varenna, Italy (1974).
13. J.E Scharer, et. al.,"Fast Magnetosonic Wave Heating of the Conceptual NUWMAK Tokamak Reactor" (To be published in Nuclear Fusion).
14. P. Lallia and Vega Group, in Proceedings of the Fourth International Conference on Theoretical and Experimental Aspects of Heating Toroidal Plasmas, Grenoble, France, 1978.

PLP REPORTS

In this thesis, several references are made to the internal reports of the University of Wisconsin plasma physics group. These reports, which are identified by PLP numbers, are available upon request from:

Plasma Physics Office
University of Wisconsin
1150 University Avenue
Madison, WI 53706